Enzo+Moray: Radiation Hydrodynamics Adaptive Mesh Refinement Simulations with Adaptive Ray Tracing

John H. Wise[1,2], Tom Abel[3], Ji-hoon Kim[3], Peng Wang[3,4], Peter Iannucci[5]

jwise@astro.princeton.edu

ABSTRACT

We describe a photon-conserving numerical method that solves the radiative transfer equation, using a spatially-adaptive ray tracing scheme, and its parallel implementation into the adaptive mesh refinement (AMR) code, Enzo. Coupling the solver with the energy equation and non-equilibrium chemistry network, our radiation hydrodynamics framework can be utilized to study a broad range of astrophysical problems, such as stellar and black hole (BH) feedback. Inaccuracies can arise from large timesteps and poor sampling, therefore we devised an adaptive time-stepping scheme and a fast approximation of the optically-thin radiation field with multiple sources. We test the method with several radiative transfer and radiation hydrodynamics tests that are given in Iliev et al. (2006a, 2009). We further test our method with more dynamical situations, for example, the propagation of an ionization front through a Rayleigh-Taylor instability, time-varying luminosities, and collimated radiation. This method linearly scales with the number of point sources and number of grid cells. To combat this, we use a novel method of merging rays at large radius, using a tree method, which we briefly describe. Our implementation is scalable to $O(10^3)$ processors on distributed and shared memory machines and can include radiation pressure and secondary ionizations from X-ray radiation. It is included in the newest public release of Enzo.

Subject headings: cosmology — methods: numerical — hydrodynamics — radiative transfer

[1]Department of Astrophysical Sciences, Princeton University, Peyton Hall, Ivy Lane, Princeton, NJ 08544

[2]Hubble Fellow

[3]Kavli Institute for Particle Astrophysics and Cosmology, Stanford University, Menlo Park, CA 94025

[4]NVIDIA

[5]Massachusetts Institute of Technology

1. Introduction

Radiative transfer is ubiquitous in many astrophysical problems, encompassing topics such as stellar atmospheres, the interstellar medium (ISM), star formation, galaxy formation, supernovae (SNe) and cosmology. Thus it is a well-studied problem (e.g. Mathews 1965; Rybicki & Lightman 1979; Mihalas & Mihalas 1984; Yorke 1986); however, its treatment in multi-dimensional calculations is difficult because of the dependence on seven variables — three spatial, two angular, frequency, and time. The non-local nature of the thermal and hydrodynamical response to radiation sources further adds to the difficulty. In the general case, one must consider all radiation sources at every point in calculation.

Fortunately problems can be simplified by exploiting symmetries and special cases. The first case was considered by Strömgren (1939) for a radiation source ionizing a static uniform neutral medium, where recombinations balance photo-ionizations. He derived a radius of an H II region,

$$R_s = \left(\frac{3\dot{N}_\gamma}{4\pi \alpha_{\rm B} n_H^2} \right)^{1/3} , \tag{1}$$

where $\dot{N}_\gamma$ is the ionizing photon luminosity, $\alpha_{\rm B}$ is the recombination rate, and n_H is the ambient hydrogen number density. Furthermore he found that the delineation between the neutral and ionized medium to be approximately the mean free path of the ionizing radiation. His seminal work was expanded upon by Spitzer (1948, 1949, 1954) and Spitzer & Savedoff (1950), who showed that the ionizing radiation heated the medium to $T \sim 10^4$ K. If the density is equal on both sides of the ionization front, then this over-pressurized region would expand and drive a shock outwards (e.g. Oort 1954; Schatzman & Kahn 1955). These early works provided the basis for the modern topic of radiation hydrodynamics. A decade later, the first radiation hydrodynamical numerical models of H II regions in spherical symmetry and plane-parallel ionization fronts were developed (e.g. Mathews 1965; Lasker 1966; Hjellming 1966). They described the expansion of the ionization front and the evolution of its associated shock wave that carries most of the gas away from the source. At the same time, theoretical models of ionization fronts matured and were classified by Kahn (1954) and Axford (1961) as either R-type (rare) or D-type (dense). In R-type fronts, the ionized gas density is higher than the neutral gas density, and in D-type fronts, the opposite is true. R-type fronts travel supersonically with respect to the neutral gas, whereas D-type front are subsonic. Furthermore "weak" and "strong" R-type fronts move supersonically and subsonically with respect to the ionized gas, respectively. The same terminology conversely applies to D-type fronts. "Critical" fronts are defined as moving exactly at the sound speed. These works established the evolutionary track of an expanding H II illuminated by a massive star in a uniform medium:

1. Weak R-type—When the star (gradually) starts to shine, the ionization front will move supersonically through the ambient medium. The gas is heated and ionized, but otherwise left undisturbed. This stage continues until $r \sim 0.02 R_s$.

2. Critical R-type—As the ionization front moves outwards, it begins to slow because of the geometric dilution of the radiation. It becomes a critical R-type front, which is equivalent to an isothermal shock in the neutral gas.

3. Strong and weak D-type—The front continues to slow, becoming a strong D-type front, and then a critical D-type front. From this point forward, it is moving subsonically with respect to the ionized gas, i.e. a weak D-type front. Thus sound waves can travel across the ionization front and form a shock. The ionization front detaches from the shock, putting the shock ahead of the ionization front.

4. Expansion phase—After the shock forms, the H II region starts to expand, lowering the interior density and thus the recombination rates. This increases the number of photons available for ionizing the gas. The sphere expands until it reaches pressure equilibrium with the ambient medium at $r \sim 5 R_s$.

In the 1970's and 1980's, algorithmic and computational advances allowed numerical models to be expanded to two dimensions, mainly using axi-symmetric to simplify the problem (e.g. Bodenheimer et al. 1979; Sandford et al. 1982; Yorke et al. 1983). One topic that was studied extensively were champagne flows. Here the source is embedded in an overdense region, and the H II region escapes from this region in one direction. The interface between the ambient and dense medium was usually set up to be a constant pressure boundary. When the ionization front passes this boundary, the dense, ionized gas is orders of magnitude out of pressure equilibrium as the temperatures on both sides of initial boundary are within a factor of a few. In response, the gas is accelerated outwards in this direction, creating a fan-shaped outflow.

Only in the past 15 years, computational resources have become large enough, along with further algorithmic advances, to cope with the requirements of three-dimensional calculations. There are two popular methods to solve the radiative transfer equation in three-dimensions:

- Moment methods—The angular moments of the radiation field can describe its angular structure, which are related to the energy energy, flux, and radiation pressure (Auer & Mihalas 1970; Norman et al. 1998). These have been implemented in conjunction with short characteristics (Stone et al. 1992, 2D), with long characteristics (Finlator et al. 2009), with a variable Eddington tensor in the optically thin limit (OTVET; Gnedin

& Abel 2001; Petkova & Springel 2009), and with an M1 closer relation (González et al. 2007; Aubert & Teyssier 2008). Moment methods have the advantage of being fast, being independent of the number of radiation point sources. However, they are diffusive and result in incorrect shadows in some situations.

- Ray tracing—Radiation can be propagated along rays that extend through the computational grid (e.g. Razoumov & Scott 1999; Abel et al. 1999; Ciardi et al. 2001; Sokasian et al. 2001; Whalen & Norman 2006; Rijkhorst et al. 2006; Mellema et al. 2006; Alvarez et al. 2006a; Trac & Cen 2007; Krumholz et al. 2007; Paardekooper et al. 2010) or particle set (e.g. Susa 2006; Johnson et al. 2007; Pawlik & Schaye 2008, 2010; Altay et al. 2008; Hasegawa et al. 2009). In general, these methods are very accurate but computationally expensive because the radiation field must be well sampled by the rays with respect to the spatial resolution of the grid or particles.

Until the mid-2000's the vast majority of the three-dimensional calculations were performed with static density distributions. One example is calculating cosmological reionization by post-processing of density fields from N-body simulations (Ciardi et al. 2001; Sokasian et al. 2001; McQuinn et al. 2007; Iliev et al. 2006b, 2007). Any hydrodynamical response to the radiation field was thus ignored. Several radiative transfer codes were compared in four purely radiative transfer tests in Iliev et al. (2006a, hereafter RT06). Only recently has the radiative transfer equation been coupled to the hydrodynamics in three-dimensions. In the second comparison paper (Iliev et al. 2009, hereafter RT09), results from these radiation hydrodynamics codes were compared. Even more rare are ones that couple it with magneto-hydrodynamics (e.g. Krumholz et al. 2007). The tests in RT06 and RT09 were kept relatively simple to ease the comparison.

In this paper, we present our implementation, Enzo+Moray, of adaptive ray tracing (Abel & Wandelt 2002) in the cosmological hydrodynamics adaptive mesh refinement (AMR) code, *Enzo* (Bryan & Norman 1997; O'Shea et al. 2004). The radiation field is coupled to the hydrodynamics solver at small timescales, enabling it to study radiation hydrodynamical problems. We have used this code to investigate the growth of an H II region from a $100 M_\odot$ Population III (Pop III) star (Abel et al. 2007), radiative feedback on the formation of high redshift dwarf galaxies (Wise & Abel 2008b), the early stages of reionization from Pop III stars (Wise & Abel 2008a), ultraviolet radiation escape fractions from dwarf galaxies before reionization (Wise & Cen 2009), radiative negative feedback from accreting Pop III seed black holes (Alvarez et al. 2009), and radiative feedback in accreting supermassive black holes (Kim et al. 2011, in prep.). We have included Enzo+Moray in the latest public release

of *Enzo*[1], and it is also coupled with the newly added MHD solver in *Enzo* (Wang & Abel 2009).

We have structured this paper as follows. In Section 2, we describe the connections between adaptive ray tracing and the radiative transfer equation. Furthermore, we detail how physics other than photo-ionization and photo-heated are included. We then derive a geometric correction factor to any ray tracing method to improve accuracy. We end the section by describing a new computational technique to approximate an optically-thin radiation field with ray tracing and multiple sources. In Section 3, we cover the details of our radiation hydrodynamics implementation in *Enzo*, specifically (1) the ray tracing algorithms, (2) coupling with the hydrodynamics solver, (3) several methods to calculate the radiative transfer timestep, and (4) our parallelization strategy. We present our results from the RT06 radiative transfer tests in Section 4. Afterwards in Section 5, we show the results from the RT09 radiation hydrodynamics tests. We expand on these tests to include more dynamical and complex setups to demonstrate the flexibility and high fidelity of Enzo+Moray. Section 6 reports the results from spatial, angular, frequency, and temporal resolution tests. In Section 7, we illustrate the improvements from the geometric correction factor and our optically-thin approximation. We also show the effects of X-ray radiation and radiation pressure in this section. Finally in Section 8, we demonstrate the parallel scalability of Enzo+Moray. Last Section 9 summarizes our method and results.

2. Treatment of Radiative Transfer

Radiation transport is a well-studied topic, and we begin by describing our approach in solving the radiative transfer equation, which in comoving coordinates (Gnedin & Ostriker 1997) is

$$\frac{1}{c}\frac{\partial I_\nu}{\partial t} + \frac{\hat{n}\cdot\nabla I_\nu}{\bar{a}} - \frac{H}{c}\left(\nu\frac{\partial I_\nu}{\partial \nu} - 3I_\nu\right) = -\kappa_\nu I_\nu + j_\nu. \tag{2}$$

Here $I_\nu \equiv I(\nu, \mathbf{x}, \Omega, t)$ is the radiation specific intensity in units of energy per time t per solid angle per unit area per frequency ν. $H = \dot{a}/a$ is the Hubble constant, where a is the scale factor. $\bar{a} = a/a_{em}$ is the ratio of scale factors at the current time and time of emission. The second term represents the propagation of radiation, where the factor $1/a$ accounts for cosmic expansion. The third term describes both the cosmological redshift and dilution of radiation. On the right hand side, the first term considers the absorption coefficient $\kappa_\nu \equiv \kappa_\nu(\mathbf{x}, \nu, t)$, and the second term $j_\nu \equiv j_\nu(\mathbf{x}, \nu, t)$ is the emission coefficient that includes any point sources

---

[1]http://lca.ucsd.edu/enzo

of radiation or diffuse radiation.

Solving this equation is difficult because of its high dimensionality; however, we can make some appropriate approximations to reduce its complexity in order to include radiation transport in numerical calculations. Typically timesteps in dynamic calculations are small enough so that $\Delta a/a \ll 1$, therefore $\bar{a} = 1$ in any given timestep, reducing the second term to $\hat{n}\partial I_\nu/\partial\mathbf{x}$. To determine the importance of the third term, we evaluate the ratio of the third term to the second term. This is HL/c, where L is the simulation box length. If this ratio is $\ll 1$, we can ignore the third term. For example at $z = 5$, this ratio is 0.1 when $L = c/H(z = 5) = 53$ proper Mpc. In large boxes where the light crossing time is comparable to the Hubble time, then it could be important to consider cosmological redshifting and dilution of the radiation, which we will describe later in §2.1. Thus equation (2) reduces to the non-cosmological form in this local approximation,

$$\frac{1}{c}\frac{\partial I_\nu}{\partial t} + \hat{n}\frac{\partial I_\nu}{\partial\mathbf{x}} = -\kappa_\nu I_\nu + j_\nu. \tag{3}$$

We choose to represent the source term j_ν as point sources of radiation (e.g. stars, quasars) that emit radial rays that are propagated along the direction $\hat{n}$. Next we describe this discretization and its contribution to the radiation field.

2.1. Adaptive Ray Tracing

Ray tracing is an accurate method to propagate radiation from point sources on a computational grid, given that there are rays passing through each cell. Along a ray, the radiative transfer equation reads

$$\frac{1}{c}\frac{\partial P}{\partial t} + \frac{\partial P}{\partial r} = -\kappa P, \tag{4}$$

where P is the photon number flux along the ray. To sample the radiation field at large radii, ray tracing requires at least $N_{ray} = 4\pi R^2/(\Delta x)^2$ rays to sample each cell with one ray, where R is the radius from the source to the cell and Δx is the cell width. If one were to trace N_{ray} rays out to R, the cells at a smaller radius r would be sampled by, on average, $(r/R)^2$ rays, which is computationally wasteful because only a few rays per cell, as we will show later, provides an accurate calculation of the radiation field.

We avoid this inefficiency by utilizing adaptive ray tracing (Abel & Wandelt 2002), which progressively splits rays when the sampling becomes too coarse and is based on Hierarchical Equal Area isoLatitude Pixelation (HEALPix; Górski et al. 2005). In this scheme, the rays are traced along normal directions of the centers of HEALPix pixels, which evenly divides

Table 1.   Variable definitions

Variable	Description
I_ν	Specific intensity
$\hat{n}$	Normal direction of radiation
H	Hubble constant
a	Scale factor
κ_ν	Absorption coefficient
j_ν	Emission coefficient
r	Radius
l	HEALPix level
N_{ray}	Rays per cell
$N_{\mathrm{pix}}(l)$	HEALPix pixels on level l
Φ_c	Minimum rays per cell
Δx	Cell width
A_{cell}	Cell face area
V_{cell}	Cell volume
θ_{ray}	Angle associated with a ray
Ω_{ray}	Solid angle associated with a ray
dt_P	Photon timestep
τ	Optical depth
σ_{abs}	Cross-section of absorber
n_{abs}	Number density of absorber
k_{ph}	Photo-ionization rate
k_{diss}	Photo-dissociation rate of H_2
Γ_{ph}	Photo-heating rate
Y_{x}	Secondary ionization factors
E_{ph}	Photon energy
E_i	Ionization energy of absorber
$f_{\mathrm{shield}}(N_{\mathrm{H2}})$	Shielding function for H_2
N_{H2}	Column density of H_2
P	Photon flux
dP	Photon loss from absorption
dP_C	Photon loss from Compton Scattering
σ_{abs}	Absorber cross-section
$d\mathbf{p}_\gamma$	Momentum change from radiation pressure
$x_{0,\mathrm{i}}$	Cell center coordinates
$D_{\mathrm{ci,i}}$	Distance from ray segment center to cell center
D_{edge}	Distance from ray segment center to cell edge
L_{pix}	Linear width of a HEALPix pixel
f_c	Geometric correction factor

a sphere into equal areas. The rays are initialized at each point source with the photon luminosity (ph s^{-1}) equally spread across $N_{\rm pix} = 12 \times 4^l$ rays, where l is the initial HEALPix level. We usually find $l = 0$ or 1 is sufficient because these coarse rays will be usually be split before traversing the first cell.

The rays are traced through the grid in a typical fashion (e.g. Abel et al. 1999), in which we calculate the next cell boundary crossing. The ray segment length crossing the cell is

$$dr = R_0 - \min_{i=1\to3}\left[(x_{\rm cell,i} - x_{\rm src,i})/\hat{n}_{\rm ray,i}\right], \tag{5}$$

where R_0, $\hat{n}_{\rm ray}$, $x_{\rm cell,i}$, and $x_{\rm src,i}$ are the initial distance travelled by the ray, normal direction of the ray, the next cell boundary crossing on the i-th dimension, and the position of the point source that emitted the ray, respectively. However before the ray travels across the cell, we evaluate the ratio of the face area $A_{\rm cell}$ of the current cell and the solid angle $\Omega_{\rm ray}$ of the ray,

$$\Phi_c = \frac{A_{\rm cell}}{\Omega_{\rm ray}} = \frac{N_{\rm pix}(\Delta x)^2}{4\pi R_0^2}. \tag{6}$$

If Φ_c is less than a pre-determined value (usually > 2), the ray is split into 4 child rays. We investigate the variations in solutions with Φ_c in §6.2. The pixel numbers of the child rays p' are given by the "nested" scheme of HEALPix at the next level, i.e. $p' = 4 \times p + [0, 1, 2, 3]$, where p is the original pixel number. The child rays (1) acquire the new normal vectors of the pixels, (2) retain the same radius of the parent ray, and (3) gets a quarter of the photon flux of the parent ray. Afterwards the parent ray is discontinued.

A ray propagates and splits until

1. the photon has travelled $c \times dt_P$, where dt_P is the radiative transfer timestep,

2. its photon flux is almost fully absorbed ($> 99.9\%$) in a single cell, which significantly reduces the computational time if the radiation volume filling fraction is small,

3. the photon leaves the computational domain with isolated boundary conditions, or

4. the photon travels $\sqrt{3}$ of the simulation box length with periodic boundary conditions.

In the second case, the photon is halted at that position and saved, where it will be considered in the solution of I_ν at the next timestep. In the next timestep, the photon will encounter a different hydrodynamical and ionization state, hence κ, in its path. Furthermore any time variations of the luminosities will be retained in the radiation field. In this sense, our method retains the time derivative of the radiative transfer equation.

2.2.   Ray Merging

Unfortunately the computational work of ray tracing scales with the number of sources. To resolve this barrier, rays can be merged in cases with either nearly parallel rays from clustered sources of radiation, whether it be diffuse radiation or point sources, or where rays exit a region with high resolution into a coarsely resolved region. In each case, the factor Φ_c can be much higher than the desired value, and it would be efficient to merge these rays. We have devised a new scheme that merges rays from clustered sources based on a hierarchical binary tree, which is analogous to the gravity tree solvers. We show the performance improvements in the strong scaling tests (§8.2). However we leave its full details for a later paper.

2.3.   Radiation Field

The radiation field is calculated by integrating equation 4 along each ray, which is done by considering the discretization of the ray into segments. In the following section, we assume the rays are monochromatic. For convenience, we express the integration in terms of optical depth $\tau = \int \kappa(r,t)\, dr$, and for a ray segment,

$$d\tau = \sigma_{\mathrm{abs}}(\nu) n_{\mathrm{abs}} dr. \tag{7}$$

Here σ_{abs} and n_{abs} are the cross section and number density of the absorbing medium, respectively. We use the cell-centered density in our calculations but have experimented with trilinearly interpolated densities (see Mellema et al. 2006) without producing considerable artifacts. Equation (4) has a simple exponential analytic solution, and the photon flux of a ray is reduced by

$$dP = P \times (1 - e^{-\tau}) \tag{8}$$

as it crosses a cell. We equate the photo-ionization rate to the absorption rate, resulting in photon conservation (Abel et al. 1999; Mellema et al. 2006). Thus the photo-ionization k_{ph} and photo-heating Γ_{ph} rates associated with a single ray are

$$k_{\mathrm{ph}} = \frac{P(1 - e^{-\tau})}{n_{\mathrm{abs}}\, V_{\mathrm{cell}}\, dt_P}, \tag{9}$$

$$\Gamma_{\mathrm{ph}} = k_{\mathrm{ph}}\, (E_{\mathrm{ph}} - E_i), \tag{10}$$

where V_{cell} is the cell volume, E_{ph} is the photon energy, and E_i is the ionization energy of the absorbing material. In each cell, the photo-ionization and photo-heating rates from each ray in the calculation are summed, and after the ray tracing is complete, these rates

can be used to update the ionization state and energy of the cells. Considering a system with only hydrogen photo-ionizations and radiative recombinations, these changes are very straightforward and is useful for illustrative purposes. The change in neutral hydrogen is

$$\frac{dn_H}{dt} = \alpha_B n_e n_p - C_H n_e n_H - k_{ph}, \tag{11}$$

where $\alpha_B = 2.59 \times 10^{-13} \text{cm}^3 \text{s}^{-1}$ is the recombination coefficient at 10^4 K in the Case B on-the-spot approximation, in which all recombinations are locally reabsorbed, (Spitzer 1978), and C_H is the collisional ionization rate. However for more accurate solutions in calculations that consider several chemical species, the photo-ionization rates are better utilized in solvers that consider chemical networks (e.g. Abel et al. 1997).

2.4. Additional Physics

Other radiative processes can also be important in some situations, such as attenuation of radiation in the Lyman-Werner bands, secondary ionizations from X-ray radiation, Compton heating of from scattered photons, and radiation pressure.

2.4.1. Absorption of Lyman-Werner Radiation

Molecular hydrogen can absorb photons in the Lyman-Werner bands that are composed of 76 absorption lines ranging from 10.2 to 13.6 eV. Each of these spectral lines can be modelled with a typical exponential attenuation equation (Ricotti et al. 2001), but Draine & Bertoldi (1996) showed that this self-shielding is well modeled with the following relation to total H_2 column density

$$f_{shield}(N_{H2}) = \begin{cases} 1 & (N_{H2} \leq 10^{14} \text{ cm}^{-2}) \\ (N_{H2}/10^{14} \text{ cm}^{-2})^{-0.75} & (N_{H2} > 10^{14} \text{ cm}^{-2}) \end{cases}. \tag{12}$$

To incorporate this shielding function into the ray tracer, we store the total H_2 column density and calculate the H_2 dissociation rate by summing the contribution of all rays,

$$k_{diss} = \sum_{rays} \frac{P \; \sigma_{LW} \; \Omega_{ray} \; r^2 \; dr}{A_{cell} \; dV \; dt_P}, \tag{13}$$

where $\sigma_{LW} = 3.71 \times 10^{18} \text{cm}^2$ is the effective cross-section of H_2 (Abel et al. 1997). To account for any absorption in each photon package, we attenuate the photon number flux by

$$dP = P[f_{shield}(N_{H2} + dN_{H2}) - f_{shield}(N_{H2})], \tag{14}$$

where dN_{H2} is the H_2 column density in the current cell.

2.4.2. Secondary Ionizations from X-rays

A high-energy $(E_{\mathrm{ph}} \gtrsim 100$ eV$)$ photon can ionize multiple neutral hydrogen and helium atoms, and this should be considered in such radiation fields. Shull & van Steenberg (1985) studied this effect with Monte Carlo calculations over varying electron fractions and photon energies up to 3 keV. They find that the excitation of hydrogen and helium and the ionization of He II is negligible. The number of secondary ionizations of H and He is reduced from the ratio of the photon and ionization energies (E_{ph}/E_i) by a factor of

$$Y_{\mathrm{k,H}} = 0.3908(1 - x^{0.4092})^{1.7592}, \tag{15}$$

$$Y_{\mathrm{k,He}} = 0.0554(1 - x^{0.4614})^{1.6660}, \tag{16}$$

where x is the electron fraction. The remainder of the photon energy is deposited into thermal energy that is approximated by

$$Y_{\Gamma} = 0.9971[1 - (1 - x^{0.2663})^{1.3163}] \tag{17}$$

and approaches one as $x \to 1$. Thus in gas with low electron fractions, most of the energy results in ionizations of hydrogen and helium, and in nearly ionized gas, the energy goes into photo-heating.

2.4.3. Compton Heating from Photon Scattering

High energy photons can also cause Compton heating by scattering off free electrons. During a scattering, a photon loses $\Delta E(T_e) = 4kT_e \times (E_{ph}/m_e c^2)$ of energy, where T_e is the electron temperature. For the case of monochromatic energy groups, we model this process by considering that the photons are absorbed by a factor of

$$\frac{dP_C}{P} = (1 - e^{-\tau_e})\frac{\Delta(T_e)}{E_{ph}}, \tag{18}$$

which is the equivalent of the photon energy decreasing. Here $\tau_e = n_e \sigma_{KN} dl$ is the optical depth to Compton scattering, and σ_{KN} is the non-relativistic Klein-Nishina cross section (Rybicki & Lightman 1979). The Compton heating rate is thus

$$\Gamma_{\mathrm{ph,C}} = \frac{dP_C}{n_e \, V_{\mathrm{cell}} \, dt}. \tag{19}$$

2.4.4. Radiation Pressure

The absorption of radiation transfers momentum from photons to the absorbing medium, i.e. radiation pressure. This is easily computed by considering the momentum

$$d\mathbf{p}_\gamma = \frac{dP\, E_{\mathrm{ph}}}{c}\, \hat{r} \tag{20}$$

of the absorbed radiation from the incoming ray, where $\hat{r}$ is the normal direction of the ray. We do not include radiation pressure on dust, and thus our treatment underestimates its effects in applicable environments. The resulting acceleration of the gas due to radiation pressure is

$$d\mathbf{a} = \frac{d\mathbf{p}_\gamma}{dt\, \rho\, V_{\mathrm{cell}}}, \tag{21}$$

where ρ is the gas density inside the cell and dt is the radiative transfer timestep. This acceleration is then added to the other forces, e.g. gravity and gas pressure, in the calculation.

2.5. Geometric Corrections

Consider the solid angle Ω_{ray} and photon flux P associated with a single ray, and assume the flux is constant across Ω_{ray}. There exists a discrepancy between the geometry cell face and HEALPix pixel when the pixel does not cover the entire cell face, which is illustrated in Figure 1. This mismatch causes non-spherical artifacts and is most apparent in the optically thin case, where the area of the pixel is dominant over $(1 - e^\tau)$ when calculating k_{ph}. One can avoid these artifacts by increasing the sampling Φ_c to high values, e.g. > 10, but we have formulated a simple geometric correction to the calculation of the radiation field. This correction is not unique to the HEALPix formalism but can be applied to any type of pixelization.

The contribution to k_{ph} and Γ_{ph} must be corrected by a covering factor f_c. When the pixel is fully contained within the cell face, $f_c \equiv 1$. Because the geometry of the pixel can be complex, i.e. curved edges, we approximate f_c by assuming the pixel is square. The covering factor is thus related to the width of a pixel, $L_{\mathrm{pix}} = R_0\, \theta_{\mathrm{pix}}$, and the distance from the ray segment midpoint to the closest cell boundary, which is depicted in Figure 1. To estimate f_c, we first find the distance $d_{\mathrm{center,i}}$ from the midpoint of the ray segment to the cell center $x_{0,\mathrm{i}}$ in orthogonal directions,

$$D_{\mathrm{c,i}} = \left| R_{0,\mathrm{i}} + \hat{n}_i \frac{dr}{2} - x_{0,\mathrm{i}} \right|. \tag{22}$$
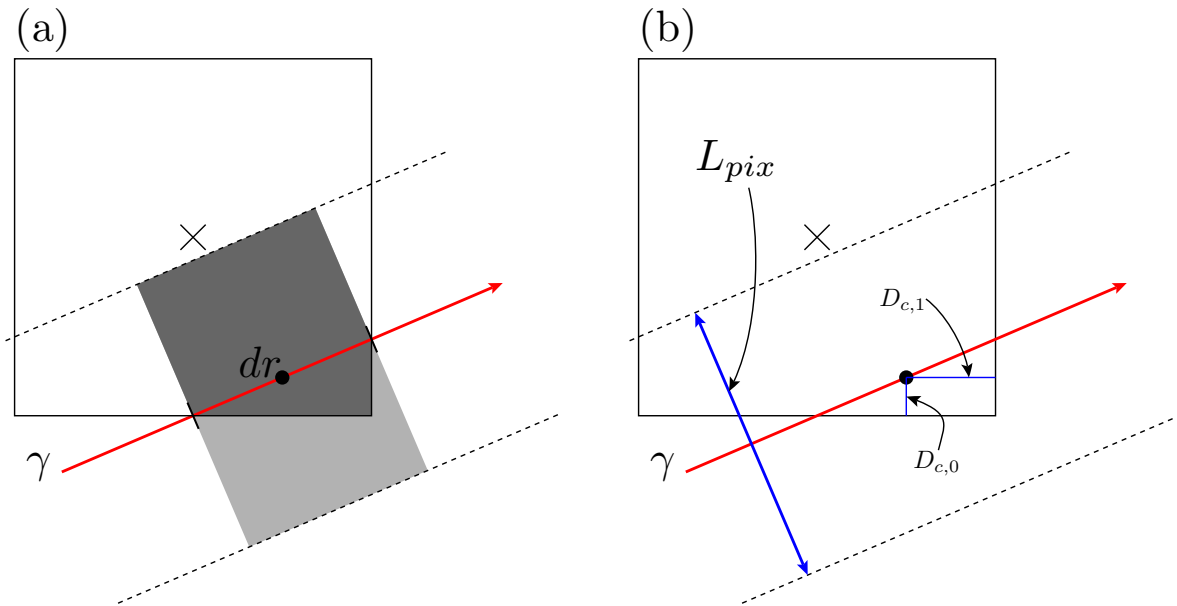
Fig. 1.— (a) A two-dimensional illustration of the overlap between the beam associated with a ray γ and a computational cell. The ray has a segment length of dr passing through the cell. The covering area is denoted by dark grey, where the full area ($dr \times L_{\text{pix}}$) is colored by the dark and light grey. The photo-ionization and photo-heating rates should be corrected by this overlap fraction f_c. (b) Annotation of quantities used in this geometric correction.

The distance to the closest cell boundary is $D_{\text{edge}} = dx/2 - \min_{i=1\to3}(D_{\text{c,i}})$. Thus the covering factor is related to the square of the ratio between the L_{pix} and d_{mid} by

$$f_c = \left(\frac{1}{2} + \frac{D_{\text{edge}}}{L_{\text{pix}}} \right)^2 \tag{23}$$

One half of the pixel is always contained within the cell, which results in the factor of $1/2$. Finally we multiply k_{ph} and Γ_{ph} by f_c but leave the absorbed radiation dP untouched because this would underestimate the attenuation of the incoming radiation. Using f_c calculated like above, the method is no longer photon conserving. In our implementation, we felt that the spherical symmetry obtained outweighed the loss of photon conservation. We show the deviations from fully conservative in §7.1.

We briefly next describe how to retain photon conservation with a geometric correction. Notice that we compute f_c by only considering the distances in orthogonal directions. A better estimate would consider the distance between the cell boundary and ray segment midpoint in the direction of $\mathbf{x}_{\text{mid}} - \mathbf{x}_{\text{center}}$. However we find that the method outlined here provides a sufficient correction factor to avoid any non-spherical artifacts. Furthermore in

principle, the ray should also contribute to any neighboring cells that overlap with $\Omega_{\rm ray}$, which is the key to be photon conservative with such a geometric correction.

2.6. Optically Thin Approximation

When the medium is optically thin to the radiation, radiation is only attenuated by geometric dilution in the local approximation to Eq. (2), i.e. the inverse square law. We can minimize the computational work of ray tracing in the optically thin regime by utilizing this fact. Here we track the total column density $N_{\rm abs}$ and the equivalent total optical depth τ traversed by the photon. If $\tau < \tau_{\rm thin} \sim 0.1$ after the ray exits the cell, we calculate the photo-ionization and photo-heating rates directly from the incoming ray instead of the luminosity of the source. This should only be evaluated once per cell per radiation source.

$$k_{\rm ph} = \frac{\sigma_{\rm abs}\, P}{dt_P\, \theta_{\rm pix}}\, \frac{r_{\rm cell}}{r_{\rm ray}}. \tag{24}$$

Note that the photon number P in the ray has already been geometrically diluted by ray splitting. Here $r_{\rm cell}$ and $r_{\rm ray}$ are the radii from the radiation source to the cell center and where the ray exits the cell. Thus the last factor corrects the flux to a value appropriate for the cell center. The photo-heating ray is calculated in the same manner as the general case, $\Gamma_{\rm ph} = k_{\rm ph}(E_{\rm ph} - E_i)$. No photons are removed from the ray. With this method, we only require one ray travel through each cell where the gas is optically thin, thus reducing the computational expense.

We must be careful not the overestimate the radiation when multiple rays enter a single cell. In the case of a single radiation source, the solution is simple — only assign the cell the photo-ionization and photo-heating rates when $k_{\rm ph} = 0$. However in the case with multiple sources, this is no longer valid, and we must sum the flux from all optically thin sources. Only one ray per source must contribute to a single cell in this framework. We create a flagging field that marks whether a cell has already been touched by an optically thin photon from a particular radiation source. Naively, we would be restricted to tracing rays from a single source at a time if we use a boolean flagging field. However we can trace rays for 32 sources at a time by using bitwise operations on a 32-bit integer field. For example in C, we would check if an optically thin ray from the n-th source has propagated through cell i by evaluating `(MarkerField[i] ≫ n & 1)`. If false, then we can add the optically thin approximation (Eq. 24) to the cell and set `MarkerField[i] |= (1 ≫ n);` to mark the cell.

3. Numerical Implementation in Enzo

Enzo is a parallel block-structured AMR (Berger & Colella 1989) code that is publicly available (Bryan & Norman 1997; O'Shea et al. 2004). In this section, we describe our parallel implementation of the adaptive ray tracing method into *Enzo*. First we explain the programming design of handling the "photon packages" that are traced along the adaptive rays. We use the terms photon packages and rays interchangeably. Next we focus on the details of the radiation hydrodynamics and then the importance of correct time-stepping. Last we give our parallelization strategy of tracing rays through an AMR hierarchy. This implementation is included in the `v2.0` public version of *Enzo*.

3.1. Programming Design

Each photon package is stored in the AMR grid with the finest resolution that contains its current position. The photon packages keep track of their (1) photon flux, (2) photon type, (3) photon energy, (4) the length of its emission, (5) emission time, (6) current time, (7) radius, (8) total column density, (9) HEALPix pixel number, (10) HEALPix level, and (11) position of the originating source, totaling 60 (88) bytes for single (double) precision. When *Enzo* uses double precision for grid and particle positions and time, items 4-7 and 11 are double precision.

We only treat point sources of radiation in our implementation; therefore all base level photon packages originate from them. As they travel away from the source, they generally pass through many AMR grids, especially if the simulation has a high dynamic range. This is a challenging programming task as rays are constantly entering and exiting grids. Before any computation, the number of rays in a particular grid is highly unpredictable because the intervening medium is unknown. Furthermore, the splitting of parent rays into child rays and a dynamic AMR hierarchy add to the complexity. Because of this, we store the photon packages as a doubly linked list (Abel & Wandelt 2002). Thus we can freely add and remove them from grids without the concern of allocating enough memory before the tracing commences.

We illustrate the underlying algorithm of the ray tracing module in *Enzo* in Figure 2 and the ray tracing algorithm is shown in Figure 3. The module is only called when advancing the finest AMR level. We describe its steps below.

Step 1.— Create N_{pix} new photon packages on the initial HEALPix level from point sources. Place the new rays in the highest resolution AMR grid that contains the source.
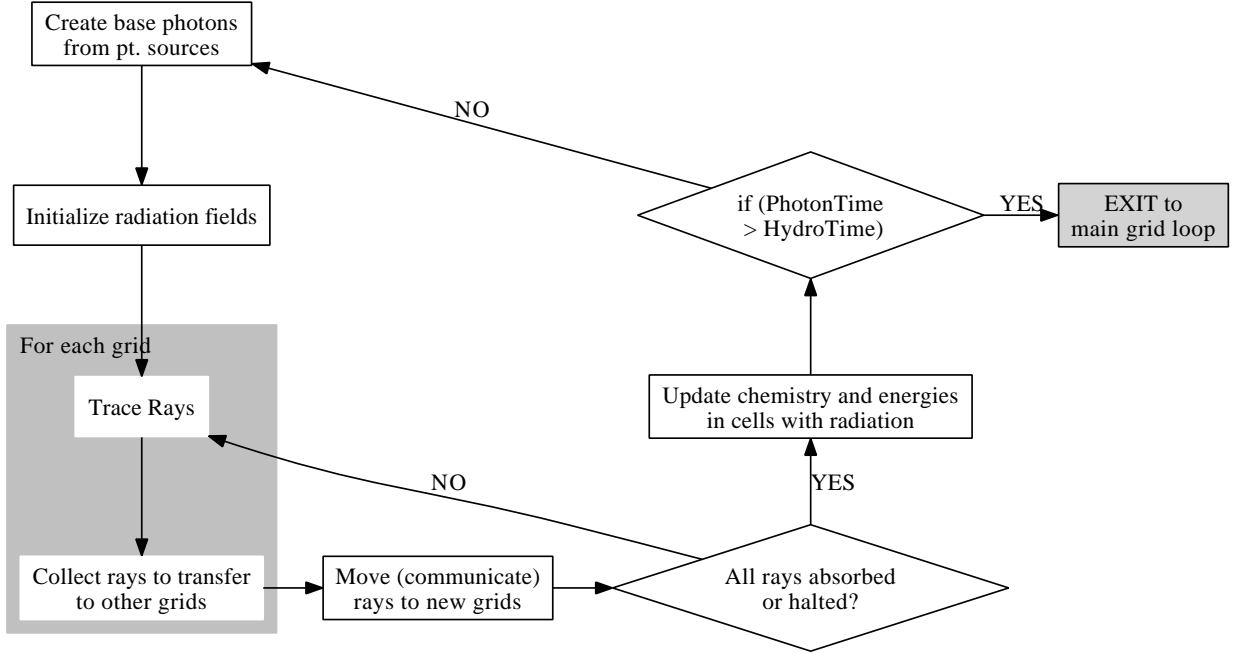
Fig. 2.— Flow chart for the overall algorithm of the radiative transfer module in *Enzo* that illustrates (1) the creation of photon packages, (2) ray tracing, (3) the transport of photon packages between AMR grids, and (4) coupling with the hydrodynamics. The ray tracing algorithm, which is contained in the "Trace Rays" is detailed in Figure 3.

Step 2.— Initialize all radiation fields to zero.

Step 3.— Loop through all AMR grids, tracing any rays that exist in it. For each ray, the following substeps are taken.

Step 3a.— Compute the ray normal based on the HEALPix level and pixel number of the photon package with the HEALpix routine `pix2vec_nest`. One strategy to accelerate the computation is to store ray segment paths in memory (Abel & Wandelt 2002; Krumholz et al. 2007); however this must be recomputed if the grid structure or point source position changes. We do not restrict these two aspects and cannot employ this acceleration method.

Step 3b.— Compute the position of the ray $(\mathbf{r}_{\rm src} + r\hat{\mathbf{n}})$, the current cell coordinates in floating point and its corresponding integer indices. Here $\mathbf{r}_{\rm src}$ is the position of the point source, r is the distance travelled by the ray, and $\hat{\mathbf{n}}$ is the ray normal.

Step 3c.— Check if a subgrid exists under the current cell. If so, move the ray to a linked list that contains all rays that should be moved to other grids. We call this variable `PhotonMoveList`. Store the destination grid number and level. Continue to the next ray in
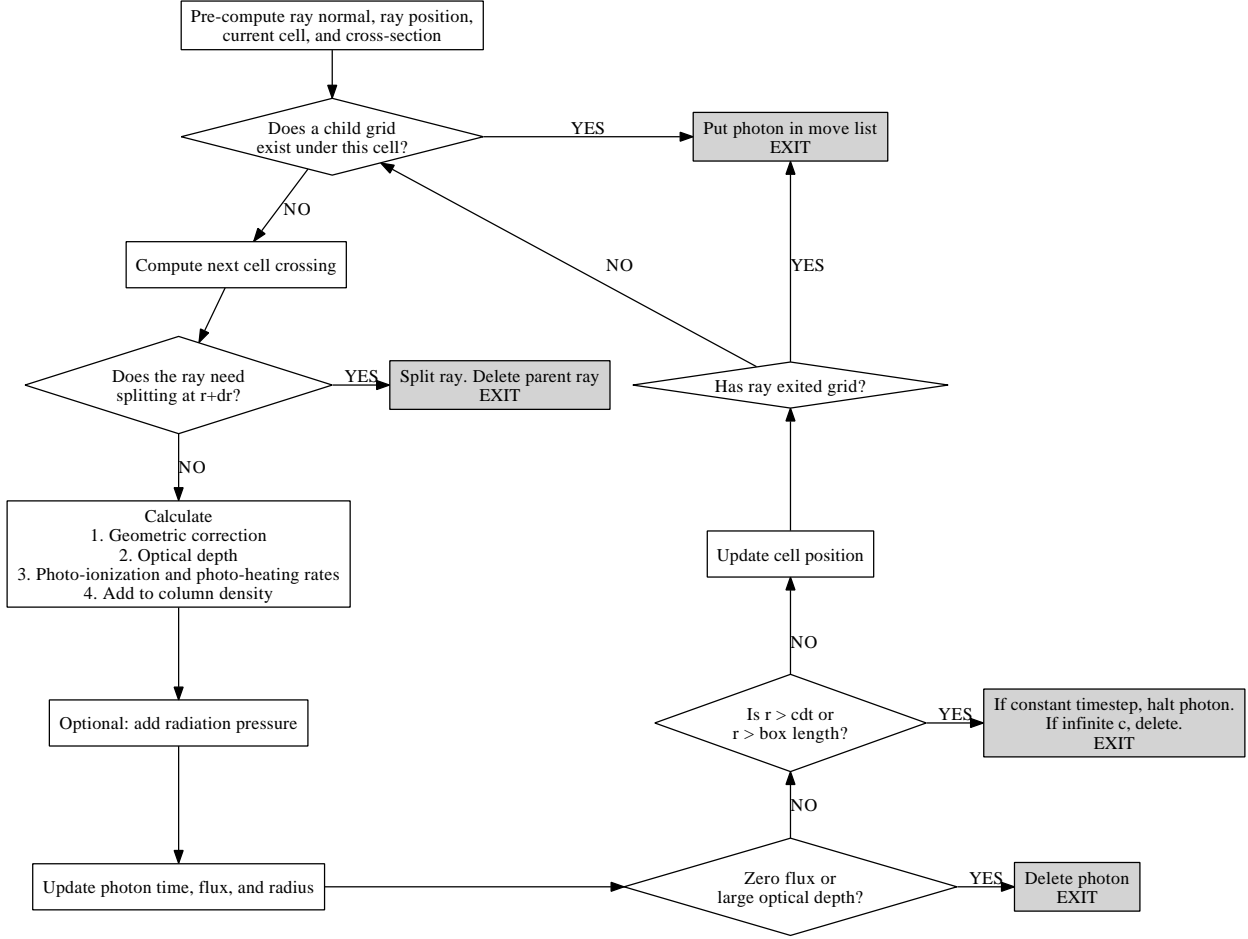
Fig. 3.— Flow chart for the ray tracing algorithm for one photon passing through a grid. Note that only one step is needed in the routine to adaptively split rays. The remainder is a typical ray tracing method.

the grid (step 3a). We determine whether a subgrid exists by creating a temporary 3D field of pointers that either equals the pointer of the current grid if no subgrid exists under the current cell or the child pointer that exists under the current cell. This provides a significant speedup when compared to a simple comparison of a photon package position and all of the child grid boundaries. Note that this is the same algorithm used in *Enzo* when moving collisionless particles to child grids.

Step 3d.— Compute the next cell crossing of the ray and the ray segment length across the cell (Equation 5).

Step 3e.— Compare the solid angle associated with the ray at radius $r + dr$ with a

user-defined splitting criterion (Equation 6). If the solid angle is larger than the desired minimum sampling, split the ray into 4 child rays (§2.1). These rays are inserted into the linked list after the parent ray, which is subsequently deleted. Continue to the next ray (step 3a), which will be the first child ray.

Step 3f.— Calculate the geometric correction (Equation 23), the optical depth of the current cell (Equation 7), photo-ionization and photo-heating rates (Equations 9 and 10), and add the column density of the cell to the total column density of the ray.

Step 3g.— Add the effects of any optional physics modules (§2.4)—secondary ionizations from X-rays, Compton heating from scattering, and radiation pressure.

Step 3h.— Update the current time ($t = t + cdr$), photon flux ($P = P − dP$, Equation 8), and radius of the ray ($r = r + dr$).

Step 3i.— If the photon flux is zero or the total optical depth is large (> 20), delete the ray.

Step 3j.— Check if the ray has travelled a total distance of cdt_P in the last timestep. If we are keeping the time-derivative of the radiative transfer equation, halt the photon. If not (i.e. infinite speed of light), delete the photon.

Step 3k.— Check if the ray has exited the current grid. If false, continue to the next ray (step 3a). If true, move the ray to the linked list `PhotonMoveList`, similar to step 3c. If the ray exits the simulation domain, delete it if the boundary conditions are isolated; otherwise, we change the source position of the ray by a distance `-sign(n[i]) * DomainWidth[i]`, where `n` is the ray normal, and `i` is the dimension of the outer boundary it has crossed. The radius is kept unchanged. In essence, this creates a "virtual source" outside the box because the ray will be moved to the opposite side of the domain, appearing that it originated from this virtual source.

Step 4.— If any rays exist in the linked list `PhotonMoveList`, move them to their destination grids and return to step 3. This requires MPI communication if the destination grid exists on another processor.

Step 5.— If all rays have not been halted (keeping the time-derivative of the radiative transfer equation), absorbed, or exited the domain, return to step 3.

Step 6.— With the radiation fields updated, call the chemistry and energy solver and update only the cells with radiation, which is discussed further in §3.3.

Step 7.— Advance the time associated with the photons t_P by the global timestep dt_P (for its calculation, see §3.4). If t_P does not exceed the time on the finest AMR level, return

to step 1.

3.2. Energy groups

In our implementation, photon packages are mono-chromatic, i.e. energy groups (Mihalas & Mihalas 1984, Ch. 6), and are assigned a photon type that corresponds whether it is a photon that (1) ionizes hydrogen, (2) singly ionizes helium, (3) doubly ionizes helium, (4) has an X-ray energy, or (5) dissociates molecular hydrogen (Lyman-Werner radiation). One disadvantage of mono-chromatic rays is the number of rays increase with the number of frequency bins. However this allows for early termination of rays that are fully absorbed, which are likely to have high absorption cross-sections (e.g. H I ionizations near 13.6 eV) or a low initial intensity (e.g. He II ionizing photons in typical stellar populations). The other approach used by some groups (e.g. Trac & Cen 2007) is to store all energy groups in a single ray. This reduces the number of the rays generated and the computation associated with the ray tracing. Unless the ray dynamically adjusts its memory allocation for the energy groups as they become depleted, this method is also memory intensive in the situation where most of the energy groups are completely absorbed but a few groups still have significant flux.

In practice, we have found that one energy group per photon type is sufficient to match expected analytical tests. For example when modeling Population III stellar radiation (e.g. Abel et al. 2007; Wise & Abel 2008b, for hydrogen ionizing radiation only), we have 3 energy groups—H I, He I, He II—each with an energy that equals the average photon energy above the ionization threshold.

3.3. Coupling with Hydrodynamics

Solving the radiative transfer equation is already an intensive task, but coupling the effects of radiation to the gas dynamics is even more difficult because the radiation fields must be updated on a timescale such that it can react to the radiative heating, i.e. sound-crossing time. The frequency of its evaluation will be discussed in the next section.

Enzo solves the physical equations in an operator-split fashion over a loop of AMR grids. On the finest AMR level, we call our radiation transport solver before this main grid loop in the following sequence:

- **All grids:**

    1. Solve for the radiation field with the adaptive ray tracer

2. Update species fractions and energies for cells with radiation with a non-equilibrium chemistry solver on subcycles (Equation 25).

- **For each grid:**

    1. Solve for the gravitational potential with the particle mesh method

    2. Solve hydrodynamics

    3. Update species fractions and energies for cells without radiation with a non-equilibrium chemistry solver on subcycles (Equation 25).

    4. Update particle positions

    5. Star particle formation

- **All grids:** Update solution from children grids

Since the solver must be called many times, the efficiency of the radiation solver is paramount. After every radiation timestep, we call the non-equilibrium chemistry and energy solver in *Enzo*. This solves both the energy equation and the network of stiff chemical equations on small timesteps, i.e. subcycles (Anninos et al. 1997). The timestep is

$$dt = \min\left(\frac{0.1n_e}{|dn_e/dt|}, \frac{0.1n_{\mathrm{HI}}}{|dn_{\mathrm{HI}}/dt|}, \frac{0.1e}{|de/dt|}, \frac{dt_{\mathrm{hydro}}}{2}\right), \tag{25}$$

where n_e is the electron number density, e is the specific energy, and dt_{hydro} is the hydrodynamic timestep. This limits the subcycle timestep to a 10% change in either electron density, neutral hydrogen density, or specific energy. In simulations without radiation, *Enzo* calls this solver in a operation-split manner after the hydrodynamics module for grids only on the AMR level that is being solved. In simulations with radiative transfer, the radiation field can change on much faster timescales than the normal hydrodynamical timesteps.

For example, a grid on level L might have no radiation in its initial evaluation, but the ionization front exists just outside its boundary. Then radiation permeates the grid in the time between $t_{\mathrm{L}=1} \rightarrow t_{\mathrm{L}=1} + dt_{\mathrm{L}=1}$, and the energy and chemical state of the cells must be updated again to advance the ionization front accurately. If one does not update these cells, it will appear that the ionization front does not enter the grid until the next hydrodynamical timestep! Visually this appears as discontinuities in the temperature and electron fraction on grid boundaries. One may avert this problem by solving the chemistry and energy equations for every cell on every radiative transfer timestep, but this is very time consuming and unnecessary, especially if the radiation filling factor is small.

We choose to dynamically split the problem by cells with and without radiation. In every radiation timestep, the chemo-thermal state of *only* the cells with radiation are updated.

For the solver subcycling, we replace dt_{hydro} with dt_P in Equation 25 in this case. Once the radiative transfer solver is finished with its timesteps, the hydrodynamic module is called, and then the chemo-thermal state of the cells without radiation are updated on a subcycle timestep stated in Equation 25.

For cells that transition from zero to non-zero photo-ionization rates, the initial state that enters into the chemistry and energy solver does not correspond to the current time of the radiation transport solver t_{RT}, but either time t_{L} if the grid level is the finest level because its chemo-thermal state has not been updated or time $t_{\text{L}}+dt_{\text{L}}$ on all other levels. In principle, one could first revert the cell back to time t_{L} and then update to t_{RT} with the chemistry and energy solver if the cell is on the finest level. However in practice, the timescales in gas without radiation are small compared to the ionization and heating timescales when radiation is introduced. Therefore, we do not perform this correction and find that this does not introduce any inaccuracies in both test problems (see §4) and real world applications.

3.4. Temporal evolution

There have been several methods of choosing a timestep to solve radiation transfer equation because an accurate yet large timestep is not trivial to compute. We describe several methods to calculate the radiative transfer timestep in this section. With a small enough timestep, the solution is guaranteed to avoid any inaccuracies (ignoring any systematic ones) due to time-stepping, but the solver must be called many times. These frequent calls may be unnecessary because the same solution may be accomplished with a longer timestep. Furthermore with ray tracing, the photon packages only advance a short distance, and they will exist in every dx/dt_P cells with radiation and are stored between timesteps, excessively consuming memory. On the shortest timescale, one can safely set the timestep to the light-crossing time of a cell (Abel et al. 1999; Trac & Cen 2007) but encounters the problems stated above.

If the timestep is too large, the solution will become inaccurate; specifically, ionization fronts will advance too slowly, as radiation intensity exponentially drops with a scale length of the mean free path

$$\lambda_{\text{mfp}} = \frac{1}{n_{\text{abs}}\ \sigma_{\text{abs}}} \tag{26}$$

past the ionization front. For example in our implementation, the chemo-thermal state of the system remains constant as the rays are traced through the cells. Thus in the case of a single H II region, the speed of the ionization front is limited to approximately the $\lambda_{\text{mfp}}/dt_P$.
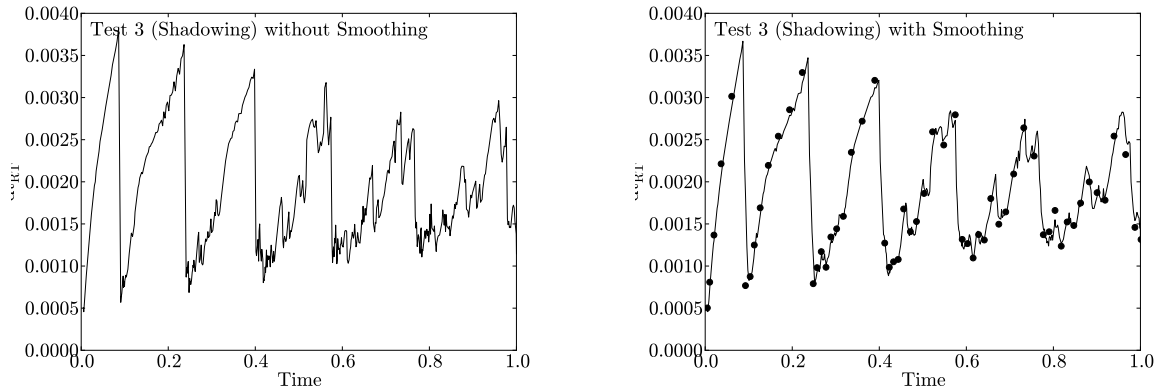
Fig. 4.— Radiative transfer adaptive timestep in shadowing test (Test 3; §4.3) while restricting the neutral fraction change to 5% in the ionization front. The unmodified timestep (left) is slightly more noisy and the minima are more prominent than the timestep computed with a running average of the last two timesteps (right). The points show every tenth timestep taken into account for the running average. The sawtooth behavior is created by the ionization front advancing into the next neutral cell in the overdensity.

3.4.1. Minimizing neutral fraction change

Another strategy is only allowing the neutral fraction of the ionized gas to change a small amount, i.e. for a single cell,

$$dt_{\text{P,cell}} = \epsilon_{\text{ion}} \frac{n_{\text{HI}}}{|dn_{\text{HI}}/dt|} = \frac{\epsilon_{\text{ion}}}{|k_{\text{ph}} + n_e(C_{\text{H}} + \alpha_B)|}, \qquad (27)$$

where ϵ_{ion} is the maximum fraction change in neutral fraction. Shapiro et al. (2004) found that this limited the speed of the ionization front. We can investigate this further by evaluating the ionization front velocity in a growing Strömgren sphere without recombinations, where $\dot{N}_\gamma = 4\pi R^2 n_{\text{H}} v_{\text{IF}}$. Using $k_{\text{ph}} \propto \dot{n}_{\text{H}}/n_{\text{H}}$ and $k_{\text{ph}} = \dot{N}_\gamma \sigma/4\pi R^2 A_{\text{cell}}$, we can make substitutions on both sides of the equation to arrive at the ionization front velocity $v_{\text{IF}} \propto n_{\text{H}}/\dot{n}_{\text{H}}$.

We have implemented this method but we only consider cells within the ionization front (by experiment we choose $\tau > 0.5$) because we are interested in evolving ionization fronts at the correct speed. In the ionized region, the absolute changes in neutral fraction are small and will not significantly affect the ionization front evolution. In other words, $n_{\text{HI}}/(dn_{\text{HI}}/dt)$ may be large but $(dn_{\text{HI}}/dt) \sim 0$, thus we can safely ignore these cells when determining the timestep without sacrificing accuracy.

We search for the cell with the smallest dt_P based on Equation 27. In principle, one could use this value without modifications as the timestep, but there is considerable noise

both spatially and temporally. In order to make this technique stable, we first spatially smooth the values of $dt_{\mathrm{P,cell}}$ with a Gaussian filter over a 3^3 cube. Because we only consider the cells within the ionization front, we set $dt_{\mathrm{P,cell}}$ to the hydrodynamical timestep outside the front during the smoothing. After we have smoothed $dt_{\mathrm{P,cell}}$, we select the minimum value as dt_P. Significant noise in dt_P can exist between time discretizations. Because the solution can become inaccurate if the timestep is allowed to be too large, we restrict the next timestep to be less than twice the previous timestep,

$$dt_{\mathrm{P,1}} = \min(2dt_{\mathrm{P,0}},\ dt_{\mathrm{P,1}}). \tag{28}$$

Otherwise, we still restrict the change in timestep by setting the next timestep to be the average of the previous timestep $dt_{\mathrm{P,0}}$ and $\min(dt_{\mathrm{P,cell}})$. Figure 4 shows the smooth evolution of dt_{P} in a growing Strömgren sphere when compared to the values of $\min(dt_{\mathrm{P,cell}})$.

3.4.2. Time averaged quantities within a timestep

Mellema et al. (2006) devised an iterative scheme that allows for large timesteps while retaining accuracy by considering the time-averaged values (τ, k_{ph}, n_e, n_{HI}) during the timestep. Starting with the cells closest to the source, they first calculate the column density to the cell. Then they compute the time-averaged neutral density for the cell and its associated optical depth, which is added to the total time-averaged optical depth. With these quantities, one can compute a photo-ionization rate and update the electron density. This process is repeated until convergence is found in the neutral number density. In a test with a Strömgren sphere, they found analytical agreement with 10^{-3} less timesteps than a method without time-averaging. Another advantage of this method is the use of pre-calculated tables for the photo-ionization rates as a function of optical depth, based on a given spectrum. This minimizes the energy groups needed to accurately sample a spectrum. We are currently implementing this method into Enzo+Moray.

3.4.3. Physically motivated

In our implementation, a constant timestep is necessary when solving the time-dependent radiative transfer equation. It should be small enough to evolve ionization fronts accurately, as discussed earlier. The timestep can be based on physical arguments, for example, the sound-crossing time of an ionized region at $T > 10^4$ K. To be conservative, one may choose the sound-crossing time of a cell (e.g. Abel et al. 2007; Wise & Abel 2008b). Alternatively, the diameter of the smallest relevant system (e.g., an accretion radius, transition radius to a

D-type ionization front, etc.) in the simulation may be chosen to calculate the sound-crossing time.

If the timestep is too large, the ionization front will propagate too slowly, but it eventually approaches the correct radius at late times (see §6.4). This does not prevent one from using a large timestep, particularly if the system is not critically affected by a slower I-front velocity. One example is an expanding H II region in a power-law density gradient. After a brief, initial R-type phase, the I-front becomes D-type phase, where the ionization and shock front progress jointly at the sound speed of the ionized region. A moderately large (0.1 Myr) timestep can accurately follow its evolution. However after the I-front passes a critical radius (Franco et al. 1990), the I-front detaches from the shock front, accelerates, and transitions back to an R-type front. This can also occur in champagne flows when the ionization front passes a density discontinuity. The I-front velocities in these two stages differ up to a factor of ~ 10. Although the solution is accurate with a large timestep in the D-type phase, the I-front may lag behind because of the constant timestep. After a few recombination times, the numerical solution eventually approaches the analytical solution. If such a simulation focuses on the density core expansion and any small scale structures, such as cometary structures and photo-dissociation regions, one can cautiously sacrifice temporal accuracy at large scales for computational savings.

3.4.4.   Change of incident radiation

Ionization front velocities can approach significant fractions of the speed of light in steep density gradients and in the early expansion of the H II region. If the ionization front position is critical to the calculation, the radiation transport timestep can be derived from an estimate of the ionization front velocity

$$v_{\mathrm{IF}}(\mathbf{r}) \approx \frac{F(\mathbf{r})}{n_{\mathrm{abs}}(\mathbf{r})}, \tag{29}$$

based on the incident radiation field at a particular position. The timestep is then chosen so that the ionization front only crosses one cell per timestep $dt_{\mathrm{P,cell}} = dx/v_{\mathrm{IF}}$, and the global timestep is $dt_{\mathrm{P}} = \min(dt_{\mathrm{P,cell}})$.

To make this approach computationally straightforward, we consider a spherically symmetric case without recombinations. Thus all photons emitted from the source result in an ionization (also see §3.4.1). Ultimately in any approach, we are focused on accurately following the time evolution of the radiation field. In this method, we base the timestep directly on the change in radiation field, the specific intensity, $I/\dot{I}$. We consider the field

after propagating through the cell, so $I = I_0 \exp(-\tau)$, where $\tau = n_{\mathrm{H}}\sigma dl$ is the optical depth through the cell. The change in specific intensity is

$$\frac{dI}{dt} = I_0 \exp(-\tau)(-\dot{n}_{\mathrm{H}}\sigma dl), \tag{30}$$

which can be expressed in terms of local optical depth and neutral fraction,

$$\frac{dI}{dt} = -I\frac{\tau\dot{n}_{\mathrm{H}}}{n_{\mathrm{H}}}. \tag{31}$$

This results in a local timestep

$$dt_P = \frac{I}{|dI/dt|} = C_{\mathrm{RT,cfl}}\frac{n_{\mathrm{H}}}{\tau\dot{n}_{\mathrm{H}}}, \tag{32}$$

where $C_{\mathrm{RT,cfl}}$ is a safety factor that restricts the change in intensity to its inverse. In practice, we have found that a ceiling of 3 can be placed on the optical depth, so optically thick cells do not create a very small timestep. We still find excellent agreement with analytical solutions with this approximation. We show the accuracy using this timestep method in §6.4.

3.5.   Parallelization Strategy

Parallelization of the ray tracing code is essential when exploring problems that require high resolution and thus large memory requirements. Furthermore, *Enzo* is already parallelized and scalable to $O(10^2)$ processors in AMR simulations, and $O(10^3)$ in unigrid calculations. *Enzo* stores the AMR grid structure on every processor, but only one processor contains the actual grid and particle data and photon packages. All other processors contain an empty grid container. As discussed in *Step 4* in §3.1, we store the photon packages that need to be transferred to other grids in the linked list `PhotonMoveList`. In a single processor (serial) run, moving the rays is trivial by inserting these photons into the linked list of the destination grid. For multi-processor runs, we must send these photons through MPI communication to the processors that host the data of the destination grids. We describe our strategy below.

The easiest case is when the destination grid exists on the same processor as the source grid, where we move the ray as in the serial case. For all other rays, we organize the rays by destination processors and send them in groups. We also send the destination grid level and ID number along with the ray information, which is listed at the beginning of §3.1.

For maximum overlap of communication and computation, which enables scaling to large numbers of processors, we must employ "non-blocking" MPI communication, where each

processor does not wait for synchronization with other processors. We use this technique for the sending and receiving of rays. Here we desire to minimize the idle time of each processor when it is waiting to receive data. In the loop shown in Figure 2 with the conditional that checks whether we have traced all of the rays, we aggressively transport rays that are local on the processor, and process any MPI receive calls as they arrive, not waiting for their completion in order to continue to the next iteration. We describe the steps in this algorithm next.

Step 1.— Before any communication occurs, we count the number of rays that will be sent to each processor. The MPI receive calls (MPI_Irecv) must have a data buffer that is greater than or equal to the size of the message. We choose to send a maximum of N_{max} (= 10^5 in *Enzo* v2.0) rays per MPI message. Therefore, we allocate a buffer of this size for each MPI_Irecv call. We then determine the number of MPI messages N_{mesg} and send this number in a non-blocking fashion, i.e. MPI_Isend.

Step 2.— Pack the photon packages into a contiguous array for MPI communication while the messages from Step 1 completes.

Step 3.— Process the number of photon messages that we are expecting from each processor, sent in Step 1. Then post this number of MPI_Irecv calls for the photon data. Because we strive to make the ray tracing routine to be totally non-blocking, the processors will most likely not be synchronized on the same loop (Steps 3–5 in §3.1). Therefore, there might be additional N_{mesg} MPI messages waiting to be processed. We check for these messages and aggressively drain the message stack to determine the total number of photon messages that we are expecting and post their associated MPI_Irecv calls for the photon data.

Step 4.— Send the grouped photon data with MPI_Isend with a maximum size of N_{max} photons.

Step 5.— Place any received photon data into the destination grids. We monitor whether the processor has any rays that were moved to grids on the same processor. If so, this processor has rays to transport, and we do not necessarily have to wait for any MPI receive messages and thus use MPI_Testsome to receive any messages that have already arrived. If not, we call MPI_Waitsome to wait for any MPI receive messages.

Step 6.— If all processors have exhausted their workload, then all rays have been either absorbed, exited the domain, or halted after travelling a distance cdt_P. We check this in a similar non-blocking manner as the N_{mesg} calls in Step 1.

Lastly we have experimented with a hybrid OpenMP/MPI version of *Enzo*, where work-

load is partitioned over grids on each MPI process. We found that parallelization over grids for the photon transport does not scale well, and threading over the rays in each grid is a better approach. Because the rays are stored in a linked list in each grid, we must manually split the list into separate lists and let each thread work on each list.

4. Radiative Transfer Tests

Tests plays an important role in creating and maintaining computational tools. In this section, we present tests drawn from the Cosmological Radiative Transfer Codes Comparison Project (Iliev et al. 2006a), where results from 11 different radiative transfer codes compared results in four test problems. The codes use various methods for radiation transport: ray tracing with short, long, and hybrid characteristics, Monte Carlo casting; ionization front tracking (Alvarez et al. 2006b); variable Eddington Tensor formalism (Gnedin & Abel 2001). They conducted tests that investigated (1) the growth of a single Strömgren sphere enforcing isothermal conditions, (2) the same test with an evolving temperature field, (3) shadowing created by a dense, optically thick clump, and (4) multiple H II regions in a cosmological density field. In all of the tests presented here, we use the method of restricted neutral fraction changes (§3.4.1) for choosing a radiative transfer timestep. We cast 48 rays (HEALPix level 1) from the point source and require a sampling of at least $\Phi_c = 5.1$ rays per cell.

4.1. Test 1. Pure hydrogen isothermal H II region expansion

The expansion of an ionizing region with a central source in a uniform medium is a classic problem first studied by Strömgren (1939). This simple but useful test can uncover any asymmetries or artifacts that may arise from deficiencies in the method or newly introduced bugs in the development process. In this problem, the ionized region grows until recombinations balance photo-ionizations (Eq. 1). The evolution of the radius r_s and velocity v_s of the ionization front has an exact solution of

$$r_s(t) = R_s[1 - \exp(-t/t_{\rm rec})]^{1/3} \tag{33}$$

$$v_s(t) = \frac{R_s}{3t_{\rm rec}}\frac{\exp(-t/t_{\rm rec})}{[1 - \exp(-t/t_{\rm rec})]^{2/3}}, \tag{34}$$

where $t_{\rm rec} = (\alpha_{\rm B} n_H)^{-1}$ is the recombination time.

We adopt the problem parameters used in RT06. The ionizing source emits 5×10^{48} ph s^{-1} of monochromatic radiation at 13.6 eV and is located at the origin in a simulation box of
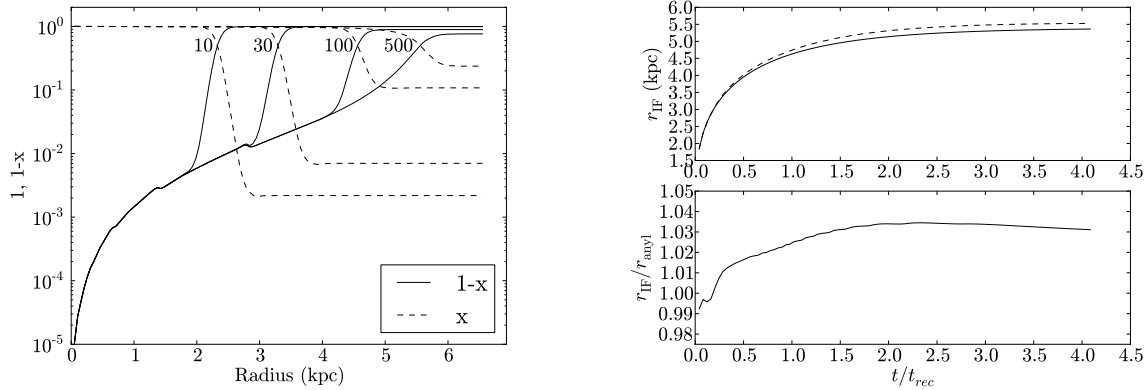
Fig. 5.— Test 1 (H II region expansion with a monochromatic spectrum of 13.6 eV). Left: Radially averaged profile of neutral (solid) and ionized (dashed) fraction at 10, 30, 100, and 500 Myr. Right: Evolution of the calculated (top, dashed) and analytical (top, solid) Strömgren radius. The ratio of these radii are plotted in the bottom panel.

6.6 kpc. The ambient medium is initially set at $T = 10^4$ K, $n_H = 10^{-3} \mathrm{cm}^{-3}$, $x = 1.2 \times 10^{-3}$, resulting in $R_s = 5.4$ kpc and $t_{\mathrm{rec}} = 122.4$ Myr. The problem is run for 500 Myr. In the original tests, the temperature is fixed at 10^4 K; however, our solver is inherently tied to the chemistry and energy solver. To mimic an isothermal behavior, we set the adiabatic index $\gamma = 1.0001$, which ensures an isothermal state but not a fixed ionization fraction outside of the Strömgren sphere.

In Figure 5, we show (a) the evolution of the neutral and ionization fraction as a function of radius at $t = 10, 30, 100$, and 500 Myr, and (b) the growth of the ionization front radius as a function of time and its ratio with the analytical Strömgren radius (Eq. 33). The ionization front has a width of ~ 0.7 kpc, which is in agreement with the inherent thickness of $\sim 18 \lambda_{\mathrm{mfp}} = 0.74$ kpc, given a 13.6 eV mono-chromatic spectrum. There are small kinks in the neutral fraction at 1.5 and 3 kpc that corresponds to artifacts created by the photon package splitting at these radii. However these do not affect the overall solution. One difference between our results and the codes presented in RT06 is the increasing neutral fraction outside of the H II. This occurs because the initial ionized fraction and temperature is set to 1.3×10^{-3} and 8000 K, which are not the equilibrium values. Over the 500 Myr in the calculation, the neutral fraction increases to 0.2, which is close to its equilibrium value. In the right panel of Figure 5, the ionization front radius exceeds R_s by a few percent for most of the calculation. This difference happens because the analytical solution (Eq. 33) assumes the H II region has a constant ionized fraction. The evolution of the ionized fraction as a function of radius can be analytically calculated (e.g. Osterbrock 1989; Petkova & Springel
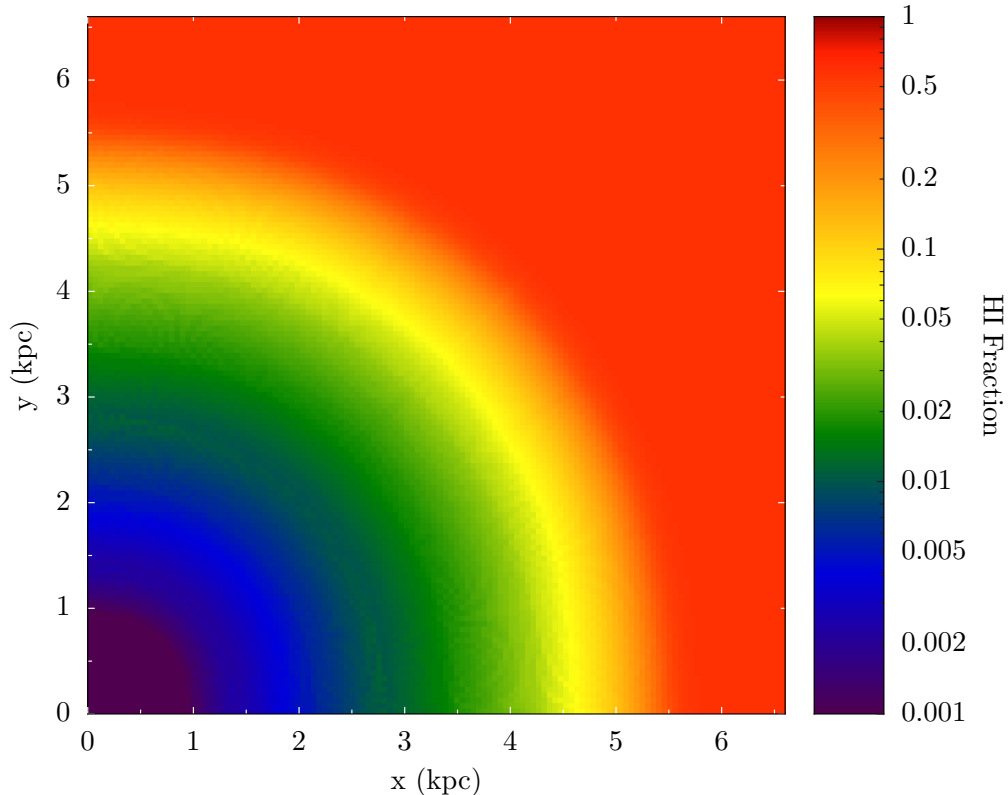
Fig. 6.— Test 1 (H II region expansion with a monochromatic spectrum of 13.6 eV). Slice of neutral fraction at the origin at 500 Myr.

2009), causing the ionization front radius to be slightly larger, increasing from 0 to 3% in the interval 80–350 Myr. Our results are in excellent agreement with this more accurate analytical solution. In Figure 6, we show a slice of the neutral fraction through the origin. Other than the ray splitting artifacts that generate the plateaus at 1.5 and 3 kpc, one sees spherical symmetry in our solution.

4.2. Test 2. H II region expansion: temperature evolution

This test is similar Test 1, but the temperature is allowed to evolve The radiation source now has a blackbody spectrum with a $T = 10^5$ K. The initial temperature is set at 100 K. The higher energy photons have a longer mean free path than the photons at the ionization threshold in Test 1. Thus the ionization front is thicker as the photons can penetrate deeper into the neutral medium. Here we use 4 energy groups with the following mean energies and relative luminosities: $E_i = (16.74, 24.65, 34.49, 52.06)$, $L_i/L = (0.277, 0.335, 0.2, 0.188)$.
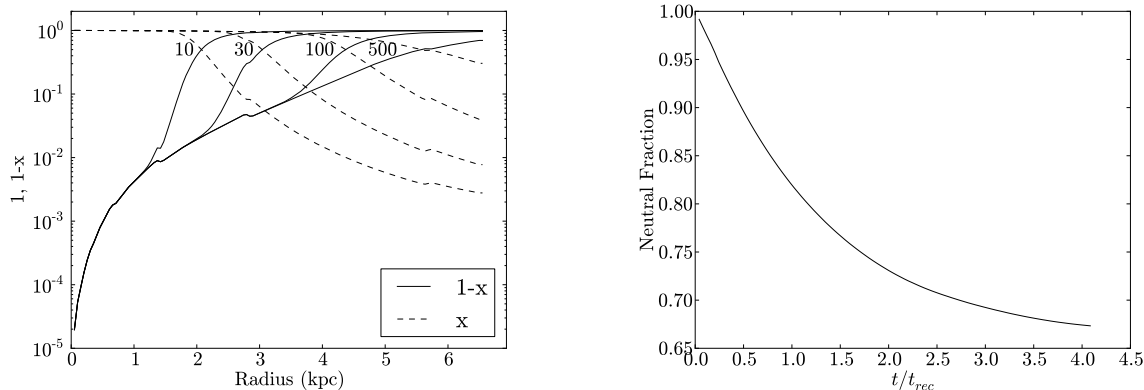
Fig. 7.— Test 2. (H II region expansion with a $T = 10^5$ K blackbody spectrum). Left: Radially averaged profile of neutral (solid) and ionized (dashed) fraction at 10, 30, 100, and 500 Myr. Right: Evolution of the average neutral fraction.

In Figure 7, we show the neutral and ionized fraction as a function of radius at $t = 10$, 30, 100, and 500 Myr, and the total neutral fraction of the domain. Compared with Test 1, the ionization front is thicker, as expected with the harder spectrum. The total neutral fraction decreases to 0.67 over $4t_{\rm rec} = 500$ Myr, which is in agreement with the analytical expectation and other codes in RT06. In Figure 8, we show the ratio of the ionization front radius $r_{\rm IF}$ in our simulation and R_s. Before $1.5t_{\rm rec}$, $r_{\rm IF}$ lags behind R_s, initially by 10% and then increases to R_s; however afterwards, this ratio asymptotes to a solution that is 4% greater than R_s. This behavior puts our code is approximately the median result in RT06, where this ratio varies between 1 and 1.1, and the early evolution of $r_{\rm IF}$ is under-predicted by almost all of the codes. If we use one energy group with the mean energy (29.6 eV) of a $T = 10^5$ K blackbody, we find that $r_{\rm IF}/R_s = 1.08$, which is representative of the codes in the upper range of RT06. In Figure 9, we show slices of neutral fraction and temperature through the origin at $t = 10$ and 100 Myr. Here one sees the spherically symmetric H II regions and a smooth temperature transition to the neutral ambient medium.

4.3. Test 3. I-front trapping in a dense clump and the formation of a shadow

The diffusivity and angular resolution of a radiative transport method can be tested with the trapping of an ionization front by a dense, neutral clump. In this situation, the ionization front will uniformly propagate until it reaches the clump surface. Then the radiation in the line of sight of the clump will be absorbed more than the ambient medium. If the clump is optically thick, a shadow will form behind the clump. The sharpness of the ionization front
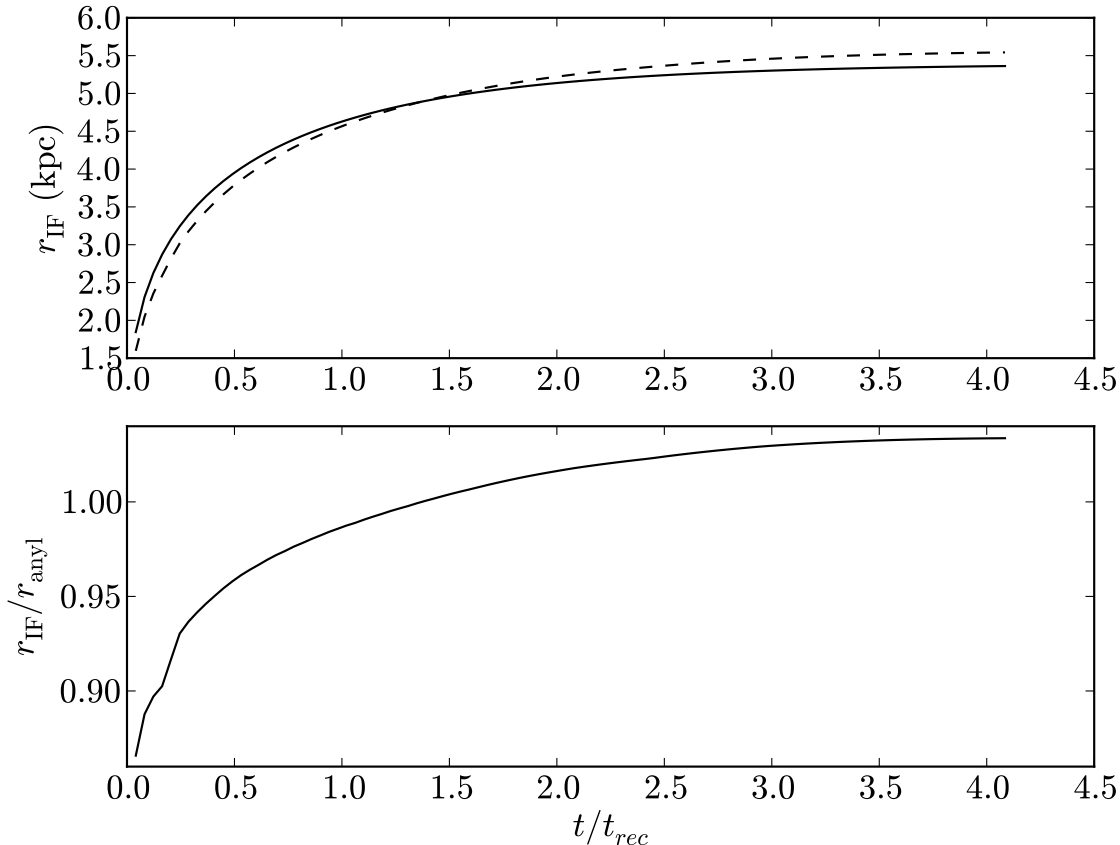
Fig. 8.— Test 2. (H II region expansion with a $T = 10^5$ K blackbody spectrum). Top: Evolution of the radius of the simulated ionization front (dashed) and analytical (solid) Strömgren radius. Bottom: The ratio of the calculated and analytical Strömgren radius.

at the shadow surface can be used to determine the diffusivity of the method. Furthermore the shadow surface should be aligned with the outermost neutral regions of the clump, which can visually assess the angular resolution of the method.

The problem for this test is contained in a 6.6 kpc box with an ambient medium of $n_H = 2 \times 10^{-4} \mathrm{cm}^{-3}$ and $T = 8000$ K. The clump is in pressure equilibrium with $n_H = 0.04 \mathrm{cm}^{-3}$ and $T = 40$ K. It has a radius of $r_c = 0.8$ kpc and is centered at $(x, y, z) = (5, 3.3, 3.3)$ kpc. In RT06, the test considered a plane parallel radiation field with a flux $F_0 = 10^6$ ph s^{-1} cm^{-2} originating from the $y = 0$ plane. Our code can only consider point sources, so we use a single radiation source located in the center of the $y = 0$ boundary. The luminosity of $\dot{N}_\gamma = 3 \times 10^{51}$ ph s^{-1} corresponds to the same flux F_0. The location where the ionization front
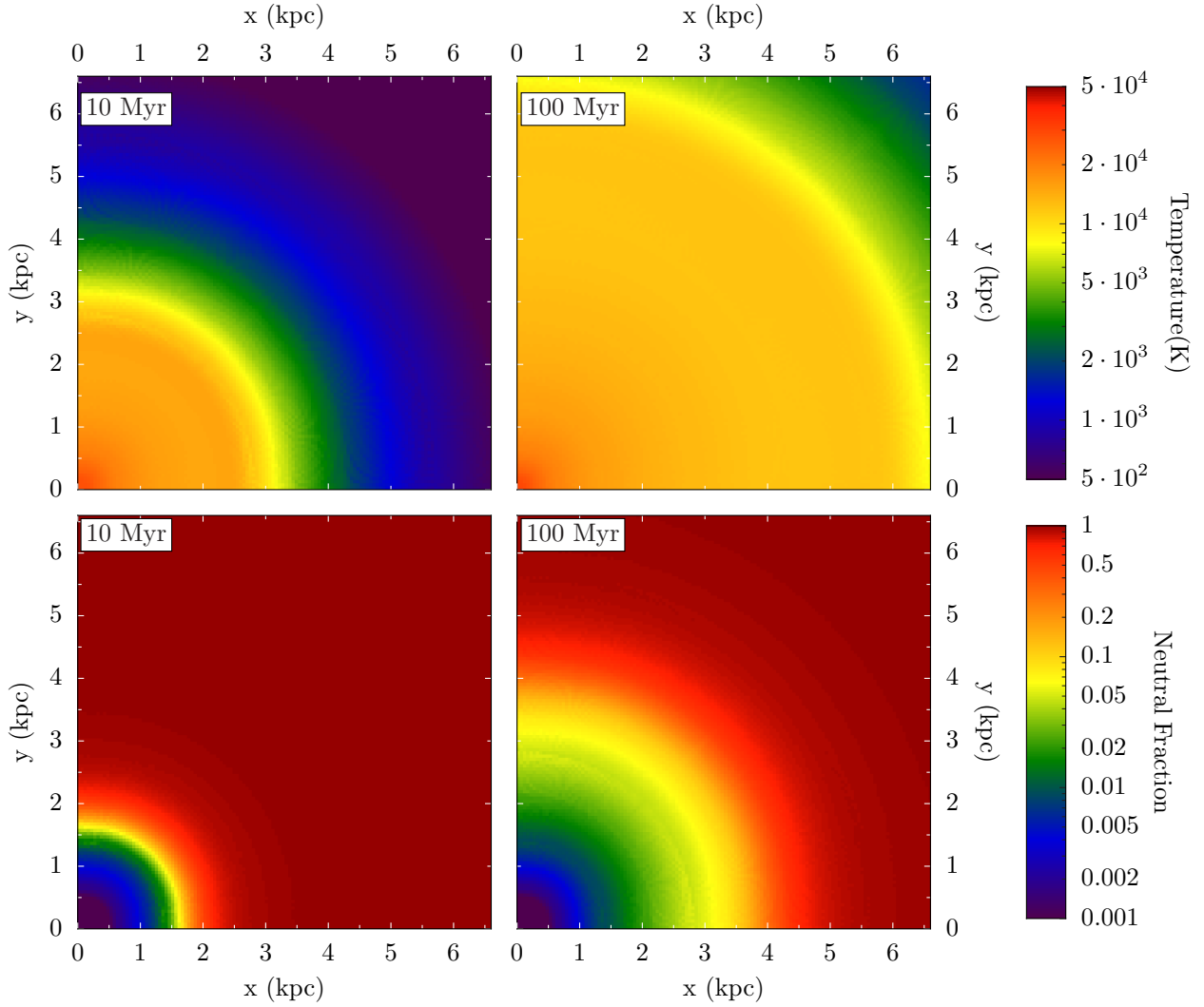
Fig. 9.— Test 2. (H II region expansion with a $T = 10^5$ K blackbody spectrum). Top: Slices through the origin of neutral fraction at 10 and 100 Myr. Bottom: Slices of temperature at 10 and 100 Myr.
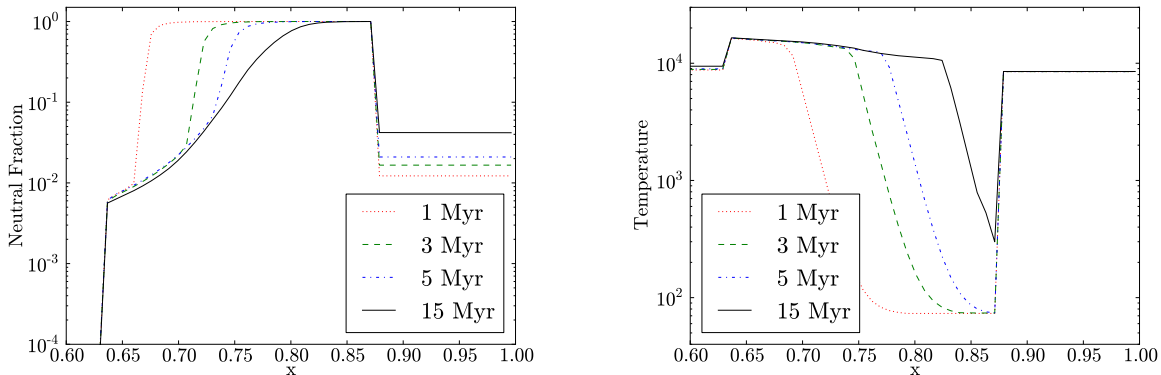
Fig. 10.— Test 3. (I-front trapping in a dense clump and shadowing). Left panel: Line cut from the point source through the middle of the dense clump at $t = 1, 3, 5, 15$ Myr. of the average neutral fraction (left) and temperature (right) of the clump.

trapping can be calculated analytically (Shapiro et al. 2004), and with these parameters, it should halt at approximately the center of the clump. We use the same four energy groups as in Test 2.

In Figure 10, we show neutral fraction and temperature of a one-dimensional cut through the center of the dense clump at $z = 0.5$ at $t = 1, 3, 5, 15$ Myr. The ionization front is halted at a little more than halfway through the clump, which is consistent with the analytical expectation. The hardness of the $T = 10^5$ K blackbody spectrum allows the gas outside of the ionization front. Where the gas is ionized, the temperature is between 10,000 and 20,000 K, but decreases sharply with the ionized fraction. Figure 11 depicts the average ionized fraction and temperature inside the dense clump, which both gradually increase as the ionization front propagates through the overdensity. Our results are consistent with RT06. Finally we show slices of neutral fraction and temperature in the $z = 0.5$ plane in Figure 12. The neutral fraction slices prominently show the sharp shadows created by the clump and demonstrates the non-diffusivity behavior of ray tracing. The discretization of the sphere creates one neutral cell on the left side of the sphere. This inherent artifact to the initial setup carries through the calculation. We did not smooth the clump surface like in some of the RT06 codes, in order to remove this artifact. It is seen in the neutral fraction and temperature states at all times and is not a caused by our ray tracing algorithm.
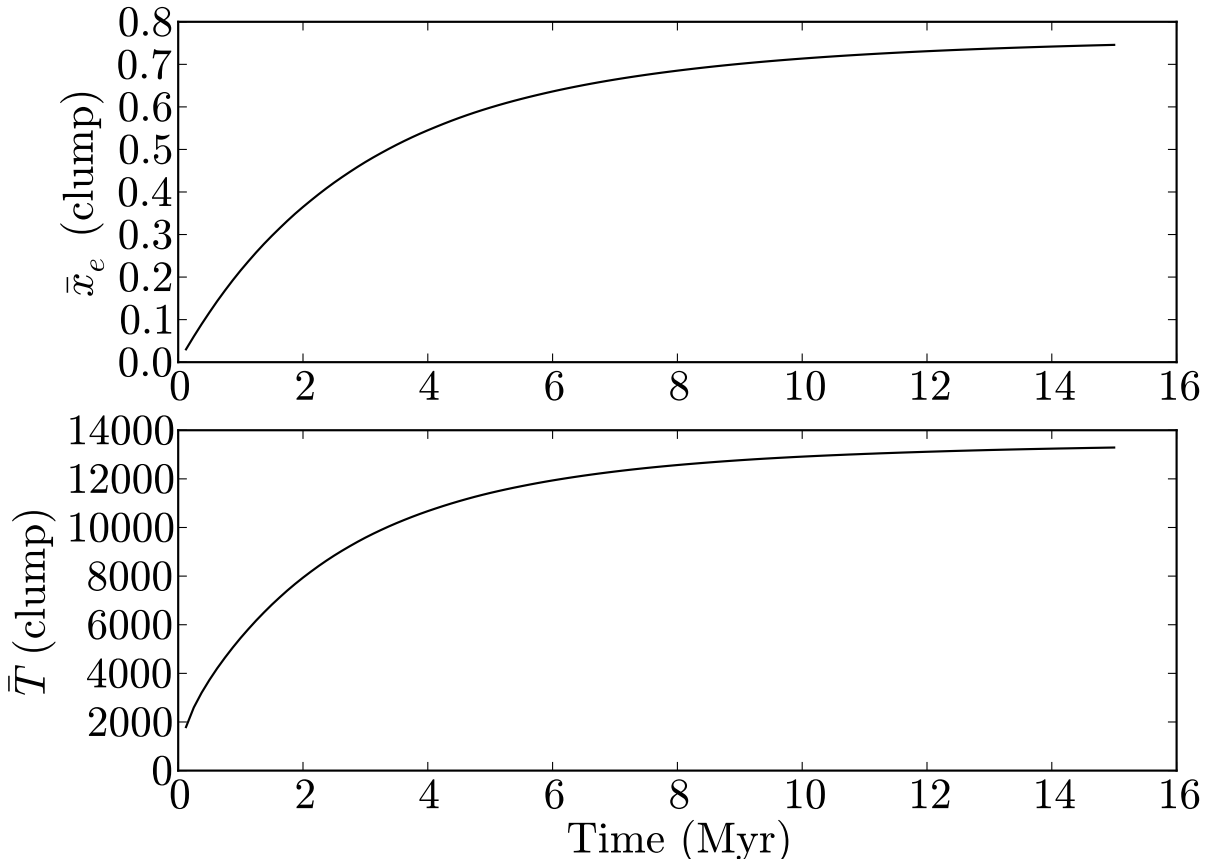
Fig. 11.— Test 3. (I-front trapping in a dense clump and shadowing). Evolution of the average ionized fraction (top) and temperature (bottom) of the overdense clump.

4.4. Test 4. Multiple sources in a cosmological density field

The last test in RT06 involves a static cosmological density field at $z = 9$. The simulation comoving box size is $0.5\ h^{-1}$ Mpc and has a resolution of 128^3. There are 16 point sources that are centered in the 16 most massive halos. They emit $f_\gamma = 250$ ionizing photons per baryon in a blackbody spectrum with an effective temperature $T = 10^5$ K, and they live for $t_s = 3$ Myr. Thus the luminosity of each source is

$$\dot{N}_\gamma = f_\gamma \frac{M\Omega_b}{\Omega_m m_H t_s}, \tag{35}$$

where M is the halo mass, $\Omega_m = 0.27$, and $\Omega_b = 0.043$. The radiation boundaries are isolated so that the radiation leaves the box instead being shifted periodically. The simulation is evolved for 0.4 Myr.
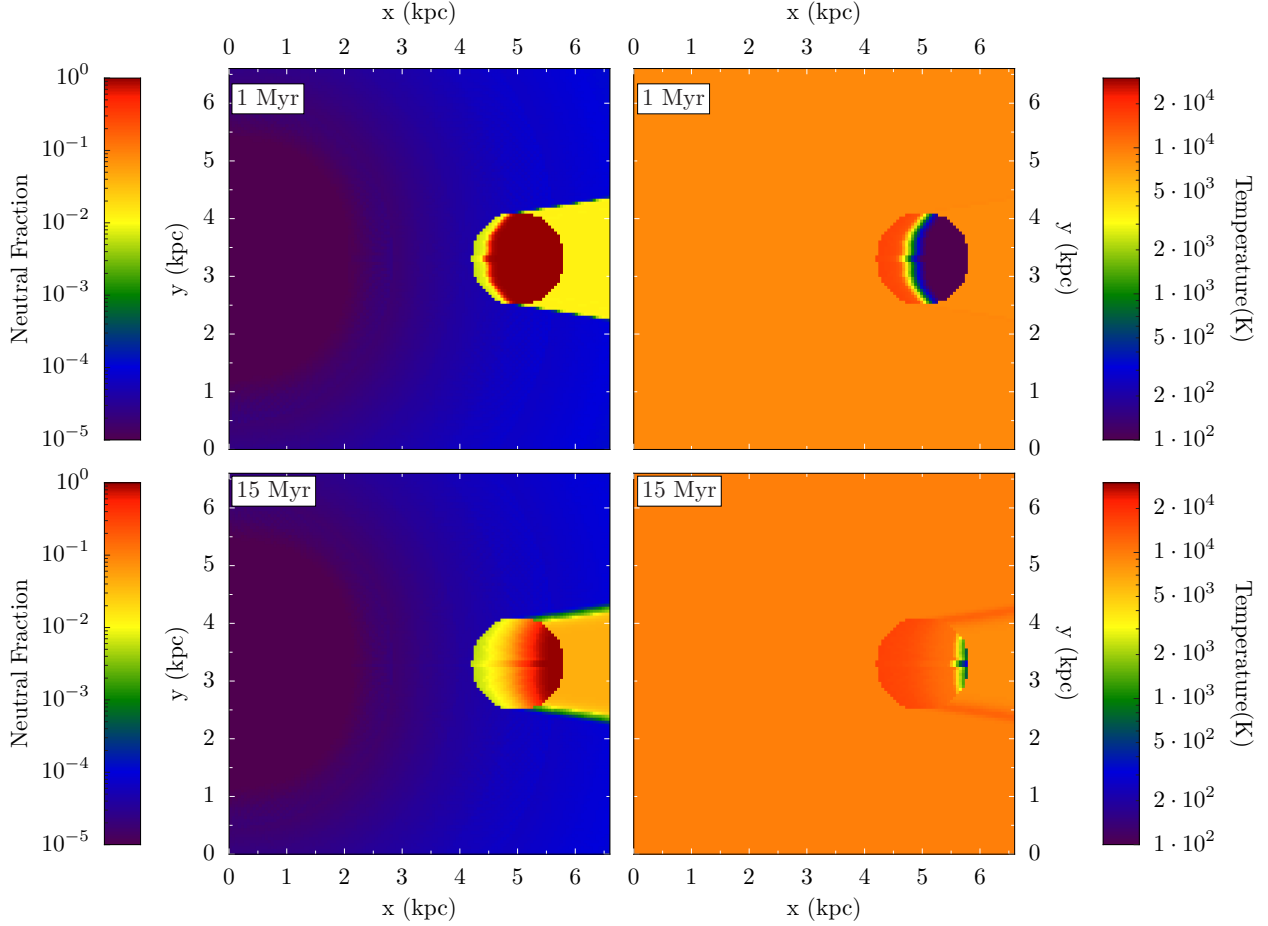
Fig. 12.— Test 3. (I-front trapping in a dense clump and shadowing). Clockwise from upper left: Slices through the origin of neutral fraction (1 Myr), temperature (1 Myr), temperature (15 Myr), and neutral fraction (15 Myr).

We show the growth of the H II regions by computing the mass-averaged x_m and volume-averaged x_v ionized fraction in Figure 13. Initially x_m is larger than x_v, and at $t \sim 170$ kyr, the x_v becomes larger. This is indicative of inside-out reionization (e.g. Gnedin 2000; Miralda-Escudé et al. 2000; Sokasian et al. 2003), where the dense regions around halos are ionized first, then the voids are ionized last. At the end of the simulation, $x_v = 0.65$, which is lower than all of the codes in RT06. However by visual inspection in the slices of electron fraction (Fig. 14), there appears to be very good agreement with C^2-ray and FTTE. By first glance, our result appears to be different than the RT06 because of the color-mapping. Our results are also in good agreement with the multi-frequency version of TRAPHIC (Pawlik & Schaye 2010, see also for better representations of the electron fraction slices). In the slices of electron fraction and temperature, Figure 14, the photo-heated regions are larger than
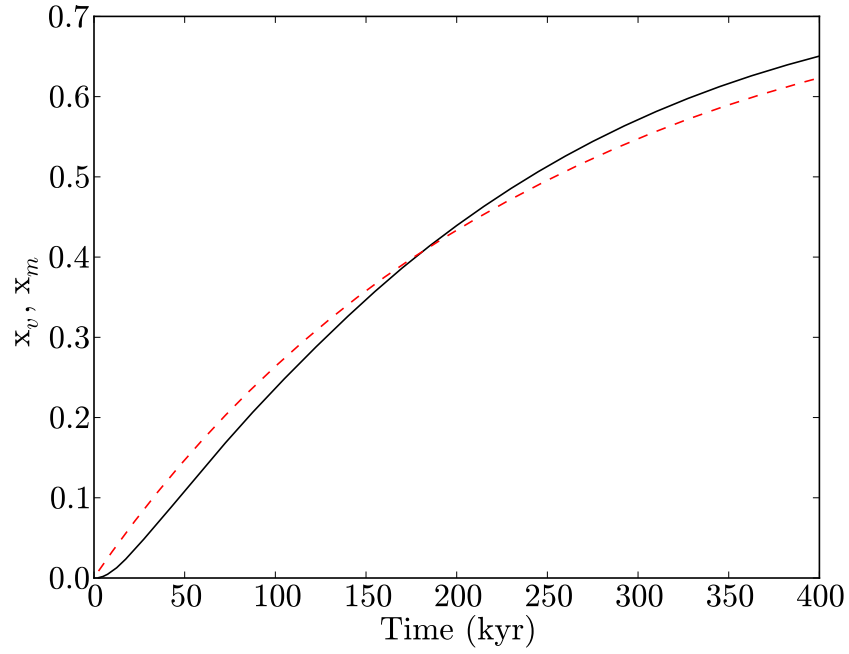
Fig. 13.— Test 4. (Multiple cosmological sources). Evolution of the mass- (dashed) and volume-averaged (solid) ionized fraction.

the ionized regions by a factor of 2–3 because of the hardness of the $T = 10^5$ K blackbody spectrum.
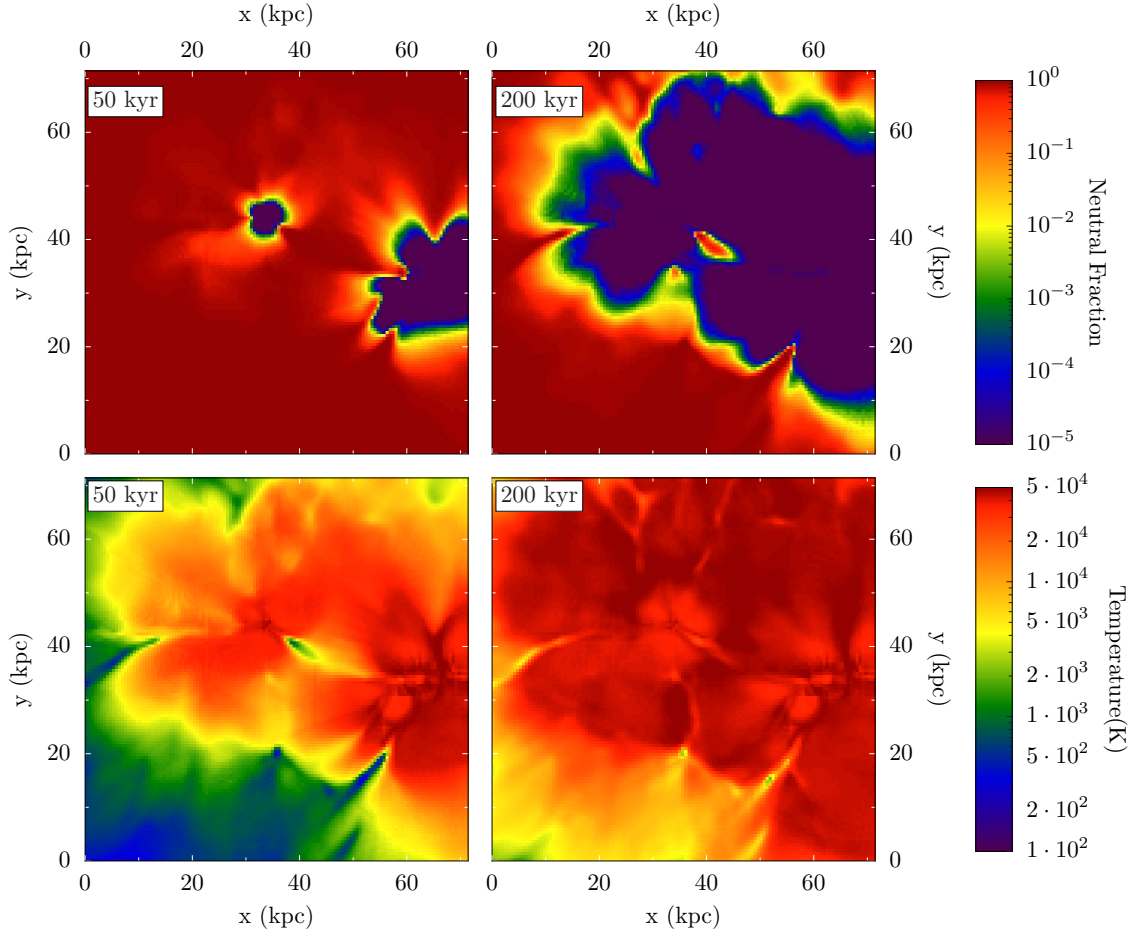
Fig. 14.— Test 4. (Multiple cosmological sources). Top: Slices through the origin of neutral fraction at 50 and 200 kyr at the coordinate $z = z_{\mathrm{box}}/2$. Bottom: Slices of temperature at 50 and 200 kyr. No smoothing has been applied to the images.

5. Radiation Hydrodynamics Tests

In this section, we show results from radiation hydrodynamics test problems presented in Iliev et al. (2009, hereafter RT09). They involve (1) the expansion of an H II region in a uniform medium, similar to Test 2, (2) an H II region in an isothermal sphere, and (3) the photo-evaporation of a dense, cold clump, similar to Test 3. We expand on this test suite to include more complex situations, such as a Rayleigh-Taylor problem illuminated by a radiation source, champagne flows, collimated radiation, an irradiated blast wave, and an H II region in a rotating sphere. For the Iliev et al. tests, we turn off self-gravity and AMR in accordance with them. In the latter tests, we will indicate whether we use those capabilities of *Enzo*. Lastly, we use the new MHD implementation in *Enzo* v2.0 in the problem of a
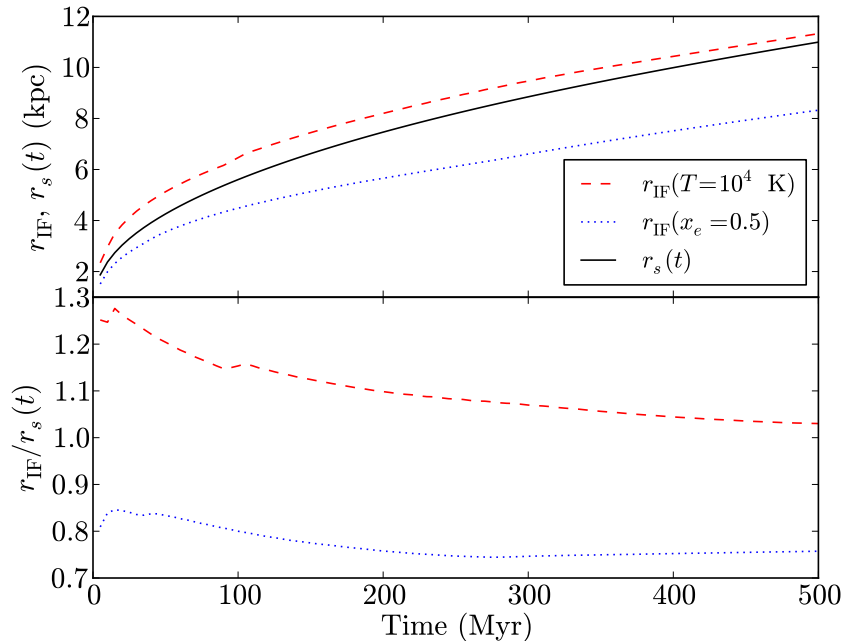
Fig. 15.— Test 5. (H II region in a uniform medium). Top: Growth of the computed ionization front radius at an ionized fraction $x_e = 0.5$ (dashed) and at a temperature $T = 10^4$ K (dotted) compared to the analytical estimate (solid; Eq. 36). Bottom: The ratio of the computed ionization front radii to the analytical estimate.

growing H II region in a magnetic field.

5.1. Test 5. Classical H II region expansion

Here we consider the expansion of an H II region into a uniform neutral medium including the hydrodynamical response to the heated gas. The ionized region has a greater pressure than the ambient medium, causing it to expand. This is a well-studied problem (Spitzer 1978) with an analytical solution, where the ionization front moves as

$$r_s(t) = r_{s,0} \left(1 + \frac{7c_s}{4R_s} \right)^{4/7}, \tag{36}$$

where c_s is the sound speed of the ionized gas and $r_{s,0}$ is the r_s in Equation 33. The bubble eventually reaches pressure equilibrium with the ambient medium at a radius

$$r_f = R_s \left(\frac{2T}{T_0} \right)^{2/3}, \tag{37}$$
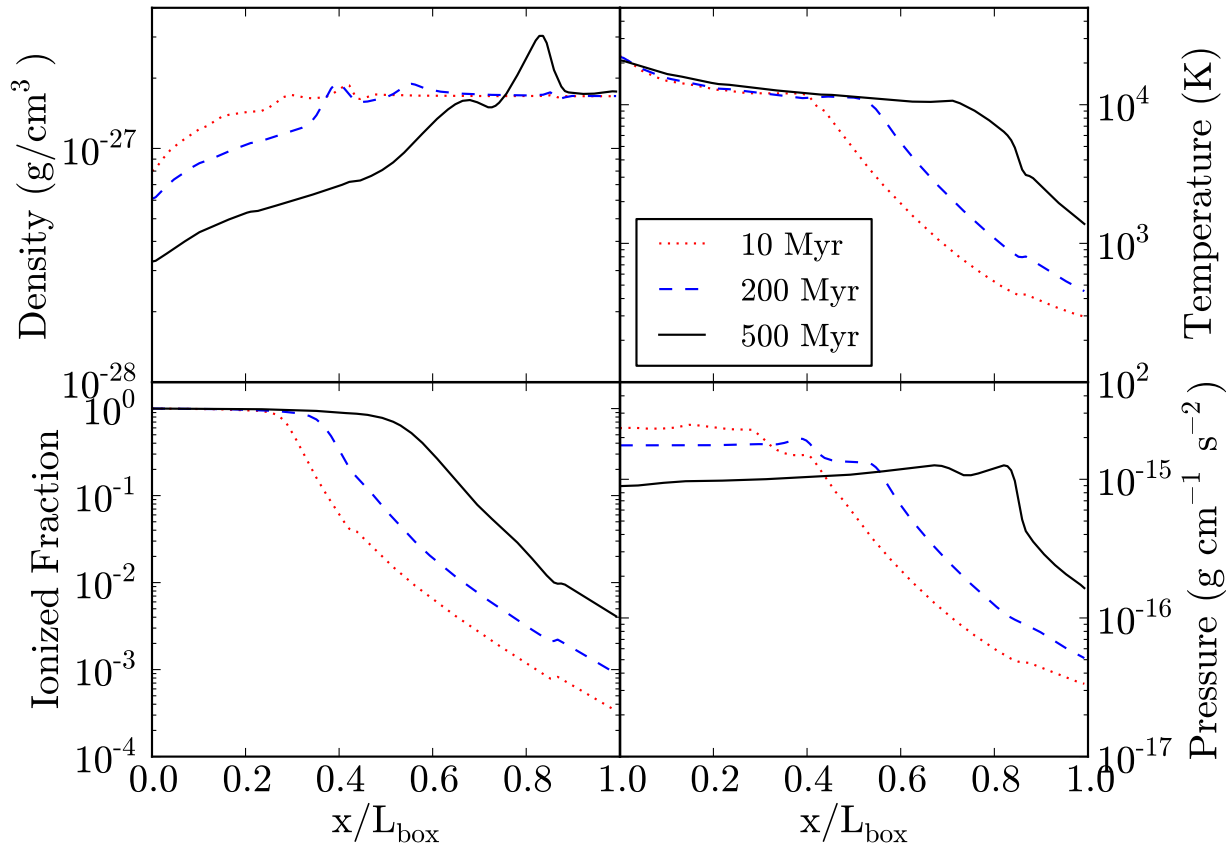
Fig. 16.— Test 5. (H II region in a uniform medium). Clockwise from the upper left: Radial profiles of density, temperature, ionized fraction, and pressure at times $t = 10$, 200, and 500 Myr.

where T and T_0 are the ionized and ambient temperatures, respectively. These solutions only describe the evolution at late times, and not the fast transition from R-type to D-type at early times.

The simulation setup is similar to Test 2 with the exception of the domain size $L = 15$ kpc. Here pressure equilibrium occurs at $r_f = 185$ kpc, which is not captured by this test. However more interestingly, the transition from R-type to D-type is captured and occurs around $R_s = 5.4$ kpc. The test is run for 500 Myr.

The growth of the H II region is shown in Figure 15, using both $T = 10^4$ K and $x_e = 0.5$ as ionization front definitions, compared to the analytical solution (Eq. 37). We define this alternative measure because the ionization front becomes broad as the D-type front creates a
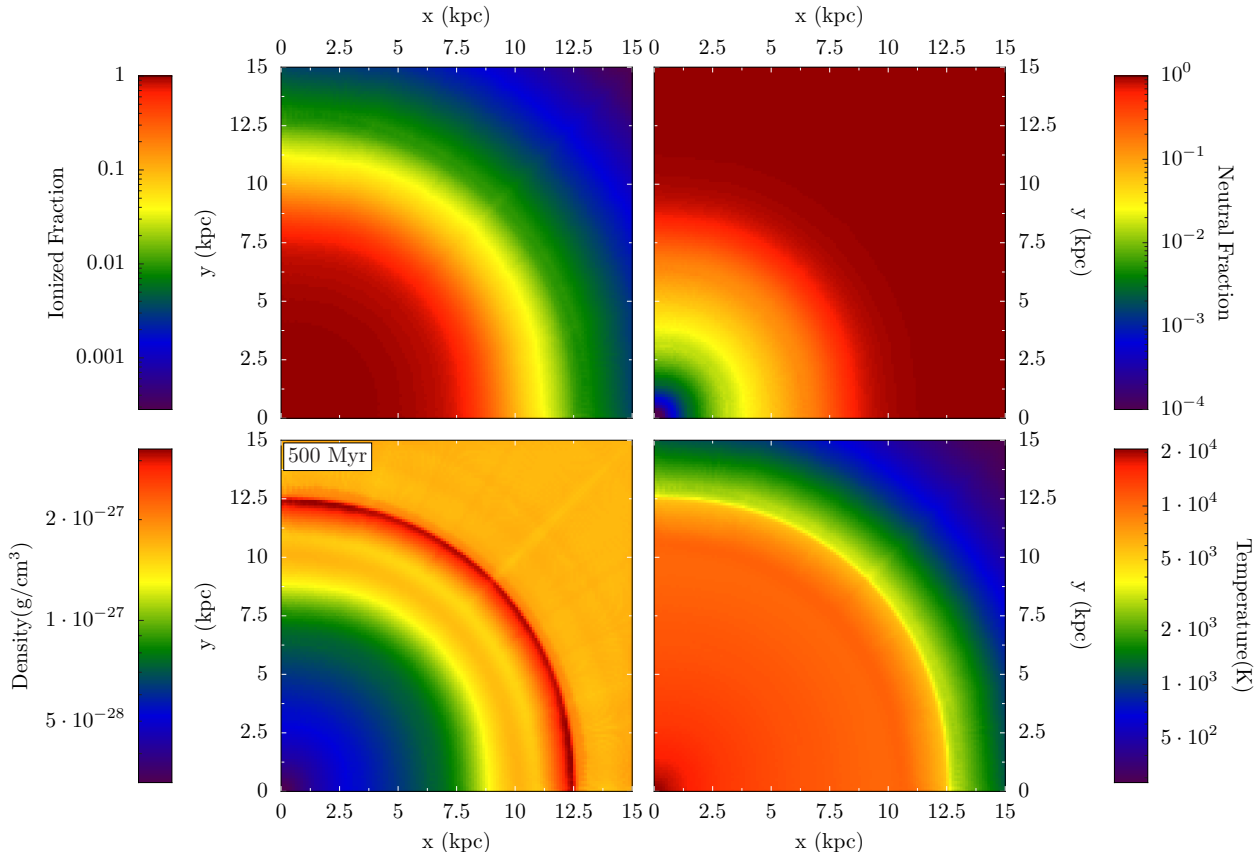
Fig. 17.— Test 5. (H II region in a uniform medium). Clockwise from the upper left: Slices through the origin of ionized fraction, neutral fraction, temperature, and density at time $t = 500$ Myr.

shock. Densities in this shock, as seen in Figure 16, are high enough for the gas to recombine but not radiatively cool. Before $2t_{rec} \approx 250$ Myr, the temperature cutoff overestimates r_s by over 10%; however at later times, it provides a good match to the $t^{4/7}$ growth at late times. With the $x_e = 0.5$ criterion for the ionization front, the radius is always underestimated by $\sim 20\%$. This behavior was also seen in RT09.

Figure 16 shows the progression of the ionization front at times $t = 10$, 200, and 500 Myr in radial profiles of density, temperature, pressure, and ionized fraction. The initial H II region is over-pressurized and creates an outward shock wave. The high-energy photons can penetrate through the shock and partially ionizes and heats the exterior gas, clearly seen in the profiles. As noted in RT09, this heated exterior gas creates an photo-evaporative flow that flows inward. This interacts with the primary shock and creates the double-peaked features in the density profiles at 200 and 500 Myr. Figure 17 shows slices through the origin of the
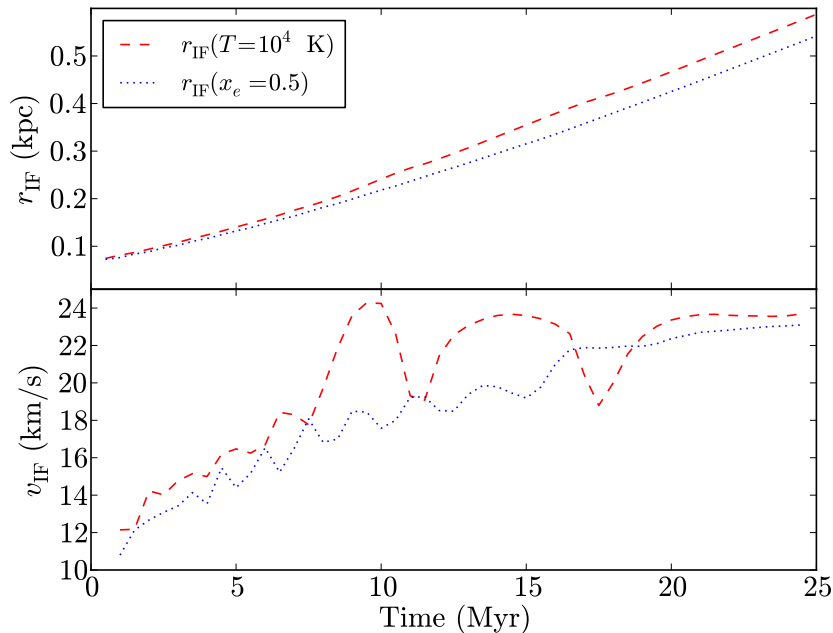
Fig. 18.— Test 6. (H II region in a $1/r^2$ density profile). Top: Growth of the computed ionization front radius as $T = 10^4$ K and $x_e = 0.5$ as definitions for the front. Bottom: Velocity of the ionization front, computed from outputs at 0.5 Myr intervals. The velocity is calculated from r_{IF}, whose coarse time resolution causes the noise seen in v_{IF}. It is smooth within the calculation itself.

same quantities, including neutral fraction. These depict the very good spherical symmetry of our method. The only apparent artifact is a very slight diagonal line, which is caused by the HEALPix pixelization differences between the polar and equatorial regions. This artifact diminishes as the ray-to-cell sampling is increased.

5.2. Test 6. H II region expansion in an isothermal sphere

A more physically motivated scenario is an isothermal sphere with a constant density n_c core, which is applicable to collapsing molecular clouds and cosmological halos. The radial density profile is described by

$$n(r) = \begin{cases} n_c & (r \leq r_0) \\ n_c(r/r_0)^{-2} & (r > r_0) \end{cases} , \tag{38}$$
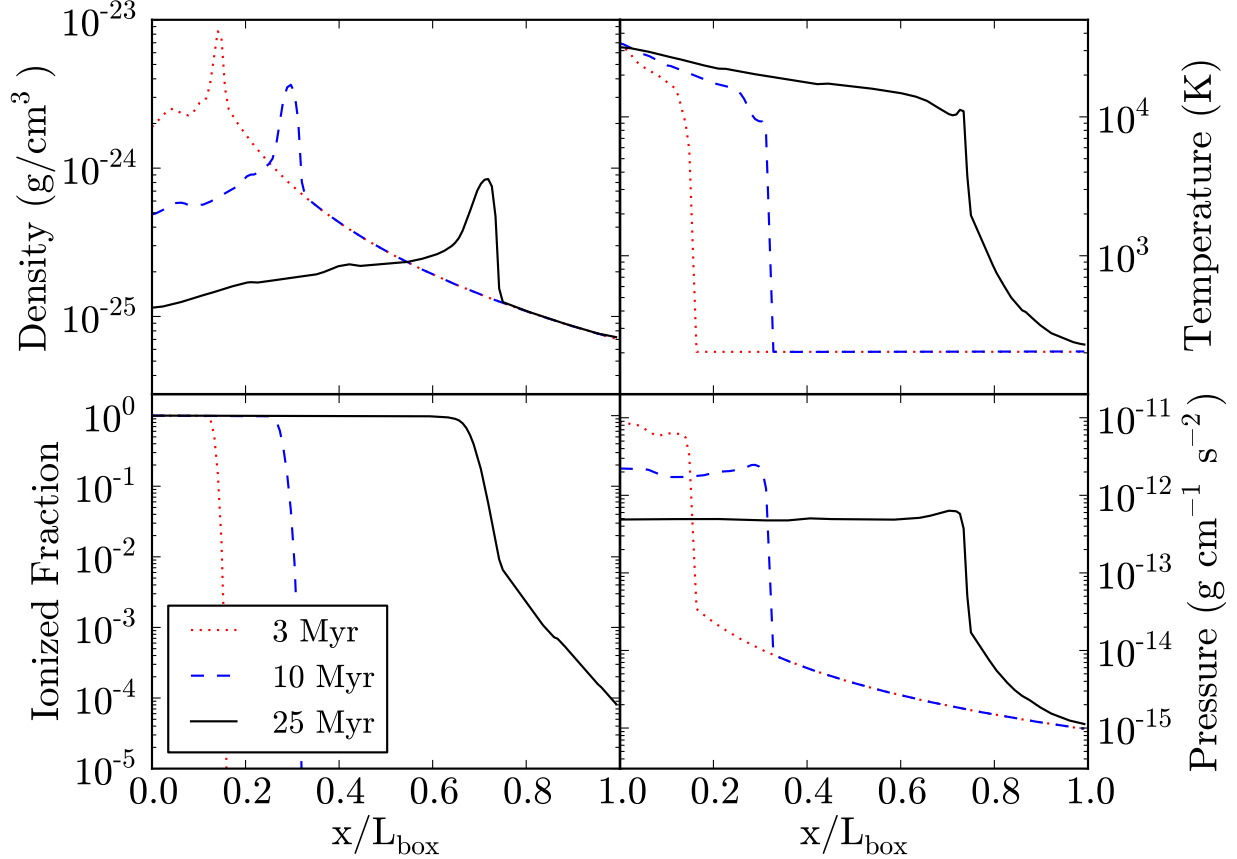
Fig. 19.— Test 6. (H II region in a $1/r^2$ density profile). Clockwise from the upper left: Radial profiles of density, temperature, ionized fraction, and pressure at times $t = 3$, 10, and 25 Myr.

where r_0 is the radius of the core. If the Strömgren radius is smaller than the core radius, then the resulting H II region never escapes into the steep density slope. When the ionization front propagates out of the core, it accelerates as it travels down the density gradient. There exists no analytical solution for this problem with full gas dynamics but was extensively studied by Franco et al. (1990). After the gas is ionized and photo-heated, the density gradient provides the pressure imbalance to drive the gas outwards.

This test is constructed to study the transition from R-type to D-type in the core and back to R-type in the density gradient. Thus the simulation focuses on small-scale, not long term, behavior of the ionization front. The simulation box has a side length $L = 0.8$ kpc with core density $n_0 = 3.2$ cm^{-3}, core radius $r_0 = 91.5$ pc (15 cells), and temperature $T = 100$ K
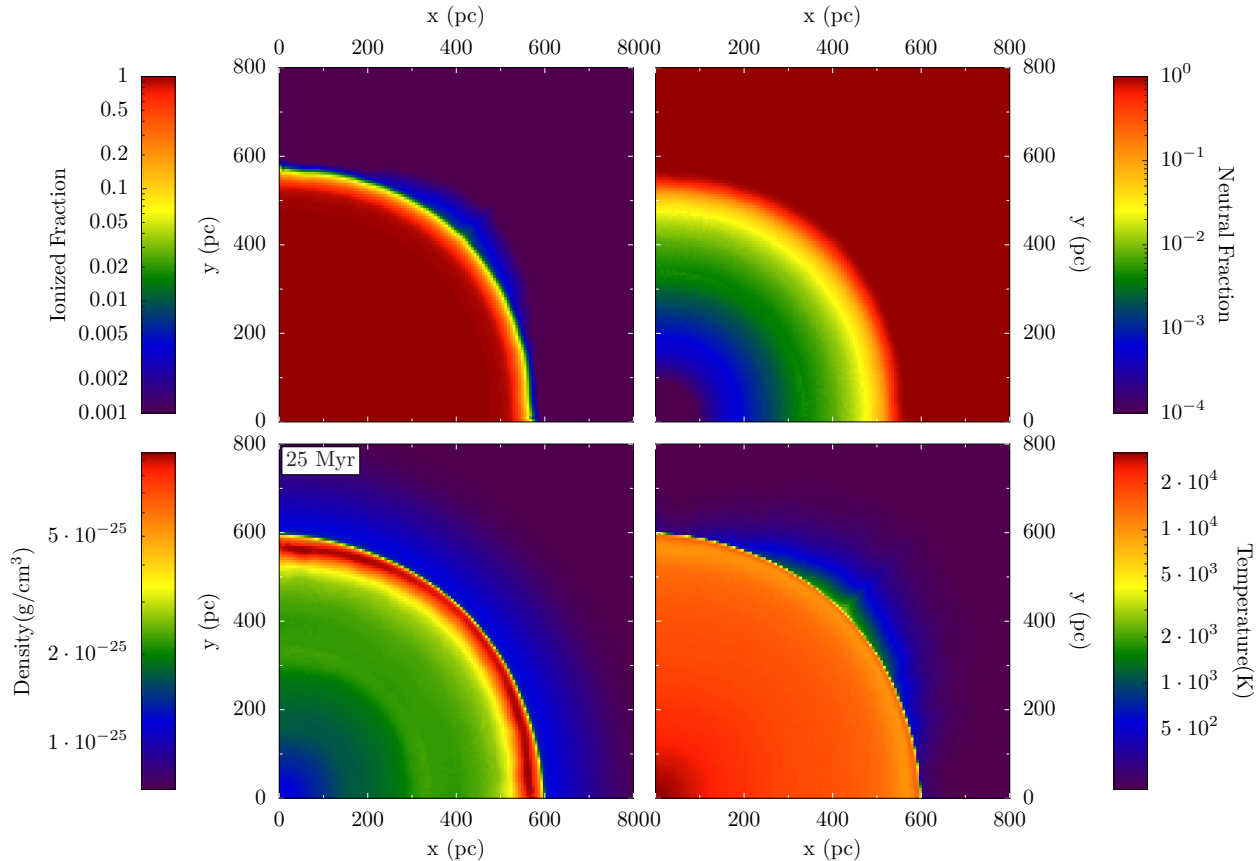
Fig. 20.— Test 6. (H II region in a $1/r^2$ density profile). Clockwise from the upper left: Slices through the origin of ionized fraction, neutral fraction, temperature, and density at time $t = 25$ Myr.

throughout the box. The ionization fraction is initially zero, and the point source is located at the origin with a luminosity of 10^{50} ph s^{-1} cm^{-3}. The simulation is run for 75 Myr.

Because this problem does not have an analytical solution, we compare our calculated ionization front radius and velocity, shown in Figure 18, to the RT09 results. Their evolution are in agreement within 5% of RT09. As in Test 5, we use an extra definition of $T = 10^4$ K for the ionization front. We compute the ionization front velocity from the radii at 50 outputs, which causes the noise seen Figure 18.

For the first Myr, the radiation source creates a weak R-type front where the medium is heated and ionized but does not expand because $v_{IF} > c_s$. When v_{IF} becomes subsonic, the medium can react to the passing ionization front and creates a shock, leaving behind a heated an rarefied medium. This behavior is clearly seen in the radial profiles of density, temperature, ionized fraction, and pressure in Figure 19. The inner density decreases over

two order of magnitude after 25 Myr. To illustrate any deviations in spherical symmetry, we show in Figure 20 slices of density, temperature, neutral fraction, and ionized fraction at the final time. The only artifact apparent to us is the slight broadening of the shock near the $x = 0$ and $y = 0$ planes. This causes the ionization front radius to be slightly smaller in those directions. In the diagonal direction, the neutral column density through the shock is slightly smaller, allowing the high-energy photons to photoionize and photoheat the gas to $x_e = 5 \times 10^{-3}$ and $T = 2000$ K out to ~ 50 pc from the shock. The reflecting boundaries in Enzo might be responsible for this artifact because this is not seen when the problem is centered in the domain, removing any boundary effects.

5.3. Test 7. Photo-evaporation of a dense clump

The photo-evaporation of a dense clump in a uniform medium proceeds very differently when radiation hydrodynamics is considered instead of a static density field. The ionization front first proceeds as a very fast R-type front, then it slows to a D-type front when it encounters the dense clump. As the clump is gradually photoionized and heated, it expands into the ambient medium. The test presented here is exactly like Test 3 but with gas dynamics. In this setup, the ionization front overtakes the entire clump, which is then completely photo-evaporated.

Figure 21 shows cuts of density, temperature, neutral fraction, and pressure in a line connecting the source and the clump center at $t = 1$, 10, and 50 Myr. At 1 Myr, the ionization front has propagated through the left-most 500 pc of the clump. This heated gas is now over-pressurized, as seen in the pressure plot in Figure 21, and then expands into the ambient medium. This expansion creates a photo-evaporative flow, seen in many star forming regions (e.g. M16 Hester et al. 1996) as stars irradiate nearby cold, dense overdensities. These flows become evident in the density at 10 Myr, seen both in the line cuts and slices (Figure 22). These outflows have temperatures up to 50,000 K. At this time, the front has progressed about halfway through the clump, if one inspects the neutral fraction. However the high energy photons have heated all but the rear surface of the clump. At the end of the test ($t = 50$ Myr), only the core and its associated shadow is neutral, as seen in Figure 23. The core has been compressed by the surrounding warm medium, thus causing the higher densities seen at $t = 50$ Myr. The non-spherical artifacts on the inner boundary of the warm outermost shell are caused by the initial discretization of the sphere, as discussed in §4.3.
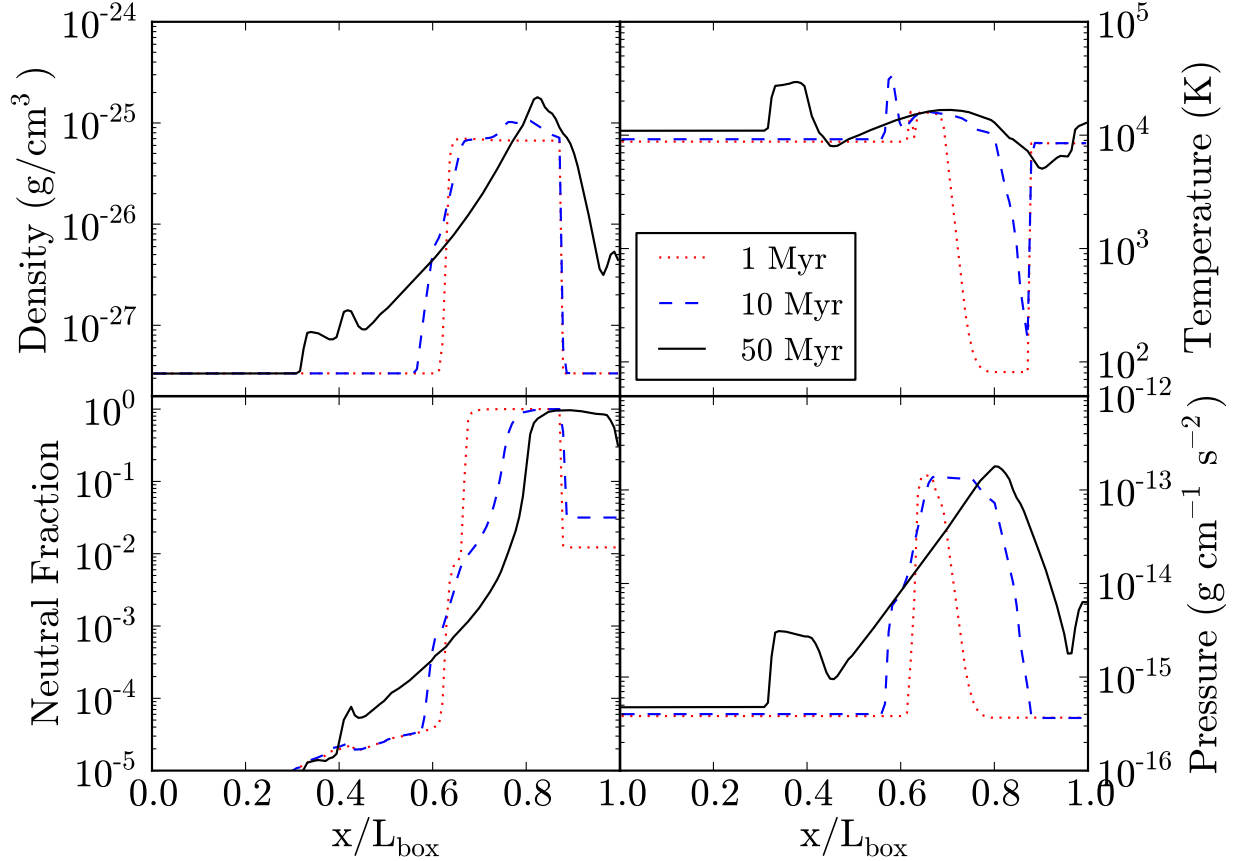
Fig. 21.— Test 7. (Photo-evaporation of a dense clump). Line cuts from the point source through the middle of the dense clump at $t = 1, 10, 50$ Myr of (clockwise from the upper left) density, temperature, pressure, and neutral fraction.

5.4.   Test 8. Champagne flow from a dense clump

Radiation-driven outflows from overdensities, known as champagne flows, is a long studied problem (e.g. Yorke 1986, §3.3). We set up a spherical tophat with an overdensity of 10 and radius of 1 pc in a simulation box of 8 pc. The ambient medium is 290 cm^{-3} and 100 K. The radiation source is offset from the overdensity center by 0.4 pc. It has a luminosity of 10^{49} ph s^{-1} and a $T = 10^5$ K blackbody spectrum. The resulting Strömgren radius is 0.33 pc, just inside of the overdense clump. These parameters are the same used in Bisbas et al. (2009). The entire domain initially has an ionized fraction of 10^{-6}. We do not consider self-gravity. The simulation has a resolution of 128^3 on base grid, and we refine the grid up to 4 times if a cell has an overdensity of 1.5×2^l, where l is the AMR level. The simulation
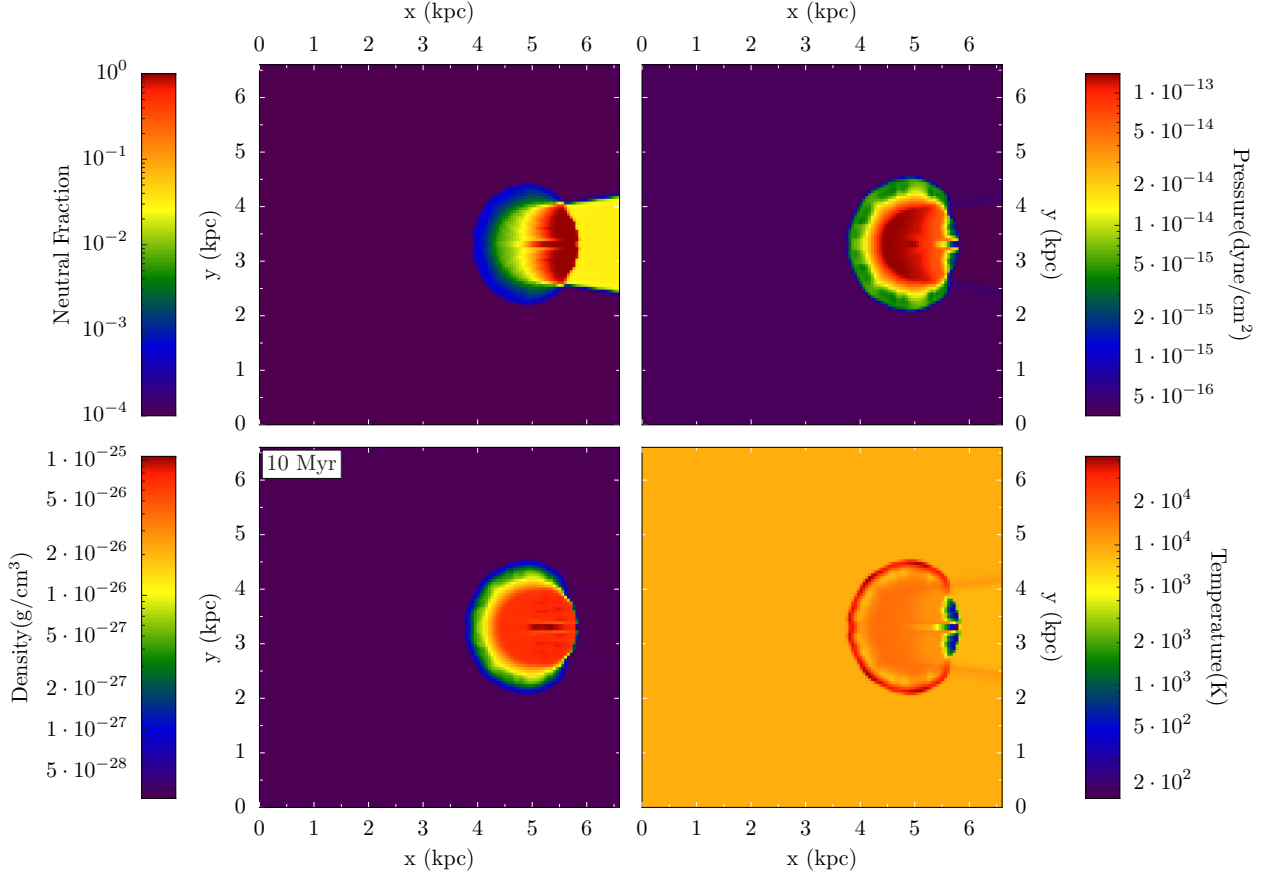
Fig. 22.— Test 7. (Photo-evaporation of a dense clump). Clockwise from the upper left: Slices through the clump center of neutral fraction, pressure, temperature, and density at time $t = 10$ Myr.

is run for 150 kyr.

We show slices in the x-y and x-z planes of density in Figure 24 at $t = 10, 40, 100, 150$ kyr. In the direction of the clump center, the ionization front transitions from spherical to parabolic after it escapes from the clump in the opposite direction. At $t = 10$ kyr, the surface of the H II region is just contained within the overdensity. In the x-z plane, there are density perturbations only above a latitude of 45 degrees. We believe that these are caused by the mismatch between HEALPix pixels and the Cartesian grid, even with our geometric correction. After the ionization front escapes from the clump in the negative x-direction, these perturbations grow from Rayleigh-Taylor instabilities as the gas is accelerated when it exits the clump. As the shock propagates through the ambient medium, it is no longer accelerated and has a nearly constant velocity, as seen in Test 6. Thus these perturbations are not as vulnerable to Rayleigh-Taylor instabilities at this point. The ambient medium
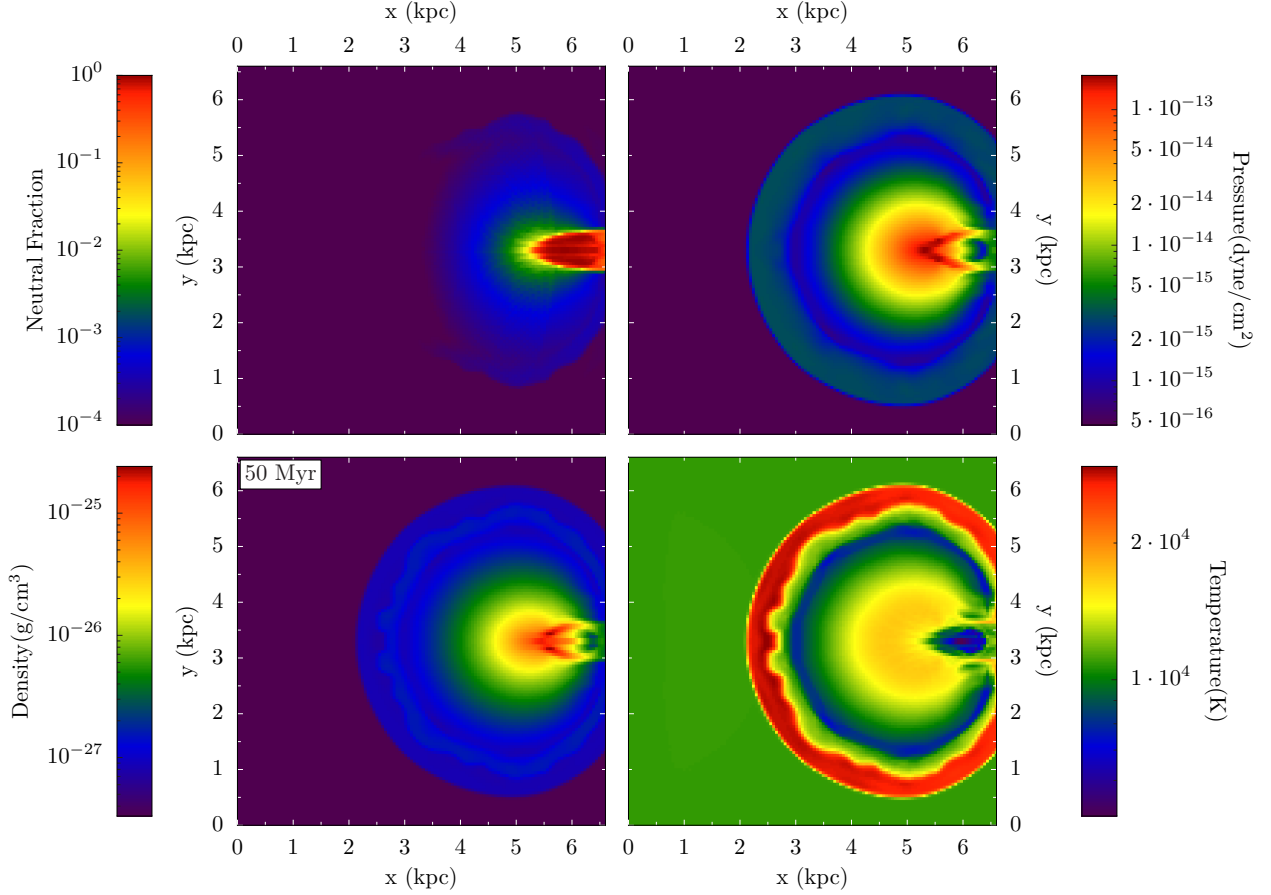
Fig. 23.— Test 7. (Photo-evaporation of a dense clump). Same as Figure 21 but at $t = 50$ Myr.

and shock are always optically thick, even in the directions of the bubbles. Bisbas et al. found that the shock fragmented and formed globules; however we find the density shell is stable against such fragmentation. To investigate this scenario further, our next tests involve radiation driven Rayleigh-Taylor instabilities.

5.5. Test 9. Irradiated Rayleigh-Taylor instability

Here we combine the classic case of a Rayleigh-Taylor instability and an expanding H II region. The Rayleigh-Taylor instability occurs when a dense fluid is being supported by a lighter fluid, initially in hydrostatic equilibrium, in the presence of a constant acceleration field. This classic test alone evaluates how subsonic perturbations evolve. We consider the case of a single-mode perturbation. We let the system evolve without any radiation until
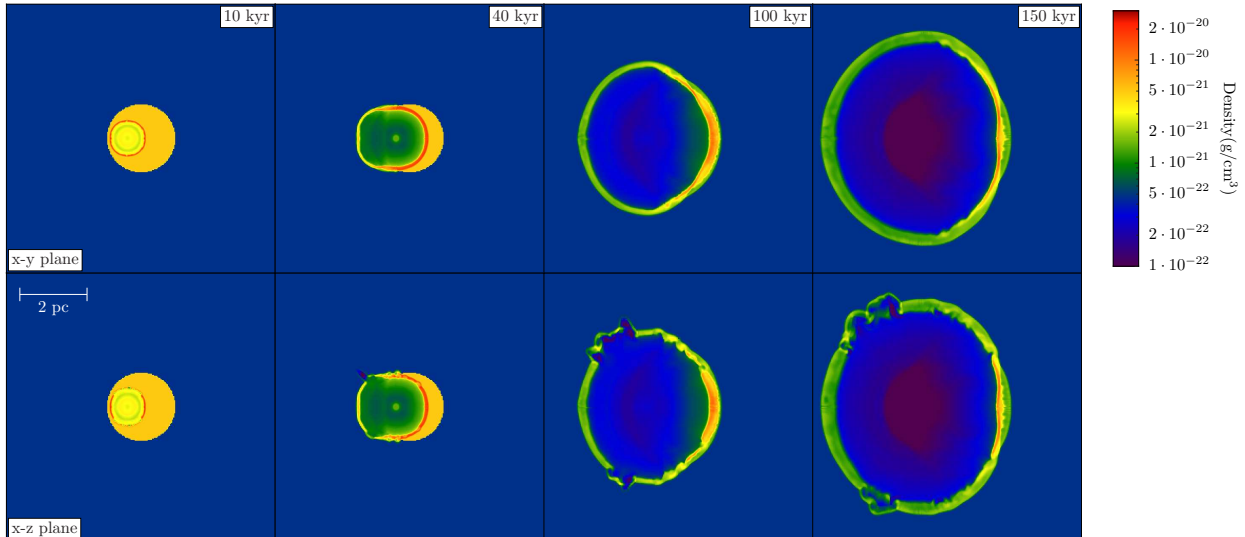
Fig. 24.— Test 8. (Champagne flow from a dense clump). Slices of density through the initial clump center in the x-y plane (top) and x-z plane (bottom) at $t = 10, 40, 100, 150$ kyr. Notice the instabilities that grow from perturbations created while the H II region is contained in the dense clump.

the perturbation grows considerably and then turn on the radiation source. These tests demonstrate that Enzo+Moray can follow a highly dynamic system and resolve fine density structures.

We run two cases — an optically-thick and optically-thin case. In the former, we take the parameter choices from past literature (e.g. Liska & Wendroff 2003; Stone et al. 2008) by setting the top and bottom halves of the domain to a density $\rho_1 = 2$ and $\rho_0 = 1$, respectively. The velocity perturbation is set in the z-direction by

$$v_z(x, y, z) = 0.01[1 + \cos(2\pi x/L_x)] \times [1 + \cos(2\pi y/L_y)] \times [1 + \cos(2\pi z/L_z)]/8. \qquad (39)$$

We set the acceleration field $g_z = 0.1$ and the adiabatic index $\gamma = 1.4$. We use a domain size of $(L_x, L_y, L_z) = (0.5, 0.5, 1.5)$ with a resolution of $(64, 64, 192)$. For hydrostatic equilibrium, we set $P = P_0 - g\rho(z)z$ with $P_0 = 2.5$. In order to consider a radiation source with a ionizing photon luminosity of 10^{42} ph s^{-1}, we scale the domain to a physical size of $(0.5, 0.5, 1.5)$ pc; time is in units of Myr; density is in units of m_h, resulting in an initial temperature of $(T_0, T_1) = (363, 726)$ K. The radiation source starts to shine at $t = 10$ Myr.

The optically-thin case is set up similarly but with three changes—(1) a density contrast of 10, (2) a luminosity of 10^{43} ph s^{-1}, and (3) the source is born at 6.5 Myr. The time units
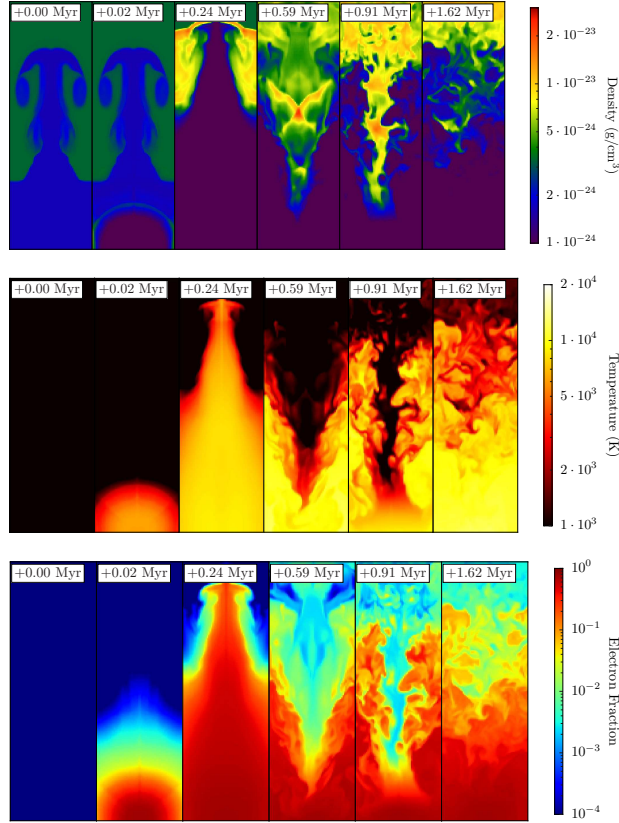
Fig. 25.— Test 9. (Irradiated Rayleigh-Taylor instability; optically thick case). Slices at $y = 0$ of density (top), temperature (middle), and electron fraction (bottom). The source turns on at $t = 0$.

are decreased to 200 kyr so that $(T_0, T_1) = (1.8 \times 10^3, 1.8 \times 10^4)$ K. Note that in code units, pressure is unchanged. We adjust the physical unit scaling, so the light fluid has $T > 10^4$ K, $x_e \sim 1$, and thus optically-thin. Furthermore, the ionization front remains R-type before interacting with the instability. A possible physical analogue could be a radiation source heating and rarefying the medium below.

The x and y-boundaries are periodic, and the z-boundaries are reflecting. The radiation source is placed at the center of lower z-boundary face. The periodic boundaries will cause features that are non-physical, considering a more realistic plane-parallel case. Nevertheless, these tests provide a good check on a radiation hydrodynamics solver. We show the evolution of the density, temperature, and ionized fraction of the optically thick and optically thin cases in Figures 25 and 26. The initial state of the Rayleigh-Taylor instability is shown in the left panels.
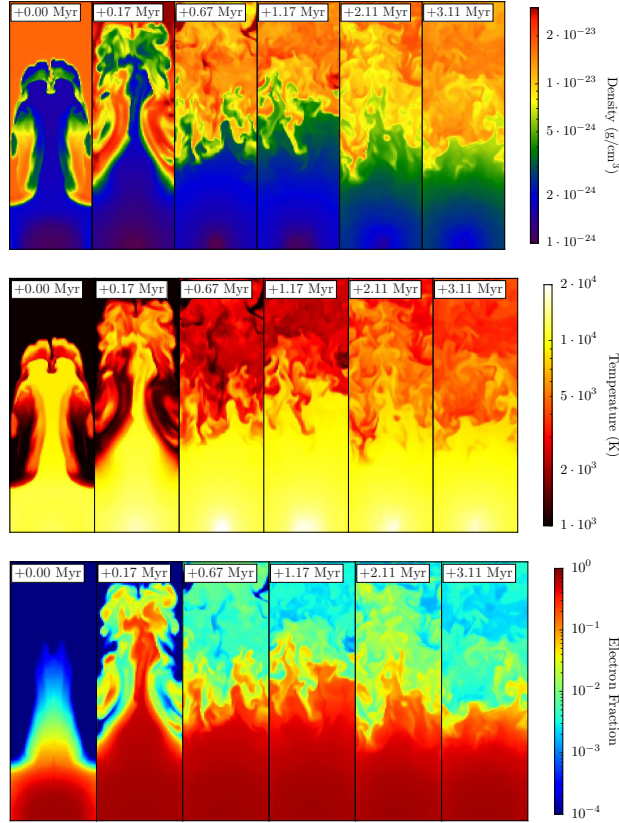
Fig. 26.— Same as Figure 25 but for the optically thin case.

In the optically thick case, a D-type front is created, which is clearly illustrated by the spherical density enhancement at 0.02 Myr. The shock then passes through the instability at $\sim$0.25 Myr and reflects off the upper z-boundary. This and complex shock reflections create a Richtmeyer-Meshkov instability, driving a chaotic jet-like structure downwards. The radiation source photo-evaporates the outer parts of this structure. The interaction between the dense cool "jet" and the hot medium further drives instabilities along the surface, which can be seen when comparing $t = 0.59$ Myr and $t = 0.91$ Myr slices. At the latter time, the jet cannot reach the bottom of the domain before being photo-evaporated. Eventually this structure is completely destroyed, leaving behind a turbulent medium between the hot and cold regions.

The optically thin problem is less violent than the optically thick case because the R-type front does not interact with the initial instability as strongly. The radiation source provides further buoyancy in the already $T = 10^4$ K gas. The gas first to be ionized and photo-evaporates is the outer regions of the instability. The enhanced heating also drives
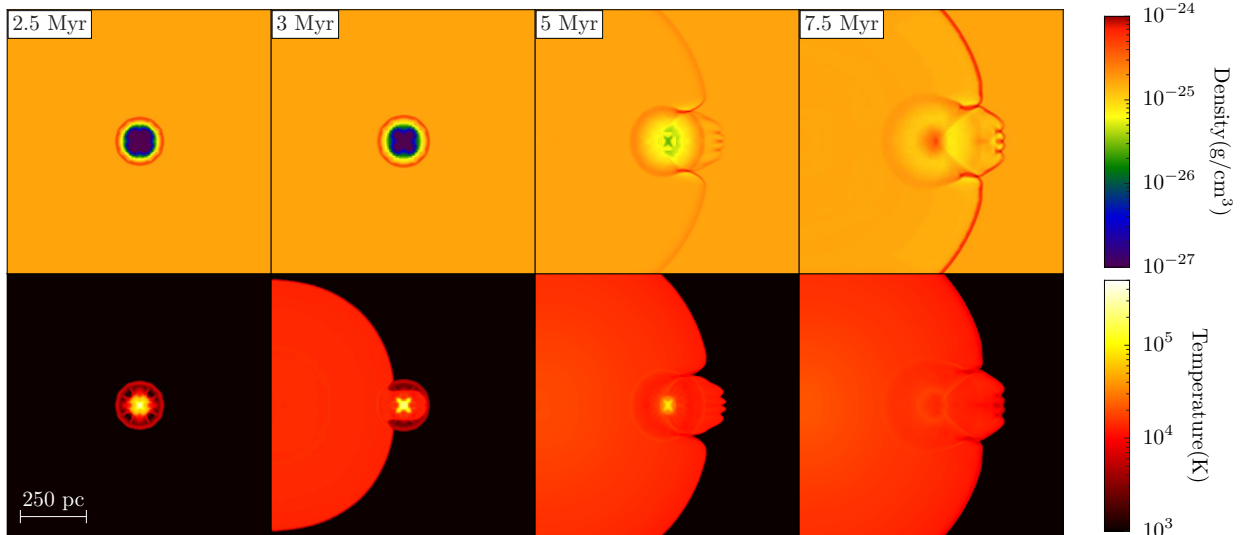
Fig. 27.— Test 10 (Photo-evaporation of a blastwave). Slices of density (top) and temperature (bottom) at $t = 2.5, 3, 5, 7.5$ Myr in the $x - z$ plane. As the R-type ionization front propagates through the blastwave center, instabilities grow from the slightly inhomogeneous hot and rarefied medium. Note that the dense shell of the blastwave also creates dense inward fingers in the ionization front shock.

the upper regions of the instability, making the top interface turbulent. It then reflects off the upper z-boundary and creates a warm $T = 5 \times 10^3$ K, partially ionized $(x_e \sim 10^{-2})$, turbulent medium, seen in the slices $t \geq 0.67$ Myr. The slices of electron fraction also show that the dense gas is optically thick.

5.6. Test 10. Photo-evaporation of a blastwave

A supernova blastwave being irradiated by a nearby star is a likely occurrence in massive-star forming regions. In this test, we set up an idealized test that mimics this scenario. The ambient medium has a density $\rho_0 = 0.1$ cm^{-3} and temperature $T_0 = 10$ K. The domain size is 1 kpc. We use 2 levels of AMR with a base grid of 64^3 that is refined if the density or total energy slope is greater than 0.4. The blastwave is initialized at the beginning of the Sedov-Taylor phase when the mass of the swept-up material equals the ejected material. It has a radius of 21.5 pc, a total energy of 10^{50} erg, and total mass of $100 M_\odot$, corresponding to $E = 315$ eV per particle or $E/k_b = 3.66 \times 10^6$ K. The radiation source is located at the center of the left x-boundary and has a luminosity of 10^{50} erg s^{-1}. We use a $T = 10^5$ K

blackbody spectrum with 2 energy groups (16.0 and 22.8 eV). The source turns on at 2.5 Myr at which point the blastwave has a radius of 200 pc. The simulation is run for 7.5 Myr.

Figure 27 shows the ionization front overtaking and disrupting the blastwave. We show the blastwave before the source is born at 2.5 Myr. The interior is rarefied ($\rho \sim 10^{-3}$ cm^{-3}). It is heated to $T \sim 5 \times 10^5$ K by the reverse shock. At $t = 3$ Myr, the ionization front is still R-type, and it ionizes the blastwave's dense shell. Because the interior is ionized and diffuse, the ionization front rapidly propagates through it until it reaches the opposite shell surface. Shortly afterward, the ionization front transitions from R-type to D-type at a radius of 0.5 kpc, seen in the formation of a shock in the 5 Myr density panel. This transition occurs by the construction of the problem not by the interaction with the blastwave. The surfaces of the blastwave that are perpendicular to the ionization front have the highest column density and thus are last to be fully ionized. The pressure forces from warm ambient medium and blastwave interior compress these surfaces, photo-evaporating them in the process, similar to Test 7. They survive until the final time $t = 7.5$ Myr. As the R-type ionization front interacts with the blastwave interior, the density perturbations create ionization front instabilities (**?**) that are seen on the H II region surface at the coordinate $z = 0.5$. Behind the ionization front, the dense shell of the blastwave is photo-evaporated, and a smooth overdensity is left in the initial blastwave center.

5.7.   Test 11. Collimated radiation from a dense clump

Some astrophysical systems produce collimated radiation either intrinsically by relativistic beaming or by an optically-thick torus absorbing radiation in the equatorial plane. The latter case would be applicable in a subgrid model of active galactic nuclei (AGN) or protostars, for example. Simulating collimated radiation with ray tracing is trivially accomplished by only initializing rays that are within some opening angle θ_c.

We use a domain that is 2 kpc wide and has an ambient medium with $\rho_0 = 10^{-3}$ cm^{-3}, $T = 10^4$ K, $x_e = 0.99$. We place a dense clump with $\rho/\rho_0 = 100$, $T = 100$ K, $x_e = 10^{-3}$, and $r = 250$ pc, at the center of the box. Radiation is emitted in two polar cones with $\theta_c = \pi/6$ with a total luminosity of 10^{49} erg s^{-1} and a 17.6 eV mono-chromatic spectrum. This results in $t_{\rm rec} = 1.22$ Myr and $R_s = 315$ pc, just outside of the sphere. The base grid has a resolution of 64^3, and it is refined with the same overdensity criterion as Test 8. We run this test for 25 Myr.

We illustrate the expansion of the H II region created by the beamed radiation in Figure 28. Before $t = 3$ Myr, the H II region is conical and contained within the dense
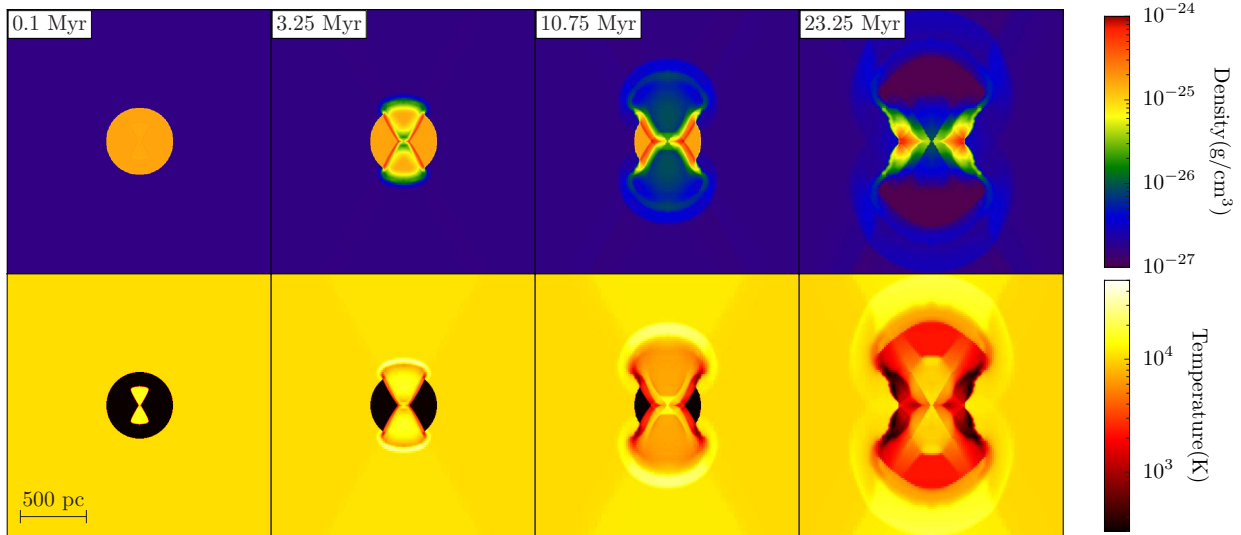
Fig. 28.— Test 11 (Collimated radiation from a dense clump). Slices of density (top) and temperature (bottom) at $t = 0.1, 3.25, 10.75, 23.25$ Myr. The conical H II region drives shocks transversely into the overdense sphere and creates polar champagne flows. The ambient medium is heated to $T \sim 3 \times 10^4$ K as the ionization front passes the constant-pressure cloud surface. The ionization front changes from D-type to R-type after it enters the ambient medium.

clump, depicted in the $t = 0.1$ Myr snapshot of the system. At this time, the ionization front is transitioning from R-type to D-type in the transverse direction of the cone. This can be seen in the minute overdensities on the H II transverse surface. When it breaks out of the overdensity, it creates a champagne flow, where the ionization front transitions back to a weak R-type front. The cloud surface is a constant-pressure contact discontinuity (CD) with a density jump of 100. After the front heats the gas at the CD, there exists a pressure difference of ~ 100. In response, the high density gas accelerates into the ambient medium and heats it to 3×10^4 K. Additionally a rarefaction wave travels towards the clump center. At later times, the transverse D-type front continues through the clump, eventually creating a disk-like structure at the final time. The polar champagne flows proceed to flow outwards, creating a density shell with a diffuse (10^{-28} cm^{-3}) and warm (5000 K) medium in its wake.

5.8. Test 12. Time variations of the source luminosity

Our implementation retains the time derivative of the radiative transfer equation (Eq. 2) if we choose a constant ray tracing timestep, which saves the photon packages between
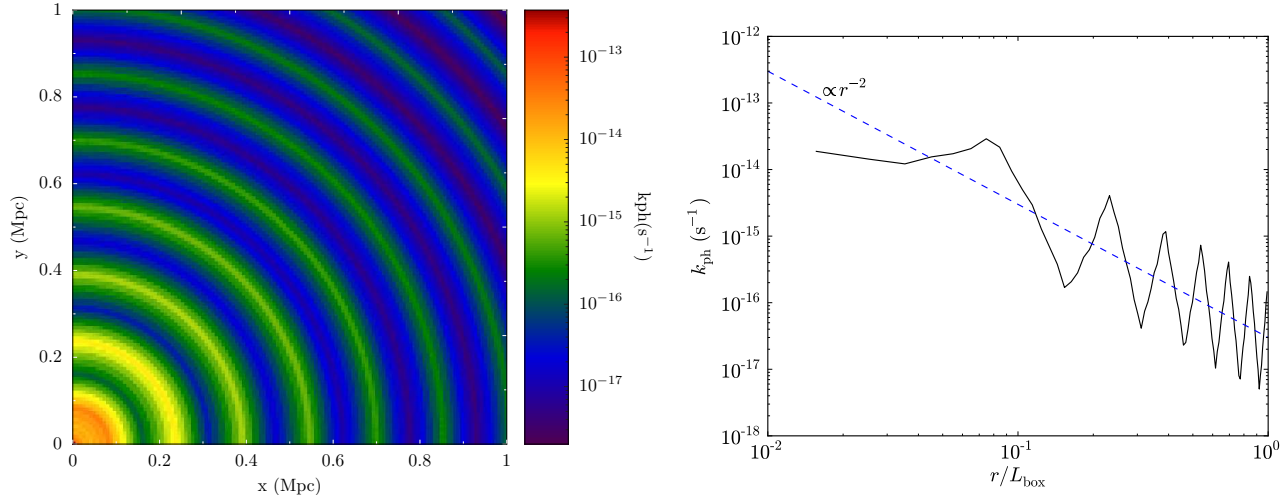
Fig. 29.— Test 12 (Time variations of the source luminosity). Left: Slice of the photo-ionization rate k_{ph} through the origin. The source has a duty cycle of 0.5 Myr, and the box has a light crossing time of 3.3 Myr. The shells of high k_{ph} originate from radiation that was emitted when the source was at its peak luminosity, illustrating the time-dependence of the radiative transfer equation. Right: Radial profile k_{ph} with the inverse square law overplotted.

timesteps if the $c\,dt_{\mathrm{P}} < L_{\mathrm{box}}$. This effect only becomes apparent when the variation timescale of the point source is smaller than the light crossing time of the simulation. Furthermore, the timestep should resolve the variation timescale by a few times. This property might be important in large box simulations with variable sources, e.g. AGN radiative feedback. To test this, we can use an exponentially varying source with some duty cycle. In a functional form, this can be described as

$$L(t) = L_{\mathrm{max}} \times \exp[A(t_f/t_0 - 1)] \tag{40}$$

where $t_f = 2 \times |t - t_0 \times \mathrm{round}(t/t_0)|$, t_0 is the duty cycle, and $A = 4$ controls the width of the radiation pulse. To illustrate the effects of source variability, we remove any dependence on the medium by considering an optically-thin uniform density $\rho 10^{-4}$ cm^{-3}. We take $L_{\mathrm{box}} = 1$ Mpc, which has a light crossing time of 3.3 Myr. A source is placed at the origin with $L_{\mathrm{max}} = 10^{55}$ ph s^{-1} and $t_0 = 0.5$ Myr. We use a radiative transfer timestep of 50 kyr to resolve the duty cycle by 10 timesteps. The simulation is run for 6 Myr, so the radiation propagates throughout the box.

The variability of the source is clearly illustrated in the photo-ionization rates, shown in Figure 29. The shells of relative maximum k_{ph} corresponds to radiation that was emitted
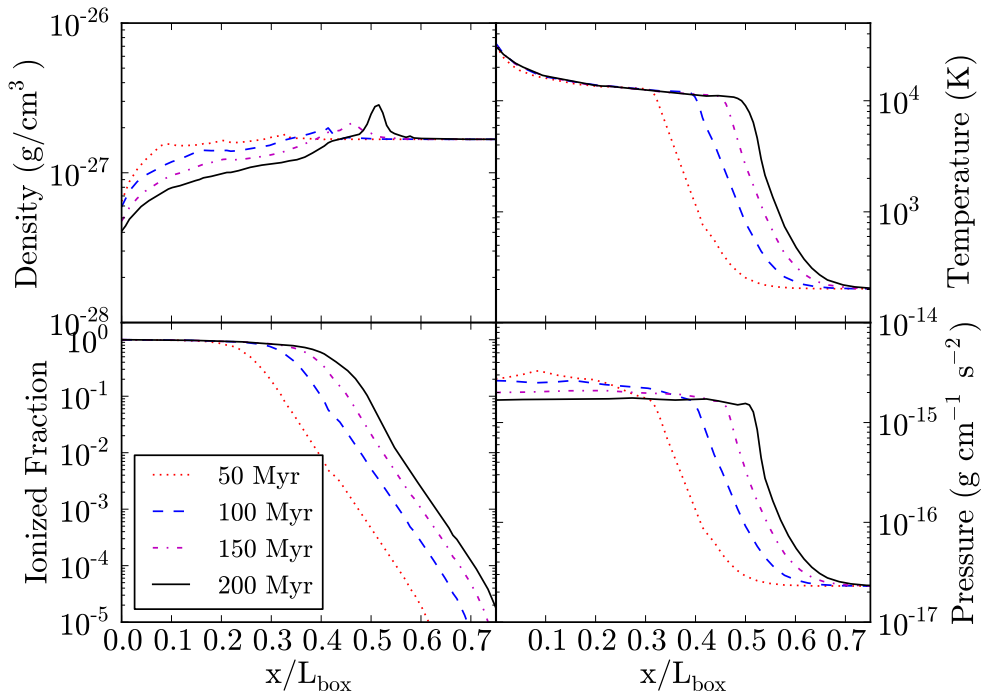
Fig. 30.— Test 12 (Time variations of the source luminosity). Radial profiles of (clockwise from upper left) density, temperature, pressure, and ionized fraction at $t = 50, 100, 150, 200, 250$ Myr. In this problem, the time variations in the source have little effect on the overall H II region expansion. Inside the ionization front at $t = 50$ Myr, there are small density perturbations that are created by the variable source that are later smoothed out over a sound crossing time.

when the source was at its peak luminosity. They are separated by ct_0 Mpc and are geometrically diluted with increasing radius. Averaged over shells of the same width, photo-ionization rates decrease as $1/r^2$.

Next we test the hydrodynamical response to a varying source by repeating Test 5. We set the peak luminosity $L_{\max} = 2 \times 10^{49}$ erg s^{-1} that is a factor of 4 more luminous than Test 5, so the average luminosity is $\sim 5 \times 10^{48}$ erg s^{-1}. The spectrum is mono-chromatic with an energy of 29.6 eV. We set the variation timescale $t_f = cL_{\mathrm{box}}/3 = 16.3$ kyr and use a constant radiative transfer timestep $t_P = t_f/4 = 4.07$ kyr. The simulation is run for 200 Myr. We show the radial profiles of density, temperature, ionized fraction, and pressure in Figure 30. The variable source has little effect on the overall growth of the H II region. It has the approximately the same radius as Test 5 at $t = 200$ Myr when run with a mono-chromatic spectrum (see §6.3). At early times, the variable source creates density perturbations with
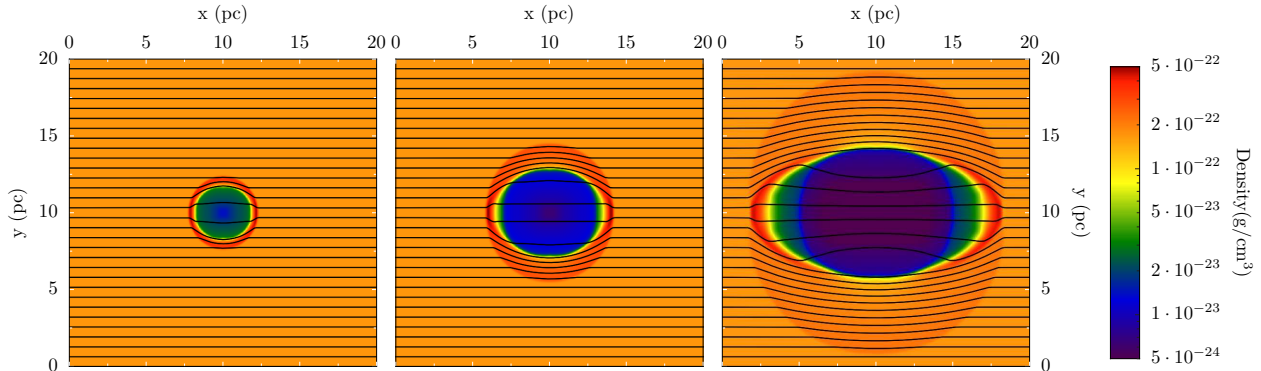
Fig. 31.— Test 14. (H II region with MHD). Left to right: slices of density at $t = 0.18, 0.53, 1.58$ Myr in the x-y plane. The streamlines show the magnetic field.

an average size of 500 pc inside the ionized region, seen in the $t = 50$ Myr profiles. They do not create any instabilities and are smoothed out over its sound crossing time of ~ 50 Myr.

5.9. Test 14. H II region with MHD

Another prevalent physical component in astrophysics is a magnetic field. We utilize the new magnetohydrodynamics (MHD) framework (Wang & Abel 2009) in *Enzo* v2.0 that uses an unsplit conservative hydrodynamics solver and a hyperbolic $\nabla \cdot \mathbf{B} = 0$ cleaning method of Dedner et al. (2002). This marriage of radiation transport and MHD has already been demonstrated in Wang et al. (2010), but for illustrative purposes, we show a test problem with an expanding H II region in an initially uniform density field and constant magnetic field. We use the same problem setup as Krumholz et al. (2007) — $\rho = 100$ cm^{-3}, $T = 11$ K, $L_{\text{box}} = 20$ pc with a resolution of 256^3. This ambient medium is threaded by a magnetic field $\mathbf{B} = 14.2\hat{\mathbf{x}}$ μG. The Alfvén speed is 2.6 km s^{-1}. The radiation source is located in the center of the box with a luminosity $L = 4 \times 10^{46}$ ph s^{-1} with a 17.6 eV mono-chromatic spectrum, resulting in a Strömgren radius $R_s = 0.5$ pc. The simulation is run for 1.58 Myr. The hydrodynamics solver uses an HLL Riemann solver (Harten et al. 1983) and piecewise linear method (PLM) reconstruction (van Leer 1977) for the left and right states in this problem.

As the H II region grows the magnetized medium, shown in Figures 31 and 32, it transforms from spherical to oblate as it is magnetically confined in directions perpendicular to the magnetic field. This occurs at $t > 0.5$ Myr because the magnetic pressure exceeds the thermal pressure, and the gas can only flow along field lines. Krumholz et al. observed
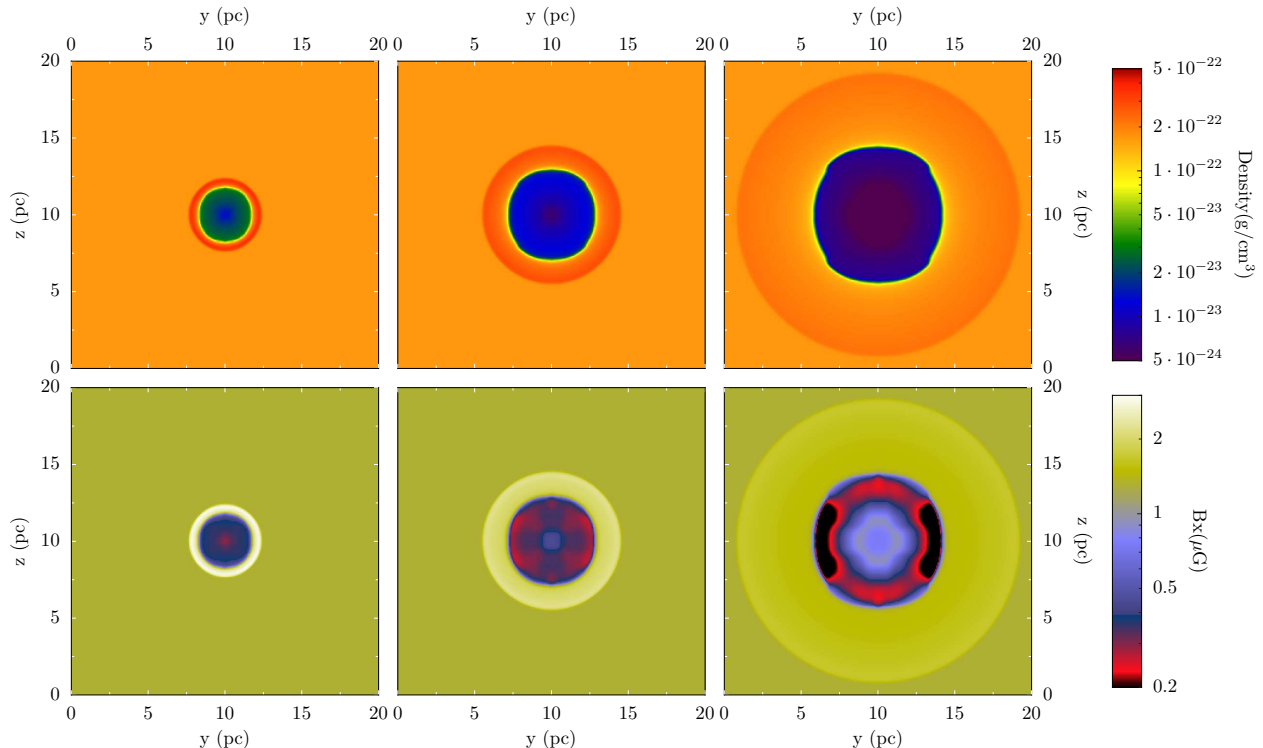
Fig. 32.— Test 14. (H II region with MHD). Slices of density (top) and the x-component of the magnetic field (bottom) in the y-z plane at $t = 0.18, 0.53, 1.58$ Myr (left to right).

some carbuncle artifacts along the ionization front; whereas we see smooth density gradients, which is most likely caused by our more diffusive choice of the HLL Riemann solver when compared to Roe's Riemann solver used in Krumholz et al. (2007), who also use PLM as a reconstruction method. The evolution of the magnetic field lines evolve in a similar manner as their results.

6.   Resolution Tests

Resolution tests are important in validating the accuracy of the code in most circumstances, especially in production simulations where the initial environments surrounding radiation sources are unpredictable. In this section, we show how our adaptive ray-tracing implementation behaves when varying spatial, angular, frequency, and temporal resolutions.
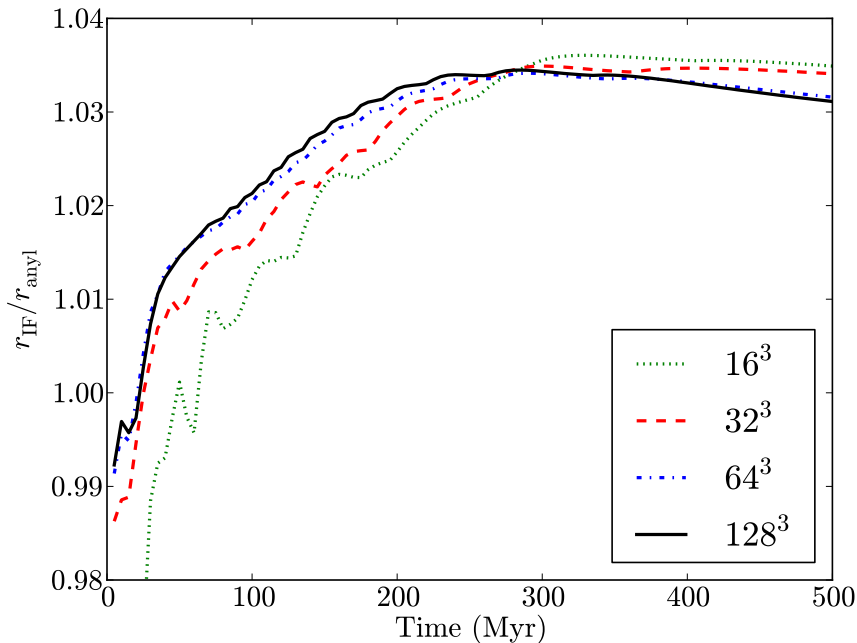
Fig. 33.— Growth of the ionization front radius, compared to the analytical radius, in Test 1 with varying spatial resolutions. At resolutions of 16^3 and 32^3, the ionization front is underestimated for the first ~ 25 Myr but converges within 0.5% of the higher resolution runs.

6.1. Spatial resolution

Here we use Test 1 (§4.1) as a testbed to investigate how the evolution of the Strömgren radius changes with resolution. We keep all aspects of the test the same, but use resolutions of 16^3, 32^3, 64^3, and 128^3. In Figure 33, we show the ratio $r_{\mathrm{IF}}/r_{\mathrm{anyl}}$, similar to Figure 5, using these different resolutions. The radii in the 64^3 and 128^3 runs evolve almost identically. Compared to these resolutions, the lower 16^3 and 32^3 resolution runs only lag behind by 1% until 300 Myr, and afterwards it is larger by 0.5% than the higher resolution cases. This shows that our method gives accurate results, even in marginally resolved cases.

6.2. Angular resolution

The Cartesian grid must been sampled with sufficient rays in order to calculate a smooth radiation field. To determine the dependence on angular resolution, we consider the propagation of radiation through an optically thin, uniform medium. The radiation field should
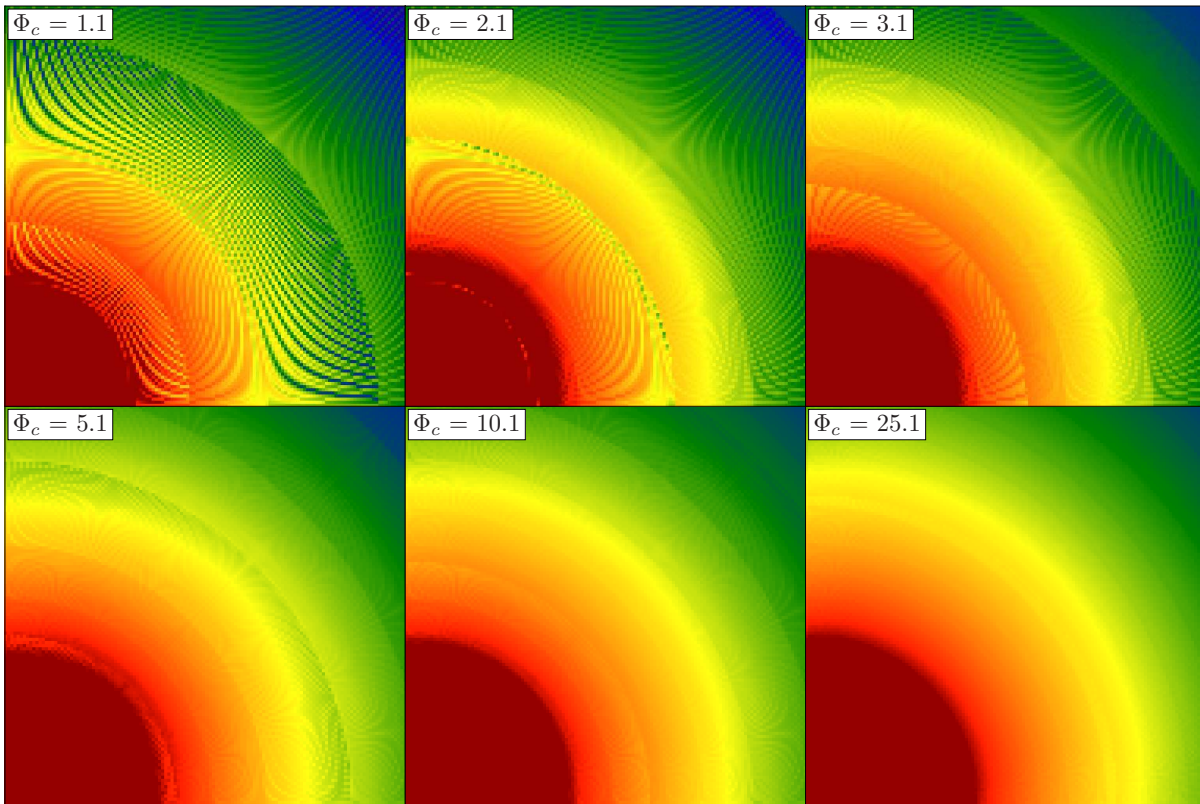
Fig. 34.— Variations in the photo-ionization rates for different ray-to-cell samplings Φ_c. The colormap only spans a factor of 3 to enhance the contrast. In comparison, the photo-ionization rate actually spans 4 orders of magnitude in this test.

follow a $1/r^2$ profile. As the grid is less sampled by rays, the deviation from $1/r^2$ should increase. This test is similar to Test 1, but the medium has $\rho = 10^{-3}$ cm^{-3}, $T = 10^4$ K, and $1 - x_e = 10^{-4}$. The radiation source is located in the center of a 6.6 kpc domain. The simulation is only run for one timestep because the radiation field should be static in this optically-thin test.

We consider minimum ray-to-cell ratios $\Phi_c = (1.1, 2.1, 3.1, 5.1, 10.1, 25.1)$. Slices of the photo-ionization rates through the origin are shown in Figure 34 for these values of Φ_c. In this figure, we limit the colormap range to a factor of 3 to show the nature of the artifacts in more contrast. Unscaled, the rates in the figures would span 4 orders of magnitude. When $\Phi_c \leq 3.1$, the cell-to-cell variations are apparent because there are not enough rays to sufficiently sample the radiation field, even with the geometric correction factor f_c, whose improvements are shown later in §7.1. At $\Phi_c = 5.1$, these artifacts disappear, leaving behind
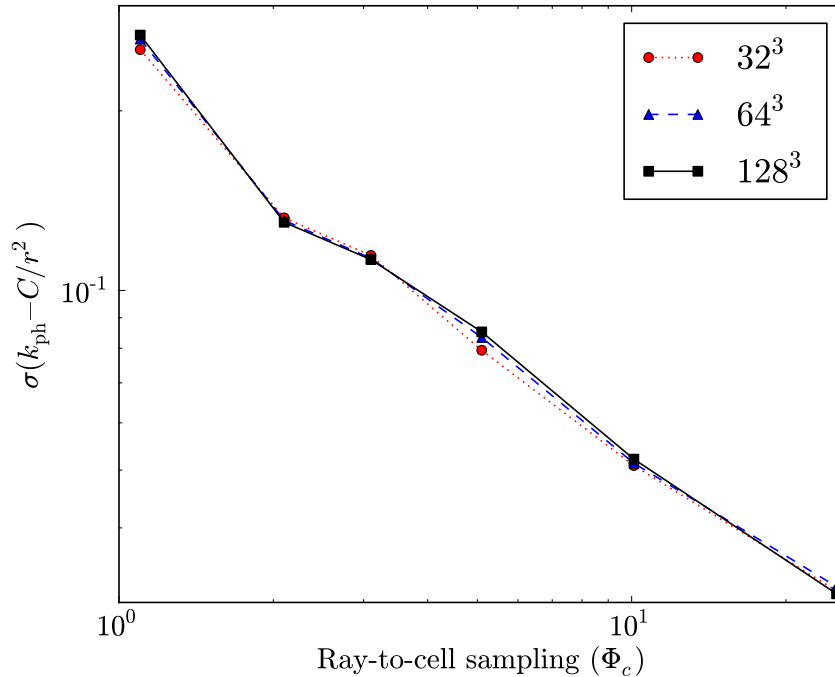
Fig. 35.— Standard deviations of the difference between the computed photo-ionization rates and an inverse square law as a function of ray-to-cell samplings Φ_c for different spatial resolutions. There is no dependence on the spatial resolution, and the accuracy increases as $\sigma \propto \Phi_c^{-0.6}$.

a shell artifact where the radiation fields do not smoothly decrease as $1/r^2$. At higher values of Φ_c, this shell artifact vanishes as well.

One measure of accuracy is the deviation from an $1/r^2$ field because this problem is optically-thin. To depict the increase in accuracy with ray sampling, we take the difference between the calculated photo-ionization rate and a $1/r^2$ field, and then plot the standard deviation of this difference field versus angular resolution in Figure 35. We plot this relation for resolutions of 32^3, 64^3, and 128^3 and find no dependence on spatial resolution, which is expected because we control the angular resolution in terms of cell widths, not in absolute solid angles. We find that the deviation from an inverse square law decreases as $\sigma \propto \Phi_c^{-0.6}$.

6.3.   Frequency resolution

The ionization front radius is within 5–10% of analytical solutions in Tests 1, 2, and 5 with only one energy group; however a multi-frequency spectrum can create differences
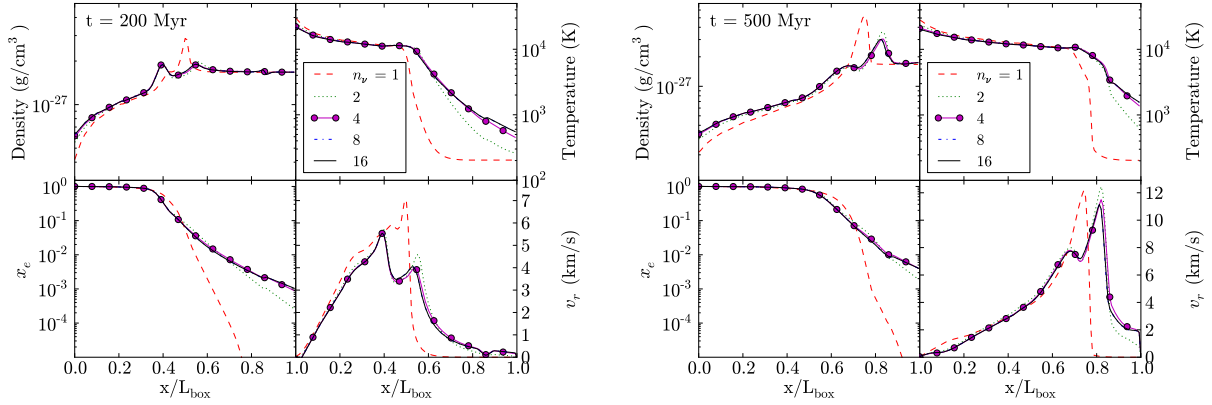
Fig. 36.— Radial profiles of (clockwise from the upper left) density, temperature, radial velocity, and ionized fraction for Test 5 with $n_\nu = 1, 2, 4, 8$, and 16 frequency bins sampling the $T = 10^5$ K blackbody spectrum. The data are shown at $t = 200$ Myr (left) and $t = 500$ Myr (right). The double-peaked structure in the shock only appears with a multi-frequency spectrum. The solution converges at $n_\nu \geq 4$.

in the reactive flows. We use Test 5 (§5.1; an expanding H II region with hydrodynamics) to probe any differences in the solution when varying the resolution of the spectrum. In RT09, ZEUS-MP was used to demonstrate the effect of a multi-frequency spectrum on the dynamics of the ionization front in this test. Instead of a single shock seen in the monochromatic spectrum, a the shock obtained a double-peaked structure in density and radial velocity. We rerun Test 5 with a $T = 10^5$ K blackbody spectrum sampled by $n_\nu = 1, 2, 4, 8$, and 16 frequency bins. We use the following energies:

- $n_\nu = 1$: Mean energy of 29.6 eV

- $n_\nu = 2$: Mean energies in bins 13.6–30 and >30 eV—21.1, 43.0 eV

- $n_\nu = 4$: Mean energies in bins 13.6–20, 20–30, 30–40, and >40 eV—16.7, 24.6, 34.5, 52.1 eV

- $n_\nu = 8, 16$: Logarithmically spaced between 13.6 and 50 eV for the first $n_\nu - 1$ bins, and the last bin is the mean energy above 50 eV.

Figure 36 shows the radial profiles of density, temperature, ionized fraction, and radial velocity at $t = 200$ Myr and $t = 500$ Myr. All of the runs with $n_\nu > 1$ show the double peaked features in density and radial velocities. The mono-chromatic spectrum misses this feature completely because all of the radiation is absorbed at a characteristic column density. In the
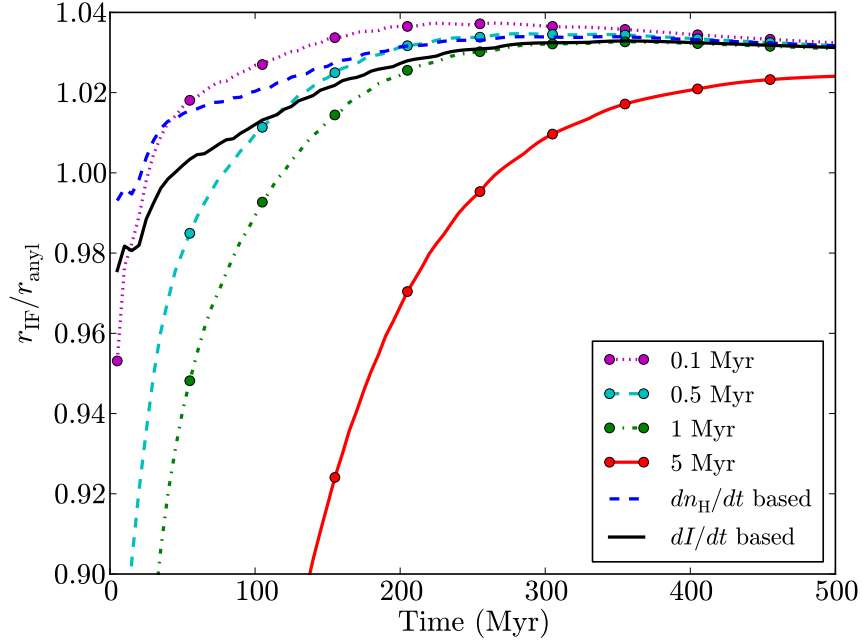
Fig. 37.— Growth of the ionization front radius, compared to the analytical radius, in Test 1 with varying radiative transfer timesteps. The dn_H/dt and dI/dt based timesteps provide the best accuracy, combined with computational efficiency because they take short timesteps when the H II is expanding rapidly but take long timesteps when the photon gradients are small when r_IF is large. At the final time, all but the $t = 5$ Myr constant timestep produce identical ionization front radii.

multi-frequency spectra, the higher energy photons are absorbed at larger column densities and photo-heated this gas. This heated gas creates a photo-evaporative flow that collides with the innermost shock, forming the double peaked density profile. The $n_\nu \geq 4$ runs are indistinguishable, and the $n_\nu = 2$ spectrum only leads to a marginally higher density in the outer shock and lower ionized fractions and temperatures in the ambient medium. In effect, a mono-chromatic spectrum can be sufficient if the problem focuses on large-scale quantities, e.g. ionized filling fractions in reionization calculations. Conversely these effects may be important when studying the details of small-scale processes, e.g. photo-evaporation.
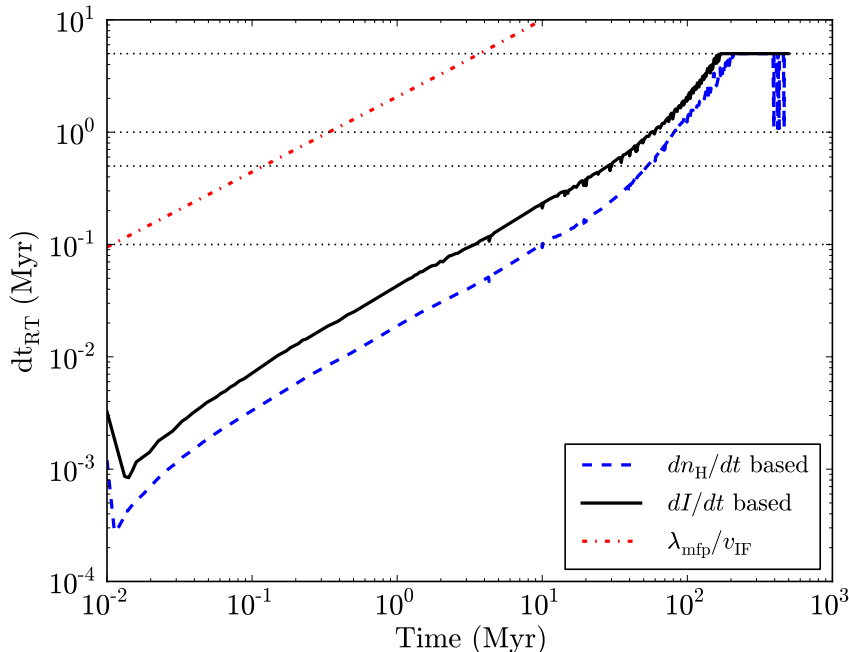
Fig. 38.— Variable time-stepping for the methods that limit change in neutral fraction (solid) and specific intensity (dotted). The horizontal lines show the constant timesteps that were used in the tests. The crossing time of a mean free path by the ionization front is plotted for reference.

6.4. Temporal resolution

The previous three dependencies did not affect the propagation of the ionization front greatly. However in our and others' past experience (Shapiro et al. 2004; Mellema et al. 2006; Petkova & Springel 2009, e.g.), the timestep, especially too small of one, can drastically underestimate the ionization front velocity. Here we use Test 1 but with 64^3 resolution to compare different time-stepping methods — restricted changes in H II (dn_{H}/dt based; §3.4.1), constant timesteps (§3.4.3), and based on incident radiation (dI/dt based; §3.4.4). The growth of the ionization front radius is shown in Figure 37. Both the H II restricted and incident radiation variable time-stepping methods agree within a few percent throughout the entire simulation, as does the run with constant $dt = 0.1$ Myr timesteps. With the larger constant timesteps, the numerical solution lags behind the analytical one, but they converge to an accurate H II radii at late times. Even $dt = 5$ Myr timestep, which underestimated it by 35% at 50 Myr, is within a percent of the analytical solution.

The larger constant timesteps deviate from these more accurate solutions at early times

because the photon energy gradient is large, and thus so is the ionization front velocity. To understand this, the ionization front can be considered static in a given timestep. Here the ionizing radiation can only penetrate into the neutral gas by roughly a photon mean path λ_mfp. Only in the next timestep, the ionization front can advance. If the timestep is larger than $\lambda_\mathrm{mfp}/v_\mathrm{IF,anyl}$, then the numerical solution may fall behind.

The variable time-stepping of the dn_H/dt and dI/dt methods adjust accordingly to the physical situation, as seen in the plot of timestep versus time (Figure 38). They provide high accuracy when the source first starts to shine. At later times, the ionization front slows as it approaches the Strömgren radius, and large timesteps are no longer necessary. The dI/dt method has a similar timestep as the dn_H/dt method. It is larger by a factor of ~ 2 because of our choice of the safety factor $C_\mathrm{RT,cfl} = 0.5$. This causes its calculated radius to be smaller by 1% at $t < t_\mathrm{rec}$, which is still in good agreement with the analytical value.

7. Methodology Tests

Here we show tests that evaluate new features in Enzo+Moray, such as the improvements from the geometric correction factor, optically-thin approximations, treatment of X-ray radiation, and radiation pressure. Lastly we test for any non-spherical artifacts in the case of two sources.

7.1. Improvements from the covering factor correction

As discussed in §2.5, non-spherical artifacts are created by a mismatch between the HEALPix pixelization and the Cartesian grid. This is especially apparent in optically-thin regions, where the area of the pixel is greater than the $(1 - e^{-\tau})$ absorption factor. In this section, we repeat the angular resolution tests in §6.2. Slices of the photo-ionization rates through the origin are shown in Figure 39, depicting the improvements in spherical symmetry and a closer agreement to a smooth $1/r^2$ profile. Previous attempts to reduce these artifacts either introduced a random rotation of the HEALPix pixelization (e.g. Abel & Wandelt 2002; Trac & Cen 2007; Krumholz et al. 2007) or by increasing the ray-to-cell sampling.

In the x-y plane without the correction, there exists shell artifacts where the photo-ionization rates abruptly drops when the rays are split. This occurs because the photon flux in the rays are constant, so k_ph is purely dependent on the ray segment length through each cell. Geometric dilution mainly occurs when the number of rays passing through a cell
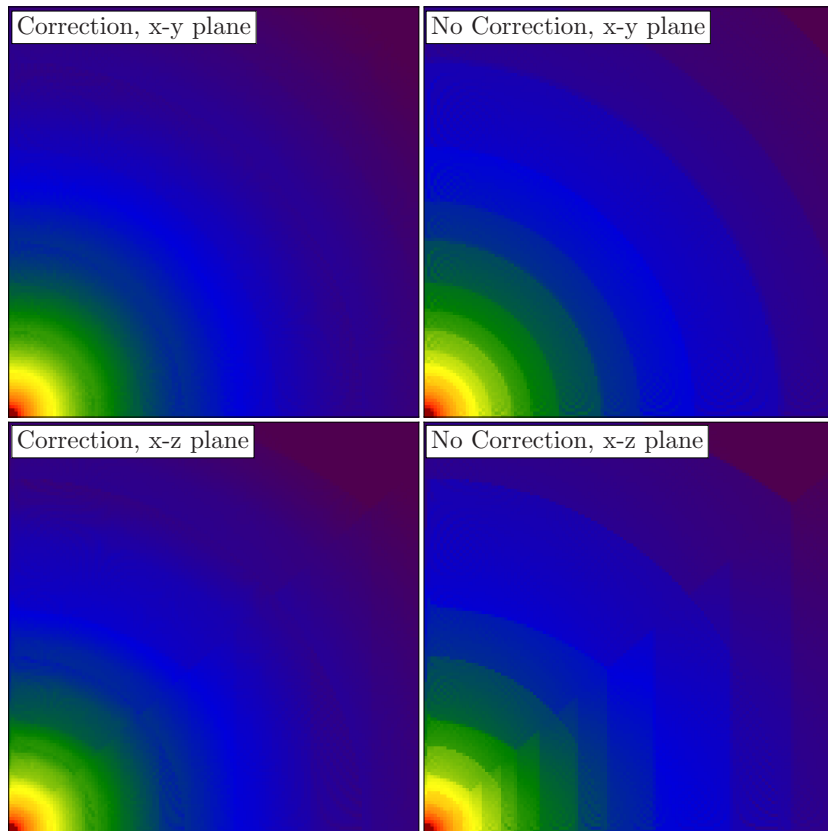
Fig. 39.— Slices of the photo-ionization rate in the x-y plane (top row) and x-z plane (bottom row) with (left column) and without (right column) the geometric correction. The slices are through the origin. In the x-y plane, it reduces the shell artifacts. In the x-z plane, it reduces the severity of a non-spherical artifact delineated at a 45 degree angle, where the HEALPix scheme switches from polar to equatorial type pixels.

decreases. With the correction, geometric dilution also occurs when the ray's solid angle only partially covers the cell. This by itself alleviates these shell artifacts. In the x-z plane without the correction, there is a non-spherical artifact delineated at a 45 degree angle. In the lower region, the rays are associated with equatorial HEALPix pixels, and in the upper region, they are polar HEALPix pixels. This artifact is not seen in the x-y plane because all rays are of a equatorial type. The geometric correction smooths this artifact but does not completely remove it.
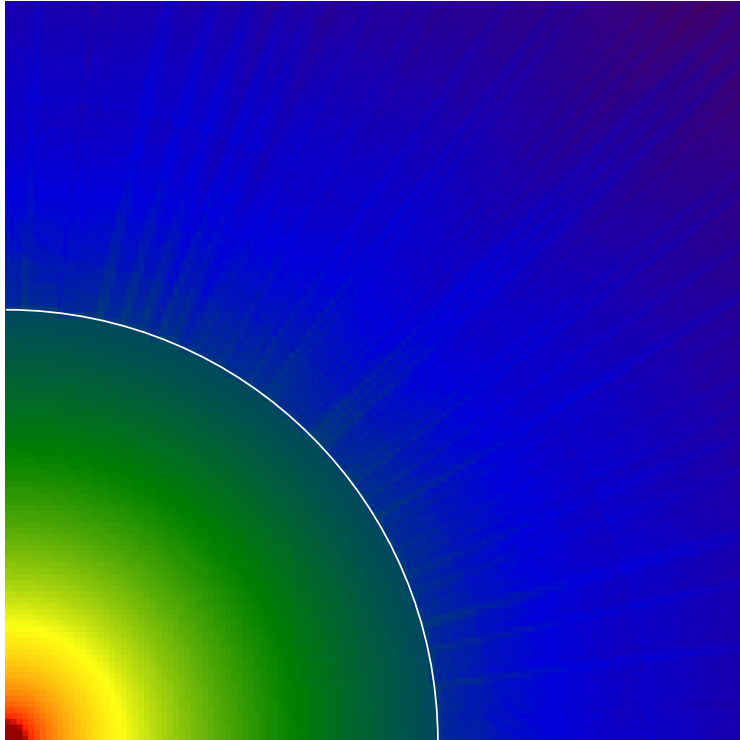
Fig. 40.— Optically-thin approximation to the radiation field with one ray per cell in optically thin regions. The angular artifacts result from the transition to optically thick (white line) at an optical depth $\tau = 0.1$.

7.2. Optically-thin approximation

In practice, we have found it difficult to transition from this optically-thin approximation to the optically-thick regime without producing artifacts in the photo-ionization rate k_{ph}. We use the optically thin problem used in the angular resolution test (§6.2) with $\Phi_c = 5.1$ to show these artifacts in k_{ph} in Figure 40. The radiation field strictly follows a $1/r^2$ profile until it reaches $\tau_{\mathrm{thin}} \equiv 0.1$, which is denoted by the white quarter circle in the figure. At this radius, the rays are then split until a sampling of Φ_c is satisfied. Angular spike artifacts beyond this radius arise because of the interface between the optically-thin approximation and full ray tracing treatment. They originate in cells that intersect the τ_{thin} surface, which are split into the optically thin and thick definitions. Unfortunately we have not determined a good technique to avoid such artifacts. They occur because of the following reason. When the first ray with $\tau < 0.1$ exits such a cell, it applies the optically-thin approximation and marks the cell so no other ray from the same source contributes to its k_{ph} and Γ field. However other rays may exit the cell with $\tau > 0.1$ because the maximum distance between
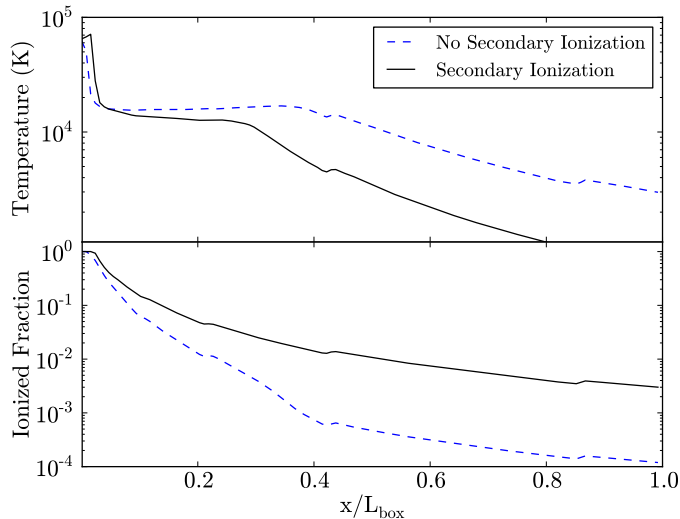
Fig. 41.— Radial profiles of temperature and ionized fraction showing the effects of secondary ionizations from a mono-chromatic 1 keV spectrum. The discontinuity at $r \sim 0.4$ is caused by artifacts in the ray tracing, which is described in Test 1. The high energy photons can ionize multiple hydrogen atoms, increasing the ionized fraction. In part, less radiation goes into thermal energy, lowering the temperature.

the far cell faces and the source is not always $\tau < 0.1$. Then these rays will split in this cell and add to $k_{\rm ph}$ and become attenuated, reducing its photon fluxes. When the rays continue to the next cell after this transition, the photon fluxes are not necessarily equal to each other, creating the angular artifacts seen in Figure 40. We are continuing to formulate a scheme that avoids these artifacts because this approximation will be very advantageous in simulations with large ionized filling factors.

7.3. X-Ray secondary ionizations and reduced photo-heating

Here we test our implementation of secondary ionizations from high-energy photons above 100 eV, described in §2.4.2 and used in Alvarez et al. (2009) in the context of accreting black holes. We use the same setup as Test 5 but with an increased luminosity $L = 10^{50}$ erg s^{-1} and a mono-chromatic spectrum of 1 keV. Figure 41 compares the density, temperature, ionized fraction, and neutral fraction of the expanding H II region considering secondary ionizations and reduced photo-heating and considering only one ionization per photon and the remaining energy being thermalized.
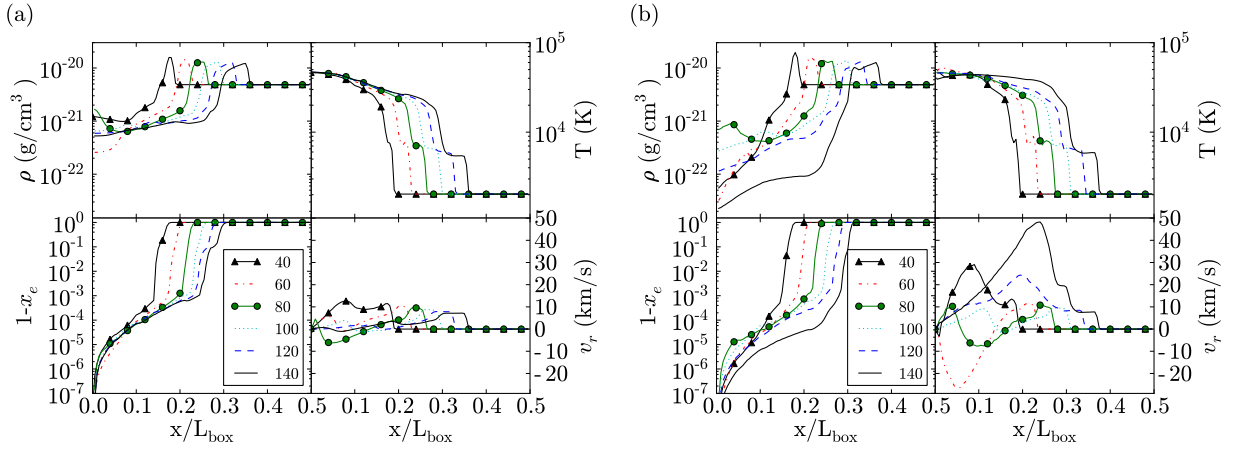
Fig. 42.— (a) No radiation pressure. Radial profiles of (clockwise from top left) density, temperature, radial velocity, and neutral fraction. Time units in the legend are in kyr. (b) Radial profiles with radiation pressure. The momentum transferred to the gas drives out the gas at higher velocities than without radiation pressure. Afterwards the central region is under-pressurized, and the gas infalls toward the center, as seen at t = 60 kyr. Then the radiation pressure continues to force the gas outwards, increasing gas velocities up to 50 km/s.

Figure 41 shows the main effects of secondary ionizations from the 1 keV spectrum on the ionization and thermal state of the system. Without secondary ionizations, each absorption results in one ionization with the remaining energy transferred into thermal energy. But with secondary ionizations, recall that most of the radiation energy goes into hydrogen and helium ionizations in neutral gas; whereas in ionized gas, most of the energy is thermalized. In this test, only the inner 300 pc is completely ionized because of the small cross-section of hydrogen at $E_{\rm ph} = 1$ keV. Beyond this core, the medium is only partially ionized. This process expands the hot $T = 10^5$ K core by a factor of 2. In the outer neutral regions, the ionization fraction is larger by a factor of ~ 10, which in turn results in less photo-heating, lowering the temperature by a factor 2–3.

7.4. Radiation pressure

Radiation pressure affects gas dynamics in an H II region when its force is comparable to the acceleration created by gas pressure of the heated region. The imparted acceleration on a hydrogen atom $\mathbf{a}_{\rm rp} = E_{\rm ph}/c$. This is especially important when the ionization front is in its initial R-type phase, where the gas has not reacted to the thermal pressure yet. Thus
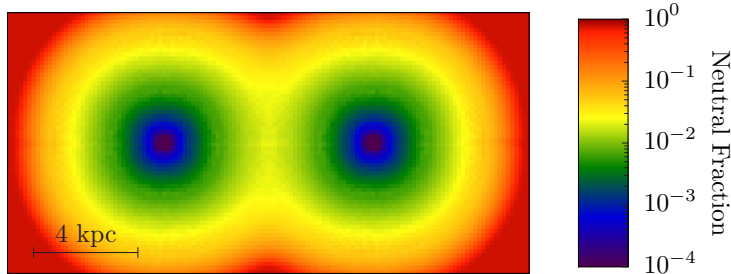
Fig. 43.— Slice of neutral fraction at $t = 500$ Myr through the sources in the consolidated H II test. There are no artifacts associated with rays being emitted from two sources. Both of the ionized regions are spherically symmetric before they overlap.

we construct a test that focuses on a small scales, compared to the Strömgren radius. The domain has a size of 8 pc with a uniform density $\rho = 2900\text{cm}^{-3}$ and initial temperature $T = 10^3$ K. The source is located at the origin with a luminosity $L = 10^{50}$ ph s^{-1} and a $T = 10^5$ K blackbody spectrum. We use one energy group $E_{\text{ph}} = 29.6$ eV. The grid is adaptively refined on overdensity with the same criterion as Test 8. The simulation is run for 140 kyr.

We compare nearly identical simulations but one with radiation pressure and one without radiation pressure to quantify its effects. Radial profiles of density, temperature, neutral fraction, and radial velocity are shown in Figure 42 for both simulations at several times. Without radiation pressure, the evolution of the H II is matches the analytical expectations described in §5.1. At $t = 140$ kyr, the ionization front radius is increased by $\sim 5\% = 0.16$ pc. However radiation pressure impacts the system the greatest inside the ionization front. At $t = 40$ kyr, the central density is smaller by a factor of 20 with radiation pressure, but the temperatures are almost equal. A rarefaction wave thus propagates toward the center, depicted by the negative radial velocities at $t = 60$ kyr. This raises the central density to 10^{-21} g cm^{-3} at $t = 80$ kyr. Afterwards, the radiation continues to force gas outwards. From $t = 100$ kyr to $t = 140$ kyr, the maximum radial velocity of the ionized gas increases from 10 km s^{-1} to 50 km s^{-1}. This leaves behind an even more diffuse medium, lowering the gas density by a factor of 10 at $t = 140$ kyr. Thus the recombination rates are lower, resulting in increased ionization fractions and temperatures in the H II region.

7.5. Consolidated H II region with two sources

Here we test for any inaccuracies in the case of multiple sources. We use the same test problem as Petkova & Springel (2009, §5.1.2), which has two sources with luminosities of 5×10^{48} ph s^{-1} and are separated by 8 kpc. The ambient medium is static with a uniform density of 10^{-3} cm^{-3} and $T = 10^4$ K. This setup is similar to Test 1. The domain has a resolution of $128 \times 64 \times 64$ It is 20 kpc in width and is 10 kpc in height and depth. The problem is run for 500 Myr.

The H II regions grow to $r = 4$ kpc where they overlap. Then the two sources are enveloped in a common, elongated H II region. To illustrate this, we show the neutral fraction in Figure 43. Our method keeps spherical symmetry close to the individual sources, and there are no perceptible artifacts from having multiple sources.

8. Parallel Performance

Last we demonstrate the parallel performance of Enzo+Moray in weak and strong scaling tests. For large simulations to consider radiative transfer, it is imperative that the code scales to large number of processors.

8.1. Weak Scaling

Weak scaling tests demonstrates how the code scales with the number of processors with a constant amount of work per processor. Here we construct a test problem with a 64^3 block per core. The grid is not adaptively refined. The physical setup of the problem is the same as Test 5 with a uniform density $\rho = 10^{-3}$cm^{-3} and initial temperature $T = 100$ K. Each block has the same size of 15 kpc as Test 5. At the center of each grid, there exists a radiation source with a luminosity $L = 5 \times 10^{48}$ ph s^{-1} and a 17 eV mono-chromatic spectrum. The problem is run for 250 Myr. We run this test with $N_p = 2^n$ cores with $n = [0, 1 \ldots 10, 11]$. The domain has (N_x, N_y, N_z) blocks that is determined with the MPI routine `MPI_Dims_create`. For example with $n = 7$, the problem is decomposed into $(N_x, N_y, N_z) = (4, 4, 8)$ blocks, producing a $256 \times 256 \times 512$ grid. We have run these on the original (Harpertown CPUs) nodes of the NASA NAS machine, Pleiades, with 8 cores per node. Figure 44 shows the performance timings of various parts of the code. From one to two cores, the total time only increases by $\sim 1\%$ due to the overhead associated with the inter-processor message passing. From two to eight cores, the performance decreases in the hydrodynamics solver, chemistry and energy solver, and obtaining the hydrodynamic boundary conditions because
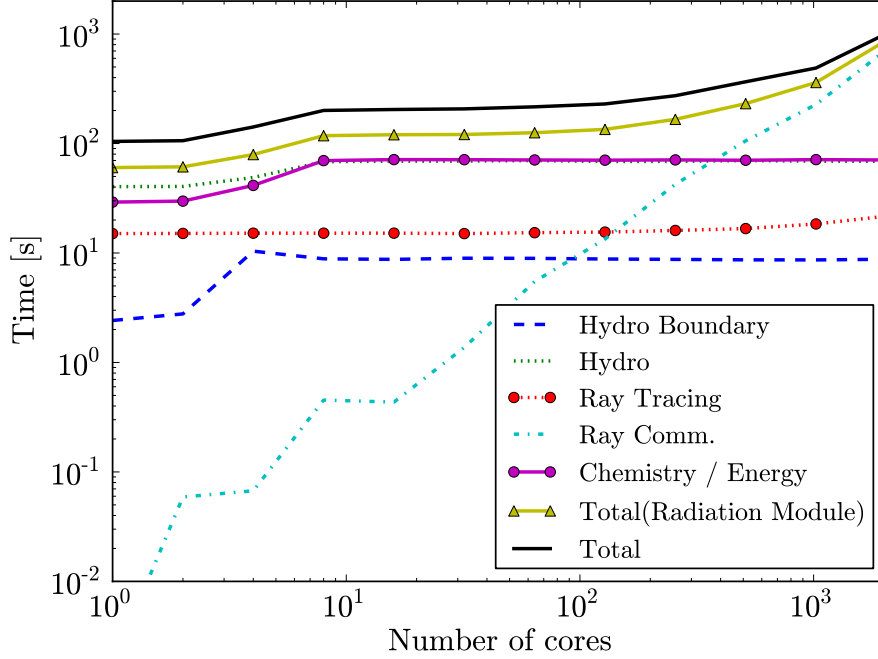
Fig. 44.— Weak scaling test with one 64^3 block per process. Each block has one source and is set up similar to the radiation hydrodynamics Test 5. Above 8 processes, all parts of the code exhibit good weak scaling except for the inter-processor ray communication. The radiation module timing include the ray tracing, communication, chemistry and energy solver, and all other overheads associated with the radiation transport. Cache locality of the data causes the decrease in performance from 1 to 8 processes.

of cache locality problems of the data being passed to the CPU. This occurs because of the CPU architecture, specifically the L1 cache and core connectivity. We see less of a penalty in newer processors, e.g. Intel Nehalam and Westmere CPUs. Unfortunately there exists a $N_p^{1.5}$ dependence in the ray communication routines. It becomes the dominant process above 512 processes. We are actively pursing a solution to this scaling problem. The other parts of the code exhibit excellent weak scaling. Overall it scales well to 512 processes, and we plan to enhance the weak scalability of Enzo+Moray in the near future to larger processor counts.

8.2. Strong Scaling

Strong scaling tests shows how the problem scales with the number of processors for the same problem. The overhead associated with the structured AMR framework in *Enzo* can limit the strong scalability. One key property of strong scaling is that each processor must have sufficient work to compute, compared to the communication involved. Here we use a small-box reionization calculation with $L_{\mathrm{box}} = 3$ Mpc/h, a resolution of 256^3, and 6 levels of refinement. We measure the time spent on the hydrodynamics, non-equilibrium chemistry, the rebuilding of the AMR hierarchy, and ray tracing in a single level-0 timestep, lasting 5 Myr, at $z = 9.5$. There are ??? point sources in this calculation at this redshift. The ionized volume fraction is ???.

9. Summary

In this paper, we have presented our implementation of adaptive ray tracing (Abel & Wandelt 2002) and its coupling to the hydrodynamics in the cosmology AMR code *Enzo*, making it a fully functional radiation hydrodynamics code. As this method is photon conserving, accurate solutions are possible with coarse spatial resolution. A new geometric correction factor to ray tracing on a Cartesian grid was described, and it is general to any implementation. We have exhaustively tested the code to problems with known analytical solutions and the problems presented in the RT06 and RT09 radiative transfer comparison papers. Additionally we have tested our code with more dynamical problems—champagne flows, Rayleigh-Taylor instabilities, photo-evaporation of a blastwave, beamed radiation, a time-varying source, and an H II region with MHD—to demonstrate the flexibility and fidelity of Enzo+Moray. Because production simulations may not have the resolution afforded in these test problems, we have tested the dependence on spatial, angular, frequency, and temporal resolution. It provides accurate solutions even at low resolution, except for the large constant timesteps. However, we have described two methods to determine the radiative transfer timestep that are based on the variations in specific intensity or changes in neutral fraction inside the ionization front. Both methods give very accurate results and provide the largest timestep to obtain an accurate solution, ultimately leading to higher computational efficiency. On the same topic, we have described a method to calculate the radiation field in the optically-thin limit with ray tracing.

Being a ray tracing code, it scales with the number of radiation sources, albeit lessened with ray merging; nevertheless, it scales well to O(10^3) processors for problems with $\sim 10^9$ computational cells and $\sim 10^4$ sources, such as reionization calculations. We have also shown that the code shows good strong scaling in AMR calculations, given a large enough problem.

The combination of the AMR and adaptive ray tracing allows for high-resolution and high-dynamical range problems, e.g. molecular cloud resolving galaxy formation simulations and H II regions of Population III stars. Furthermore, we have included Lyman-Werner absorption, secondary ionizations from X-ray radiation, Compton heating from photon scattering, and radiation pressure, into the code, which extends the reach of Enzo+Moray to study AGN feedback, stellar winds, and local star formation. Coupling the radiative transfer with MHD further broadens the applicability of our code. The full implementation is included in the latest public version of *Enzo*[2], providing the community with a full-featured radiation hydrodynamics AMR code.

REFERENCES

Abel, T., Anninos, P., Zhang, Y., & Norman, M. L. 1997, New Astronomy, 2, 181

Abel, T., Norman, M. L., & Madau, P. 1999, ApJ, 523, 66

Abel, T., & Wandelt, B. D. 2002, MNRAS, 330, L53

Abel, T., Wise, J. H., & Bryan, G. L. 2007, ApJ, 659, L87

Altay, G., Croft, R. A. C., & Pelupessy, I. 2008, MNRAS, 386, 1931

Alvarez, M. A., Bromm, V., & Shapiro, P. R. 2006a, ApJ, 639, 621

—. 2006b, ApJ, 639, 621

Alvarez, M. A., Wise, J. H., & Abel, T. 2009, ApJ, 701, L133

Anninos, P., Zhang, Y., Abel, T., & Norman, M. L. 1997, New Astronomy, 2, 209

Aubert, D., & Teyssier, R. 2008, MNRAS, 387, 295

Auer, L. H., & Mihalas, D. 1970, MNRAS, 149, 65

Axford, W. I. 1961, Royal Society of London Philosophical Transactions Series A, 253, 301

---

[2]http://lca.ucsd.edu/enzo

Berger, M. J., & Colella, P. 1989, Journal of Computational Physics, 82, 64

Bisbas, T. G., Wünsch, R., Whitworth, A. P., & Hubber, D. A. 2009, A&A, 497, 649

Bodenheimer, P., Tenorio-Tagle, G., & Yorke, H. W. 1979, ApJ, 233, 85

Bryan, G. L., & Norman, M. L. 1997, ArXiv Astrophysics e-prints

Ciardi, B., Ferrara, A., Marri, S., & Raimondo, G. 2001, MNRAS, 324, 381

Dedner, A., Kemm, F., Kröner, D., Munz, C., Schnitzer, T., & Wesenberg, M. 2002, Journal of Computational Physics, 175, 645

Draine, B. T., & Bertoldi, F. 1996, ApJ, 468, 269

Finlator, K., Özel, F., & Davé, R. 2009, MNRAS, 393, 1090

Franco, J., Tenorio-Tagle, G., & Bodenheimer, P. 1990, ApJ, 349, 126

Gnedin, N. Y. 2000, ApJ, 542, 535

Gnedin, N. Y., & Abel, T. 2001, New Astronomy, 6, 437

Gnedin, N. Y., & Ostriker, J. P. 1997, ApJ, 486, 581

González, M., Audit, E., & Huynh, P. 2007, A&A, 464, 429

Górski, K. M., Hivon, E., Banday, A. J., Wandelt, B. D., Hansen, F. K., Reinecke, M., & Bartelmann, M. 2005, ApJ, 622, 759

Harten, A., Lax, P. D., & van Leer, B. 1983, SIAM Review, 25, 35

Hasegawa, K., Umemura, M., & Susa, H. 2009, MNRAS, 395, 1280

Hester, J. J., Scowen, P. A., Sankrit, R., Lauer, T. R., Ajhar, E. A., Baum, W. A., Code, A., Currie, D. G., Danielson, G. E., Ewald, S. P., Faber, S. M., Grillmair, C. J., Groth, E. J., Holtzman, J. A., Hunter, D. A., Kristian, J., Light, R. M., Lynds, C. R., Monet, D. G., O'Neil, Jr., E. J., Shaya, E. J., Seidelmann, K. P., & Westphal, J. A. 1996, AJ, 111, 2349

Hjellming, R. M. 1966, ApJ, 143, 420

Iliev, I. T., Ciardi, B., Alvarez, M. A., Maselli, A., Ferrara, A., Gnedin, N. Y., Mellema, G., Nakamoto, T., Norman, M. L., Razoumov, A. O., Rijkhorst, E., Ritzerveld, J., Shapiro, P. R., Susa, H., Umemura, M., & Whalen, D. J. 2006a, MNRAS, 371, 1057

Iliev, I. T., Mellema, G., Pen, U., Merz, H., Shapiro, P. R., & Alvarez, M. A. 2006b, MNRAS, 369, 1625

Iliev, I. T., Mellema, G., Shapiro, P. R., & Pen, U. 2007, MNRAS, 376, 534

Iliev, I. T., Whalen, D., Mellema, G., Ahn, K., Baek, S., Gnedin, N. Y., Kravtsov, A. V., Norman, M., Raicevic, M., Reynolds, D. R., Sato, D., Shapiro, P. R., Semelin, B., Smidt, J., Susa, H., Theuns, T., & Umemura, M. 2009, MNRAS, 1313

Johnson, J. L., Greif, T. H., & Bromm, V. 2007, ApJ, 665, 85

Kahn, F. D. 1954, Bull. Astron. Inst. Netherlands, 12, 187

Kim, J. H., Wise, J. H., Alvarez, M. A., & Abel, T. 2011, ApJ, In preparation

Krumholz, M. R., Stone, J. M., & Gardiner, T. A. 2007, ApJ, 671, 518

Lasker, B. M. 1966, ApJ, 143, 700

Liska, R., & Wendroff, B. 2003, SIAM Journal on Scientific Computing, 25, 995

Mathews, W. G. 1965, ApJ, 142, 1120

McQuinn, M., Lidz, A., Zahn, O., Dutta, S., Hernquist, L., & Zaldarriaga, M. 2007, MNRAS, 377, 1043

Mellema, G., Iliev, I. T., Alvarez, M. A., & Shapiro, P. R. 2006, New Astronomy, 11, 374

Mihalas, D., & Mihalas, B. W. 1984, Foundations of radiation hydrodynamics, ed. Mihalas, D. & Mihalas, B. W.

Miralda-Escudé, J., Haehnelt, M., & Rees, M. J. 2000, ApJ, 530, 1

Norman, M. L., Paschos, P., & Abel, T. 1998, Mem. Soc. Astron. Italiana, 69, 455

Oort, J. H. 1954, Bull. Astron. Inst. Netherlands, 12, 177

O'Shea, B. W., Bryan, G., Bordner, J., Norman, M. L., Abel, T., Harkness, R., & Kritsuk, A. 2004, ArXiv Astrophysics e-prints

Osterbrock, D. E. 1989, Astrophysics of gaseous nebulae and active galactic nuclei, ed. Osterbrock, D. E.

Paardekooper, J., Kruip, C. J. H., & Icke, V. 2010, A&A, 515, A79+

Pawlik, A. H., & Schaye, J. 2008, MNRAS, 389, 651

—. 2010, ArXiv e-prints

Petkova, M., & Springel, V. 2009, MNRAS, 396, 1383

Razoumov, A. O., & Scott, D. 1999, MNRAS, 309, 287

Ricotti, M., Gnedin, N. Y., & Shull, J. M. 2001, ApJ, 560, 580

Rijkhorst, E., Plewa, T., Dubey, A., & Mellema, G. 2006, A&A, 452, 907

Rybicki, G. B., & Lightman, A. P. 1979, Radiative processes in astrophysics, ed. Rybicki, G. B. & Lightman, A. P.

Sandford, II, M. T., Whitaker, R. W., & Klein, R. I. 1982, ApJ, 260, 183

Schatzman, E., & Kahn, F. D. 1955, in IAU Symposium, Vol. 2, Gas Dynamics of Cosmic Clouds, 163–+

Shapiro, P. R., Iliev, I. T., & Raga, A. C. 2004, MNRAS, 348, 753

Shull, J. M., & van Steenberg, M. E. 1985, ApJ, 298, 268

Sokasian, A., Abel, T., Hernquist, L., & Springel, V. 2003, MNRAS, 344, 607

Sokasian, A., Abel, T., & Hernquist, L. E. 2001, New Astronomy, 6, 359

Spitzer, L. 1978, Physical processes in the interstellar medium, ed. Spitzer, L.

Spitzer, Jr., L. 1948, ApJ, 107, 6

—. 1949, ApJ, 109, 337

—. 1954, ApJ, 120, 1

Spitzer, Jr., L., & Savedoff, M. P. 1950, ApJ, 111, 593

Stone, J. M., Gardiner, T. A., Teuben, P., Hawley, J. F., & Simon, J. B. 2008, ApJS, 178, 137

Stone, J. M., Mihalas, D., & Norman, M. L. 1992, ApJS, 80, 819

Strömgren, B. 1939, ApJ, 89, 526

Susa, H. 2006, PASJ, 58, 445

Trac, H., & Cen, R. 2007, ApJ, 671, 1

Truelove, J. K., & McKee, C. F. 1999, ApJS, 120, 299

Turk, M. J. 2008, in Proceedings of the 7th Python in Science Conference, ed. G. Varoquaux,
    T. Vaught, & J. Millman, Pasadena, CA USA, 46 – 50

van Leer, B. 1977, Journal of Computational Physics, 23, 276

Wang, P., & Abel, T. 2009, ApJ, 696, 96

Wang, P., Li, Z., Abel, T., & Nakamura, F. 2010, ApJ, 709, 27

Whalen, D., & Norman, M. L. 2006, ApJS, 162, 281

Wise, J. H., & Abel, T. 2008a, ApJ, 684, 1

—. 2008b, ApJ, 685, 40

Wise, J. H., & Cen, R. 2009, ApJ, 693, 984

Yorke, H. W. 1986, ARA&A, 24, 49

Yorke, H. W., Tenorio-Tagle, G., & Bodenheimer, P. 1983, A&A, 127, 313